



Norwegian University of
Science and Technology

Exploring possibilities in AFM studies of InAs/GaAs QDs

Simon Riis Iden

Master of Science in Physics and Mathematics

Submission date: Januar 2012

Supervisor: Turid Worren Reenaas, IFY

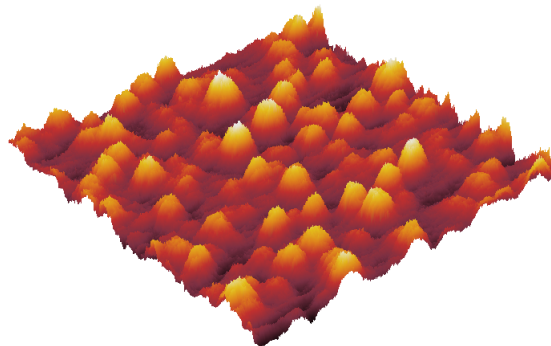
Co-supervisor: Bjørn-Ove Fimland, IET



Faculty of Natural Sciences
and Technology
Department of Physics

Exploring possibilities in AFM studies of InAs/GaAs QDs

Simon Riis Iden



JANUARY 9TH, 2012

TFY4900 - *Master Of Technology, Applied Physics*

This work was a part of the *QD-IBSC* group at

Department of Physics

The Faculty of Natural Sciences and Technology

Norwegian University of Science and Technology

(NTNU)

QD-IBSC group

Associate professor Turid Worren Reenaas

Professor Bjørn-Ove Fimland

Ph.D. Maryam Gholami Mayani

Master student Arnt Joachim Wrålsen

Supervisor:

Associate professor Turid Worren Reenaas

Department of Physics, NTNU

Co-supervisor:

Professor Bjørn-Ove Fimland

Department of Electronics and Telecommunications, NTNU

Preface

This master thesis completes a *Master of Technology* degree. The thesis work has a total workload of 30 ECTS, and was performed as part of the *QD-IBSC* group at *Norwegian University of Technology and Science* (NTNU). I am very grateful for all the useful ideas the *QD-IBSC* group gave me. Their contributions were truly inspirational. This project would never been possible without feedback from my supervisor *Turid Worren Reenaas*. She has been very valuable and helpful, especially in the process of concretizing the project. *Bjørn-Ove Fimland's* great intuition and long experience was an important resource, which I was delighted to use. Finally, I would like to thank *Sedsel Fretheim Thomassen* for growing the samples and providing specific growth parameters and additional data without any hesitation.

Simon Riis Iden

(Januar 9th, 2012)

Abstract

The main focus of this master thesis work has been to image InAs *quantum dots* (QDs) using *atomic force microscopy* (AFM), to identify and evaluate various image processing methods used to estimate the volume of the InAs QDs. The InAs QDs studied in this thesis work, had been deposited on GaAs substrates, using solid-source *molecular beam epitaxy* (MBE) before the thesis work started. The total QD volume was determined for all samples, using eight different estimation methods. The purpose of estimating the total QD volume, was to compare the total volume to the deposited volume. Previous studies on similar samples, have indicated that the total volume can be larger than the deposited volume during MBE growth. This discrepancy is explained by incorporation of Ga from the substrate during growth. This was not observed in this thesis work. One possible explanation is that the samples have oxidized; resulting in a lower measured height. In addition, the relationship between atomic steps, defects and the appearance of large QDs were studied.

Two series of samples were studied: one in which the QD growth temperature was varied and one in which the amount of deposited InAs was varied. The total QD volumes were found to increase with the QD growth temperature and the deposited InAs thickness. Square-shaped defects and contours of 2D islands were observed in nearly all samples. Higher/multiple terraces seem to be related to regions of higher QD density.

Contents

Preface	i
Abstract	iii
1 Introduction	1
2 The physics of solar cells	5
2.1 Single p-n junction solar cells	5
2.1.1 Major loss mechanisms	5
2.1.2 Detailed balance analysis: single-junction solar cells	8
2.2 Intermediate band solar cells (IBSC)	11
2.2.1 Quantum dot in intermediate band solar cells (QD-IBSC)	13
2.2.2 Detailed balance analysis: exceeding the SQ-limit	15
3 Experimental methods and details	19
3.1 Sample growth	19
3.1.1 MBE basics	19
3.1.2 Experimental details: MBE	23
3.2 Sample characterization	24
3.2.1 AFM basics	24
3.2.2 Experimental details: AFM	28
4 Image processing and data extraction	31
4.1 Image processing	31
4.1.1 <i>Fast-Fourier Transform</i> (FFT) Filter	31
4.1.2 Estimated tip shape and size	33
4.1.3 Deconvolution	34
4.1.4 Processing AFM images	35
4.2 Extracting raw data	38
4.3 Estimating QD volume	41
4.3.1 Approximating the real QD surface	43
4.3.2 Deposited QD volume converted to equivalent Mono Layers	44
4.4 Statistical tools	45
4.4.1 Calculating the Quantum Dot(QD) density	45
4.4.2 Sample mean and sample variance	46

4.4.3	Pearson's product-moment coefficient	46
4.4.4	Error in the approximation of effective diameter	47
5	Results and discussion	49
5.1	AFM images	49
5.1.1	Sample <i>503-1</i>	50
5.1.2	Sample <i>503-2</i>	52
5.1.3	Sample <i>504-1</i>	53
5.1.4	Sample <i>514-2</i>	54
5.1.5	Sample <i>514-4</i>	55
5.1.6	Sample <i>544-1</i>	56
5.2	QD density	58
5.3	Projected QD area	60
5.4	QD height	62
5.5	Total QD volume	67
5.5.1	From $500\text{ nm} \times 500\text{ nm}$ AFM images	67
5.5.2	From $1\text{ }\mu\text{m} \times 1\text{ }\mu\text{m}$ AFM images	70
5.5.3	Sample homogeneity	72
5.5.4	Discussion: Estimates of total QD volume	80
5.5.5	Comparison of samples	82
5.6	AFM images of the wetting layer	87
5.6.1	Discussion: terraces and growth of QDs	93
5.7	Imaging of defects	94
5.7.1	Sample <i>503-1</i>	95
5.7.2	Sample <i>503-2</i>	96
5.7.3	Sample <i>504-1</i>	97
5.7.4	Sample <i>514-2</i>	98
5.7.5	Sample <i>514-4</i>	99
5.7.6	Sample <i>544-1</i>	100
5.7.7	Large QDs and Square Defects	101
5.7.8	Discussion: Large QDs and Square Defects	106
5.8	Discussion: errors and uncertainties	108
5.8.1	Error in <i>surface area method</i> (V_h)	110
5.8.2	Uncertainties	111
6	Conclusion	113
	Further work	115
	Bibliography	116

Chapter 1

Introduction

The photovoltaic (PV) effect was first discovered by the French physicist *Alexandre-Edmond Becquerel* in 1839. [1] He is by many historians regarded as the father of solar cells, widely known for his pioneering work. The first *photovoltaic* cell was invented only a few decades later [2], when solar energy was converted directly into electrical energy. A polish chemist named *Jan Czochralski* developed a method to grow single-crystal silicon in 1917. [3] Using this type of silicon, the efficiency of silicon-based solar cells increased dramatically. The very same method was utilized by *J.B. Little* and *Gordon K. Teal* at *Bell Labs* to fabricate single-crystal germanium p-n junctions in 1950. [4] The germanium p-n junctions became the first modern solar cell, and made a sensational front page in *The New York Times* in 1954. [5] The journalist wrote it was "*the beginning of a new era, [...] leading eventually to the realization of harnessing the almost limitless energy of the sun for the uses of civilization.*" [6] Such solar cells based on a pn-junction made from thin crystalline semiconductor wafers belong to the first generation solar cells.

The first generation (1G) solar cells have since their invention dominated the commercial market, accounting for 89% of the market share in 2007. [7] Extremely pure materials are needed to achieve a satisfying efficiency. The first 1G solar cells had as a consequence high production costs and were rather inefficient. The production cost are today dramatically reduced, as less energy-consuming and better manufacturing processes evolved. The efficiency of modern 1G solar cells are now exceeding 20% [8], with an average energy payback time of 1-2 years. [9]

Second generation (2G) solar cells aim to minimize production costs, and have a lower efficiency than 1G solar cells. Solar cells of second generation utilizes manufacturing techniques like electroplating and vapour deposition. The materials are deposited as thin films on cheap glass or ceramic substrates. This reduces the production cost, as less semiconductor material is needed. The first thin film solar cell of amorphous silicon was realized in 1976. The thin film photovoltaic cells were early adapted as power supplies on cheap toys and hand-held calculators. In 2010, the most successful thin film photovoltaic cells are made of *Cadmium Telluride* (CdTe) (4.7% market share) and polycrystalline silicon (5.2% share). [7]

The production costs of 2G are expected to fall even in the next few years, mostly due to new mass production factories in China, but also because of a greater demand for renewable energy on world basis. [10]

Third generation (3G) solar cells exceed the *Shockley-Queisser* (SQ) limit, proposing high performance and thus low-cost electricity. *Hans Queisser* and *William Shockley* proved in 1961 the existence of an upper limit to the energy conversion efficiency of any single-junction solar cell (the SQ-limit). The SQ-limit was under ideal conditions calculated to be 33.7% (1 suns), and 40.7% (46050 suns). [11] No single-junction PV cells can exceed the SQ limit. There are several approaches proposed to exceed the SQ limit: modifying the incident spectrum (light conversion), introducing multiple bandgaps (multi-junction or intermediate band solar cells), or generation of multiple charge carriers per photon and extraction of hot carriers. Silicon valley based *Solar Junction* developed in 2011 a multi-junction prototype with an efficiency of 43.5% ; the highest performing prototype PV cell ever built. [12]

The solar cell physics group at NTNU has decided to explore *intermediate band solar cells* (IBSC), and the realization of such cells using *quantum dots* (QD-IBSC). IBSCs are cheaper to manufacture and have a more robust design than the multi-junction cells. [13] The QDs could be a strategy to realize intermediate bands using well-known deposition techniques such as *molecular beam epitaxy* (MBE). [14]

QDs were first discovered in the early 1980s, and are described as nano-sized semiconductor crystals where the charge carriers are confined in all three dimensions. [15] QDs have applications beyond photovoltaics; in *light-emitting diodes* and fields like quantum computing [16] and medicine. [17] It has been shown that IBSCs have a theoretical efficiency limit of 63.2% at full light concentration (46050 suns). [18] Two or more IBSCs working in tandem can have an even higher conversion efficiency.

Until now, most QD-IBSCs studied are made of InAs QDs on GaAs substrates. [13] None of these have been successful in achieving efficiencies higher than the reference cell without QDs. [13] This is partly due to the fact that optimum QD properties have not yet been achieved. Therefore, additional fundamental studies of the QD growth process are needed. This thesis aims to investigate InAs grown on GaAs substrates, using *atomic force microscopy* (AFM) to determine the total QD volume. In this work, the total QD volume was found for six samples deposited with various different parameters. The samples were also examined for defects and other characteristics.

Chapter 2 summarizes the fundamental physics of both *single-junction solar cells* (SJSCs) and *intermediate band solar cells* (IBSCs). The experimental methods employed to fabricate and investigate the samples, and experimental details are presented in chapter 3. Image processing and tools related to the data analysis are outlined in chapter 4, together with a brief description of the various volume estimation methods and a discussion on conditions that might affect the AFM image quality. The results from two sample series are presented and discussed in chapter 5. Finally, everything is concluded in chapter 6. It is assumed that the reader has a formal background in physics.

Chapter 2

The physics of solar cells

This chapter covers the essentials of *single p-n junction solar cells* (SJSCs) and *intermediate band solar cells* (IBSCs), focusing on the underlying physics, and the advantages of IBSCs in particular. The solar cell designs are compared in terms of a detailed balance analysis. The final section describes how and why IBSCs can exceed the fundamental efficiency limit of SJSCs.

2.1 Single p-n junction solar cells

A single-junction (SJ) solar cell is a two energy band system consisting of a valence band (VB), and a higher conduction band (CB) (see Fig. 2.1). Solar cells are a *p-n junctions*, and convert light into electricity. The incoming photon energy is transformed to electrical energy in the cell, and a voltage is generated. This phenomenon is called the *photovoltaic effect*. Electrons get excited to a higher energy state, leaving behind empty states ("holes") in the VB (seen in Fig. 2.1). The process transfers the photon energy to an electron-hole pair (EHP). Equilibration and *thermalization* of the electrons and holes result in a steady-state population of electrons in the CB and holes in the VB, when the cell is illuminated. These two populations can be described by two quasi-Fermi levels: ϵ_{FC} for electrons and ϵ_{FV} for holes. The difference between ϵ_{FC} and ϵ_{FV} gives rise to a chemical potential, $\Delta\mu$, which can be extracted as electrical work. $\Delta\mu$ is zero at thermal equilibrium. When the material is exposed to sunlight, or if an external voltage is applied, a chemical potential is generated ($\Delta\mu > 0$).

2.1.1 Major loss mechanisms

There are four fundamental loss mechanisms in a SJSCs.

- ◇ A photon energy of $E_\gamma = h\nu < E_g$ can not excite electrons to the CB. Photons of an energy $E_\gamma < E_g$ will not be absorbed in a SJSC from the VB. This accounts for a spectrum loss of approximately 23% for Silicon SJSCs. [19]

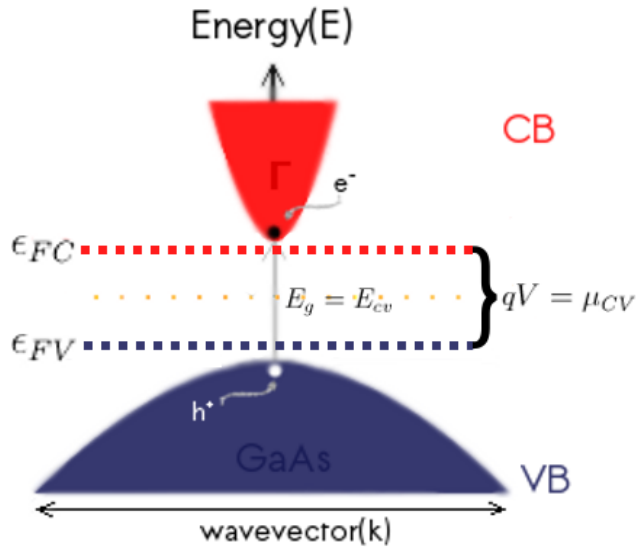


Fig. 2.1: Generation of Electron-Hole-Pairs (EHPs) in a direct bandgap semiconductor.

- ◇ All excess energy $\Delta E = E_\gamma - E_g$ for photons with $E_\gamma > E_g$, is lost through equilibration and thermalization (33% spectrum loss for silicon SJSCs). [19]
- ◇ Spontaneous emission (*radiative recombination*) leads to loss of charge carriers and thus current and voltage. Spontaneous emission occurs when an electron (e^-) falls spontaneously from the CB to the VB. The electron recombines with a hole (h^+) and emits a photon (γ), releasing energy.
- ◇ *Auger recombination* is a form of *non-radiative recombination* where an electron recombines with a hole in the VB, but with the excess energy given to another electron in the CB. The obtained excess energy is rapidly lost as lattice vibrations when the electron/holes thermalizes. Both momentum and energy are conserved in the process. It occurs frequently in indirect bandgap materials and semiconductors with high doping levels.

In an ideal cell only the fundamental losses mentioned above will be present. However, there are several other loss mechanisms. They are not considered as fundamental, but will all decrease the efficiency of the non-ideal solar cell. The four most common loss mechanisms are shown schematically in Fig. 2.2. These losses are:

- ◇ A significant amount of the incident light is reflected and is thus not absorbed. In the *Shockley-Queisser* limit below it is assumed that the solar cell is a perfect *blackbody*, absorbing all incoming light. This is often very far from the truth, as much of the light is scattered and/or reflected as it hits the solar cell surface, or transmitted through it.
- ◇ Non-radiative *Shockley-Read-Hall* (SRH) recombination is caused by defects or impurities in the material, often forming deep-level traps, with energy levels deep in the bandgap. [20] SRH recombination is a common recombination and generation mechanism in most real solar cells. In the *Shockley-Read-Hall* process an electron is trapped at an impurity or a defect level. In a second step, a hole is also trapped making the electron and the hole to recombine. The energy is not emitted as photons, but given up as phonons.
- ◇ *Shunt* and *series* resistance may cause noteworthy power losses, and are typically due to the manufacturing process. The effect of various *Shunt* resistance on the fill factor is illustrated in Fig. 2.3.

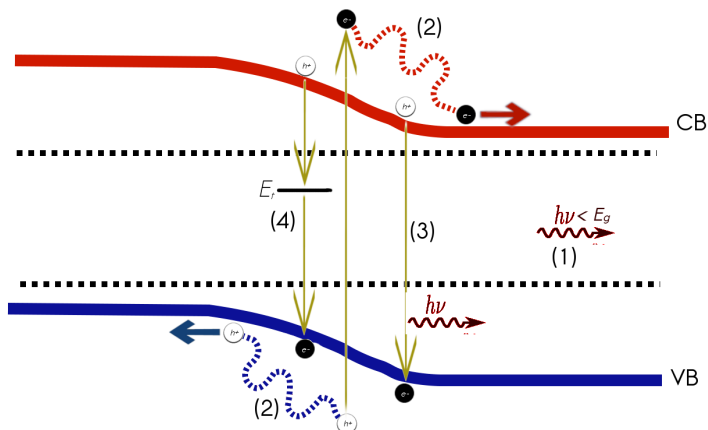


Fig. 2.2: The four most common loss mechanisms in a single p-n junction solar cell: (1) transmission of photons with $E_\gamma < E_g$, (2) loss due to thermalization, (3) spontaneous emission, and (4) *Shockley-Read-Hall* (non-radiative) recombination (not fundamental)

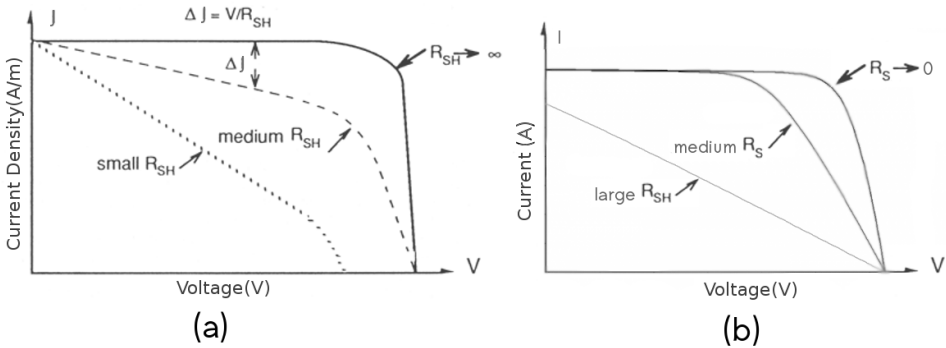


Fig. 2.3: The effect of (a) *shunt resistance* R_{SH} and (b) *series resistance* on a solar cell and $R_{SH} \rightarrow \infty$. The solar cell power $P = IV$ goes to a maximum when $R_s \rightarrow 0$.

Auger recombination is as mentioned unavoidable, but is normally a minor loss mechanism in solar cells with a low carrier density. *Shockley-Read-Hall* recombination, series resistance and *Shunt* resistance are avoidable to a certain degree, as it depends on the material.

2.1.2 Detailed balance analysis: single-junction solar cells

The principle of detailed balance could be used to find an upper theoretical limit for the efficiency of a ideal solar cell. A baseline energy is *always* emitted in a solar cell. Both the solar cell and the sun exchange thermal radiation with its surroundings, dynamically as a *blackbody*; obeying fundamental thermodynamical laws. The solar cell must be ruled by the principle of detailed balance: [19]

$$E_{in} = E_{out} \Rightarrow E_{sun} + E_{surroundings} = E_{SJSC} \quad (2.1)$$

The incoming energy can be expressed as the current density generated due to the absorption, and the outgoing energy as the current density due to radiative recombination plus the current density extracted from the cell. To keep a steady-state concentration of electrons constant, the rate of photons emitted must match the rate of photons absorption: [19]

$$J_{abs}(sun) + J_{abs}(surr.) = J_{abs} = J_{rad} + J(V) \quad (2.2)$$

J_{abs} is absorbed from the sun and surroundings, J_{rad} origins from spontaneous emission in the solar cell. Rearranging equation (2.2) gives the steady-state current $J(V)$ in the SJSC: [19]

$$J(V) = J_{abs} - J_{rad} \quad (2.3)$$

Assumptions

This limit was first derived by *Shockley* and *Queissier* in 1961. Some of the assumptions they made in the original paper are [11]

- ◇ the sun radiates as a *blackbody* at a temperature of $T_{sun} = 6000\text{K}$.

- ◇ the solar cell emits photons as a *blackbody* at an ambient temperature of $T_a = 300\text{K}$. $T_a = 300\text{K}$ represents approximately 7% of all available incoming energy at 1 sun concentration.
- ◇ all photons above the bandgap (i.e. $E_\gamma > E_g$) are 100% absorbed. None below bandgap photons are absorbed. As a result, the absorptance of this ideal cell is

$$a(E) = \begin{cases} 0, & E_\gamma < E_g, \\ 1, & E_\gamma \geq E_g, \end{cases} \quad (2.4)$$

- ◇ each absorbed photon produces one EHP.
- ◇ all carriers relax and create phonons. The excess energy of photons above the bandgap is converted to heat as the photons thermalise.
- ◇ the only recombination process is *spontaneous emission*.
- ◇ the carriers diffuse without loss to the electrodes. The carriers that do not radiatively recombine can be extracted.
- ◇ carrier mobilities are infinite and *ohmic* contacts are applied, and subsequently only electrons can be extracted from the CB and holes from the VB.
- ◇ the back of the cell is a perfect mirror (100% reflection). Radiation generated the cell can only escape through the illuminated surface. The illumination is *isotropic*.

The SQ-limit: the limit to solar cell efficiency

Integrating over all photon energies, Eq. 2.3 gives the net cell current density for an ideal solar cell [19]

$$J(V) = q \int_0^\infty [(1 - R(E))] a(E) \{b_s(E) - (b_e(E, qV) - b_e(E, 0))\} dE \quad (2.5)$$

where E is the photon energy, $R(E)$ the reflectivity and $a(E)$ the absorptivity. They are determined by material properties and optical path length. b_e is emitted spectral photon flux, expressed as

$$b_e(E, \Delta\mu) = \frac{2 F_a}{h^3 c^2} \left(\frac{E^2}{e^{\frac{E - \Delta\mu}{k_B T_s}} - 1} \right) \quad (2.6)$$

where $b_e(E, 0)$ is the incoming photon flux from the ambient, and $b_s(E)$ the incident spectral photon flux normal to the surface - defined as

$$b_s(E) = \frac{2 F_s}{h^3 c^2} \left(\frac{E^2}{e^{\frac{E}{k_B T_s}} - 1} \right) \quad (2.7)$$

F_s and F_a are geometrical factors resulting from an integration over the relevant solid angle, and F_a also depends on the refractive index of the surrounding medium (≈ 1 in air).

$$\begin{aligned} F_s &= \pi \sin^2 \theta_{sun} \\ F_a &\approx \pi \end{aligned}$$

where $\sin^2 \theta_{sun} = 2.16 \cdot 10^{-5}$ is the angular range of the sun. F_s corresponds a hemisphere (π) at surface of the sun, but is on Earth reduced to $F_s = 2.16 \cdot 10^{-5} \pi$ by a factor of $4.6 \cdot 10^4$ [19]

For an ideal cell $R(E) = 0$, $a(E) = 1$, $E > E_g$ and

$$J(V) \cong q \int_{E_g}^{\infty} \{b_s(E) - b_e(E, \Delta\mu)\} dE \quad (2.8)$$

where $b_e(E, 0)$ is omitted since it is much smaller than $b_s(E)$. From this expression we see that the current density only depends on the bandgap of the cell for a given photon flux. The conversion efficiency of the solar cell can be expressed as

$$\eta = \frac{V \cdot J(V)}{P_s} \quad (2.9)$$

where the incoming power density P_s is given by

$$P_s = \int_0^{\infty} E \cdot b_s(E) \cdot dE \quad (2.10)$$

The energy conversion efficiency η is at a maximum when

$$\frac{d}{dV} (J(V) \cdot V) = 0 \quad (2.11)$$

The solar cell has an optimum bandgap that maximizes the efficiency for a given illumination. The conversion efficiency η has a maximum at the optimum bandgap, called the *Shockley-Queisser* (SQ) limit. A plot of SQ limit at two different light concentration are presented in Fig. 2.4. Fig. 2.4 shows that the SQ limit is 40.7% at full light concentration, and 30.5% for unconcentrated sun light.

In this section we have seen the limitations of single-junction solar cells (SJSCs), although several assumptions are made in SQ limit. It is assumed the cell consists of only one single p-n junction fine-tuned to the solar spectrum. One way to exceed the SQ limit is by introducing an additional, intermediate, band in the bandgap of the solar cell material. The resulting intermediate band solar cell is presented in the following section.

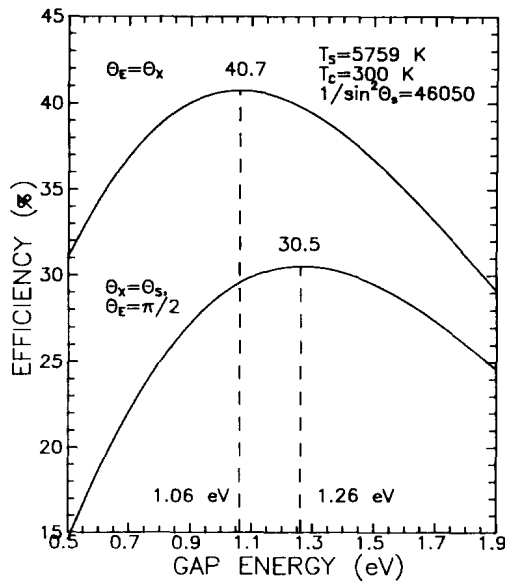


Fig. 2.4: The limiting efficiencies for photovoltaic energy conversion, as a function of the bandgap. The light concentration is $X=1$ (lower curve) and $X=46050$ (upper curve). [21]

2.2 Intermediate band solar cells (IBSC)

Intermediate band solar cells (IBSC) are p-n junctions with an intermediate band material placed between the n- and p-type semiconductors (see Fig. 2.5). An IBSC has the potential to exceed the limits of conventional single-junction solar cells, by increasing the current, but at the same time maintaining the output voltage. Ideally, it has a limiting conversion efficiency of 63.2% at light concentration of 46050 suns. [18] This is a potential improvement of 55% compared to single-junction solar cells, but similar to ideal 3J tandem cell. There are several methods proposed to achieve the intermediate bands. One approach is *quantum dots* (QDs). However, few high performance quantum dot intermediate band solar cells (QD-IBSCs) have been realized to date.

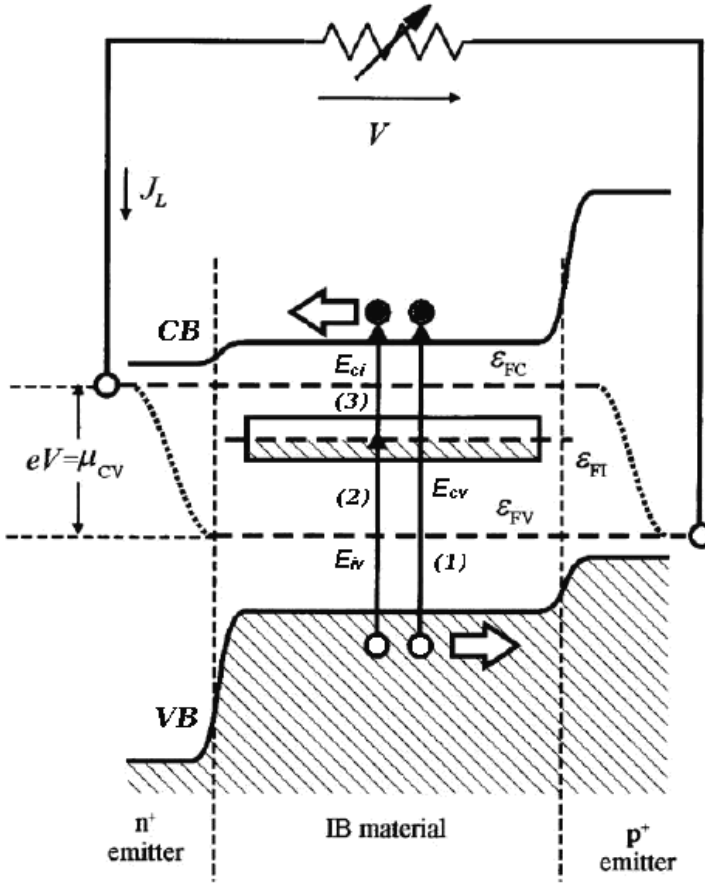


Fig. 2.5: A schematic drawing of an ideal IBSC exposed to light, in forward bias. The intermediate band material is squeezed in between a p and a n semiconductors.

As shown in Fig. 2.5, an *intermediate band* (IB) the main gap $E_g = E_{cv}$ into two smaller bandgaps, namely, E_{iv} and E_{ci} . The IB is a (thermally) isolated energy band located between the *conduction band* (CB) and the *valence band* (VB). Each energy band is described by their own quasi-Fermi level, as indicated by the dashed lines. Physically, this means that the thermalization within a band is a much faster process than carrier recombination between the bands.

There are three mechanisms that generate electron-hole pairs (EHP) in an IBSC.

1. A direct transition from VB to CB ((1) in Fig. 2.5). This requires one photon with energy $E_{\gamma 1} \geq E_g$.
2. Exciting electrons from the VB to the IB (2), followed by a transition from IB to CB (3). This requires the absorption of two photons, one for each

transition with energy $E_{iv} \leq E_{\gamma_2} < E_{cv}$ (2) and $E_{ci} \leq E_{\gamma_3} < E_{cv}$ (3).

The electrons are extracted from the CB on the n-side, and holes from the VB on the p-side.

In the ideal case, with infinite mobilities $\Delta\mu = E_{Fn} - E_{Fp} = qV$. Note that the qV in general will be larger than in a SJ cell because E_g can be larger. J_{sc} is also increased due to absorption of low energy photons. Once fully mastered, two or more IBSCs could work in tandem at very high efficiencies. [13]

2.2.1 Quantum dot in intermediate band solar cells (QD-IBSC)

Quantum dots (QDs) can be utilized to take advantage of the IBSC concept in practice. The first prototypes of QD-IBSC were fabricated in 2004. [22] Ever since, much progress has been made to implement the QD-IBSC design. This work studies QDs based on the InAs/GaAs(001) system, a possible QD-IBSC. This section covers some theory on *quantum dots* and how QDs can change semiconductor properties.

Self-assembled QDs are "artificial atoms"; nano-crystal semiconductors with a size of a few nm in diameter, embedded in a higher bandgap semiconducting material. QDs exploit 3D quantum confinement, and is a possible strategy to implement the intermediate band concept. [18] The electronic states become quantized at discrete energy levels, if the region of confinement is smaller than the *De Broglie* wavelength of the electrons:

$$\lambda = \frac{h}{p} = \frac{h}{\sqrt{3 m^* k_B T}} = \frac{1.22 \text{ nm}}{\sqrt{E_{kin}(\text{eV})}} \quad (2.12)$$

where m^* is the effective mass, T the crystal temperature and E_{kin} the kinetic energy of the charge carrier. The effect of quantization can be pronounced for crystals of an mesoscopic scale, considering that the effective mass of a charge carrier can be much smaller than the mass of a free charge carrier.

The following theory aims to explain why there are discrete energy levels inside QDs. A quantum mechanical approach is necessary, in order to understand the behaviour of the QDs at a mesoscopic level. A electron or hole can be treated like an isolated particle inside empty quantum confinement, using the solid-state effective mass (m^*). Any excess charge carriers populate the energy levels to minimize *Coulomb* interactions. The first assumption is that the quantum confinement is spherical with a radius R_0 . Recall that the spherical harmonics satisfy [23]:

$$\hat{l}^2 Y_{lm}(\theta, \phi) \equiv \left\{ -\frac{1}{\sin^2 \theta} \left[\sin \theta \frac{\partial}{\partial \theta} \left(\sin \theta \frac{\partial}{\partial \theta} \right) + \frac{\partial^2}{\partial \phi^2} \right] \right\} Y_{lm}(\theta, \phi) = l(l+1) Y_{lm}(\theta, \phi) \quad (2.13)$$

Eq. (2.13) substituted into the *Schrödinger equation* gives an eigenvalue equation:

$$\left\{ -\frac{\hbar^2}{2 m^* r^2} \frac{d}{dr} \left(r^2 \frac{d}{dr} \right) + \frac{\hbar^2 l(l+1)}{2 m^* r^2} + V(r) \right\} R(r) = E_r R(r). \quad (2.14)$$

Eq. (2.14) can be rearranged to the radial function Eq. (2.15) by substituting $u(r) \stackrel{\text{def}}{=} rR(r)$:

$$-\frac{\hbar^2}{2m^*} \frac{d^2 u(r)}{dr^2} + V_{\text{eff}}(r)u(r) = E_r u(r) \quad (2.15)$$

which corresponds to the *Schrödinger equation* for radial function $u(r)$ and an effective potential

$$V_{\text{eff}}(r) = V(r) + V_c = V(r) + \frac{\hbar^2 l(l+1)}{2m^* r^2}, \quad (2.16)$$

where V_c is called the centrifugal barrier and l is a quantum number. The charge carrier is confined in all spatial dimensions by a potential $V(r)$:

$$V(r) = \begin{cases} 0, & 0 < r < R_0 \\ \infty, & \text{otherwise} \end{cases}, \quad (2.17)$$

The problem above can be solved analytically, and gives

$$E_l = \frac{u_{l,k}^2 \hbar^2}{2m^* R_0^2} \quad (2.18)$$

where $u_{l,k}$ is the k^{th} zero of the *Bessel function* J of order l (J_l). Eq. (2.18) proves that an excess charge carriers trapped in a spherical semiconductor QD must obey discrete energy states. The discrete energy states are found in other shapes QD as well, including pyramidal, lens-shaped and box/cubic QDs. [24] The energy states are quantized in atoms, defined precisely within the limit of *Heisenberg's* uncertainty relation. The electron energy in crystals is a function of momentum, and have continuous densities of states, energy bands and gaps. The "atom-like" electronic properties in nano-crystals originate from the 3D quantum confinement of excitations and carriers. Any subtraction or addition of charge carriers (electrons and holes) completely changes the properties of the QD.

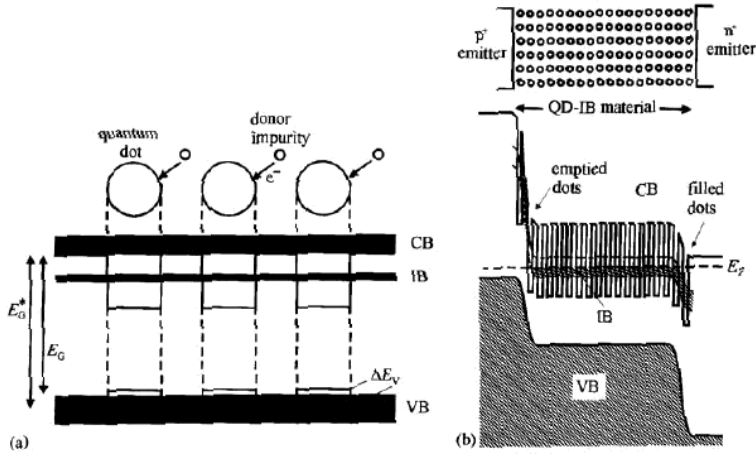


Fig. 2.6: (a) schematic drawing of an intermediate band formed by an array of QDs. The wave-function in each QD overlap to form an intermediate band. (b) A QD-IBSC in equilibrium (simplified energy band diagram). [25]

Each QD will act as a spherical potential well when embedded in a bulk material with a higher bandgap. If the QDs are packed closely enough, the wave-functions will overlap and form a band. [26] Fig. 2.6 (b) shows the formation of an intermediate band by the overlap of confined wave-functions: the fundamental idea of a QD-IBSC. It is possible to fine-tune the energy, band and width of the intermediate band by adjusting the QD size, shape, density and composition. The only QDs to be discussed in this report is InAs; a binary III-IV compound with a relatively small bandgap in an GaAs matrix. [27]

2.2.2 Detailed balance analysis: exceeding the SQ-limit

The principle of detailed balance is very important in calculating the limits in solar cell efficiency. The same assumptions are made as in the detailed balance analysis of SJ cells (see **Assumptions** in Sec. 2.1.2), and in addition we assume: [19]

- ◇ absorption of photons by electron transitions from VB to IB, and between IB and CB may also take place - in addition to VB to CB.
- ◇ there are three separate quasi-Fermi levels (see Fig. 2.5), one for each band: ϵ_{VB} , ϵ_{IB} and ϵ_{CB} .
- ◇ the sun light is concentrated to light equivalent to 46050 suns.

As in the SQ model it is assumed that any irreversible loss mechanism is prevented. The photons are absorbed and emitted continuously inside the semiconductor.

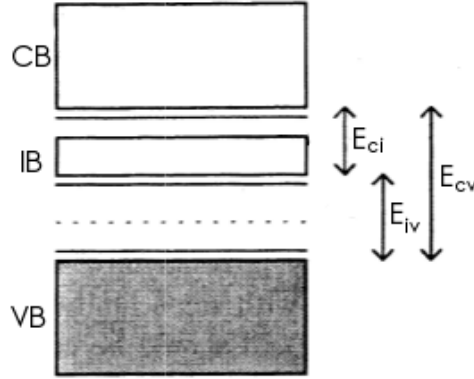


Fig. 2.7: Modified from [19]. An energy band diagram of an IBSC with two conduction bands IB and CB and one single valence band.

Assume a three band cell with a energy band diagram, as shown in Fig. 2.7. There are three types of photon absorption events possible, depending on the photon energy (E_γ)

- ◇ $E_\gamma > E_{ci}$ promotes electron from IB to CB
- ◇ $E_\gamma > E_{iv}$ promotes electron from VB to IB
- ◇ $E_\gamma > E_{cv} = E_g$ promotes electron from VB to CB

All of the absorption events above occur over a constricted energy range: E_g to ∞ , E_{g2} to E_g and E_{g1} to E_{g2} , respectively. There is a net current density of electrons leaving the CB contact and returning to the VB - delivering a $J(V)$ to an external load. The net current density could be calculated as follows, assuming unit absorptivity in each of the energy ranges above [19]

$$J(V) = [N(E_{cv}, \infty, T_s, 0) - N(E_{cv}, \infty, T_a, \epsilon_{CB} - \epsilon_{VB})] \\ + [N(E_{iv}, E_{cv}, T_s, 0) - N(E_{iv}, E_g, T_a, \epsilon_{IB} - \epsilon_{VB})]$$

where ϵ_{VB} , ϵ_{IB} and ϵ_{CB} are the quasi Fermi levels of the VB, IB and CB, accordingly, and [18]

$$N(\epsilon_n, \epsilon_m, T, \mu) = \frac{2}{h^3 c^2} \int_{\epsilon_n}^{\epsilon_m} \frac{\epsilon^2}{e^{\frac{\epsilon - \mu}{kT}} - 1} d\epsilon \quad (2.19)$$

is the maximum absorbed or emitted photon flux density in the energy range from ϵ_n to ϵ_m . For a cell in *steady state*, the net current from VB to IB must equal the current from IB to CB. This can be expressed as [19]

$$q [N(E_{ci}, E_{iv}, T_s, 0) - N(E_{ci}, E_{iv}, T_a, \epsilon_{CB} - \epsilon_{IB})] \\ = q [N(E_{iv}, E_{cv}, T_s, 0) - N(E_{iv}, E_{cv}, T_a, \epsilon_{IB} - \epsilon_{VB})]$$

The quasi *Fermi levels* must also satisfy

$$qV = \epsilon_{CB} - \epsilon_{VB} = (\epsilon_{IB} - \epsilon_{VB}) + (\epsilon_{CB} - \epsilon_{IB}) \quad (2.20)$$

As for the SJSC there will always be a voltage V that maximizes the product $J(V) \cdot V$, but now for a given E_{cv} and E_{ci} . The energy conversion efficiency is found by dividing the peak power by the power of the incoming light, implying that the optimum efficiency of an IBSC is only a function of the bandgaps and the photon flux. Fig. 2.8 shows that an ideal IBSC have a limiting efficiency of 63.2% for $E_g = E_{cv} = 1.93eV$ and $E_{iv} = 0.7eV$ [18], higher than the similar efficiency limit of SJSCs (40.7% [11]) or two-terminal ideal tandem cell (55.5% [28]). As mentioned earlier, one reason is that the QDs have not been optimized yet. This thesis aims to contribute the understanding of QD growth.

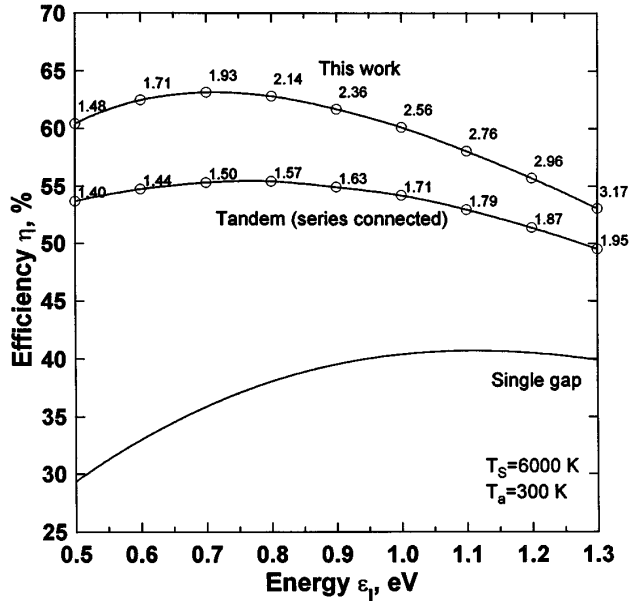


Fig. 2.8: Reprinted from [18]. The energy conversion efficiency limit for an intermediate band solar cell (IBSC), a two-terminal ideal tandem cell, and a single-junction solar cell (SJSC). The numbers on the curve indicate the highest bandgap (i.e. $E_g = E_{cv}$ for IBSC). The calculated efficiency assumes light concentrated equivalently to 46050 suns (max. light concentration).

Ideal solar cells are of course not achievable in reality. QD-IBSCs have been successfully demonstrated [13], but have yet to set great records and a deeper understanding of how the QDs are formed, is needed. This thesis is a small piece in the puzzle to fully understand QD growth. In the next chapter we will review the experimental methods employed to deposit and investigate *quantum dots* for *QD-IBSC* at NTNU, namely, *molecular beam epitaxy* (MBE) and *atomic force microscope* (AFM).

Chapter 3

Experimental methods and details

This chapter covers details related to the experiments, and illuminates two general topics: sample growth (Sec. 3.1) and sample characterization (Sec. 3.2). Sec. 3.1 covers some basic theory on the experimental methods used to fabricate the samples, using *molecular beam epitaxy* (MBE) Sec. 3.2 outlines how the samples were investigated, using *atomic force microscopy* (AFM). The sample growth and sample characterization sections both begin with an overview over the basics of the experimental methods, followed by the experimental details, focusing more on the actual lab parameters and instrumentation used.

3.1 Sample growth

3.1.1 MBE basics

MBE is a method for depositing epitaxial, thin films on a substrate and the essential parts are shown schematically in Fig. 3.1. The substrate is placed on a heater in a ultra-high vacuum chamber, and usually has the form of a full or 1/4-wafer. Ultra-pure elements are heated in separate effusion cells until they sublime or vaporize. The material flux is determined by the temperature of the effusion cell. A shutter in front of each cell turns the flux of the material on and off. Fine-tuning the flux ratios of the molecular beams determines the growth and the composition of the deposited material.

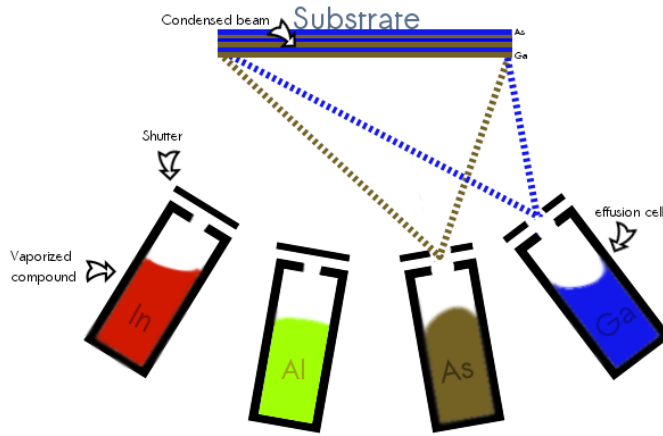


Fig. 3.1: A schematic drawing of a MBE. Molecular beams are directed to a heated and rotating substrate. Shutters in front of the effusion cells turn the beams on and off.

The beam of gaseous elements are directed towards the surface of the substrate. The growth rates are often quite low (typically μm per hour), allowing epitaxial growth. There is very little interaction between the molecular beams before they reach the substrate. The substrate holder is normally rotating, and heated during deposition. The molecular beams quickly condense on the substrate surface. The layer will relax and form self-organized QDs, if the deposited layer has a larger lattice constant than the substrate and a critical thickness is exceeded. The growth mode is called *Stranski-Krastonov* growth and is further described in the following section.

The Stranski-Krastonov growth mode

Stranski-Krastonov (SK) growth is based on lattice mismatch. The lattice mismatch is about 7% in the InAs / GaAs system. [27] SK growth mode was first described by *L. Von Krastanow* and *Ivan N. Stranski* in 1939, and follows a two-step process:

1. a thin film, often a few monolayers thick, is deposited in a layer-by-layer fashion on the surface.
2. if the thin film is deposited beyond a critical thickness, the growth mode rapidly changes to 3D growth of consisting islands and QDs are formed. The critical thickness is determined by the build-up of strain in the film.

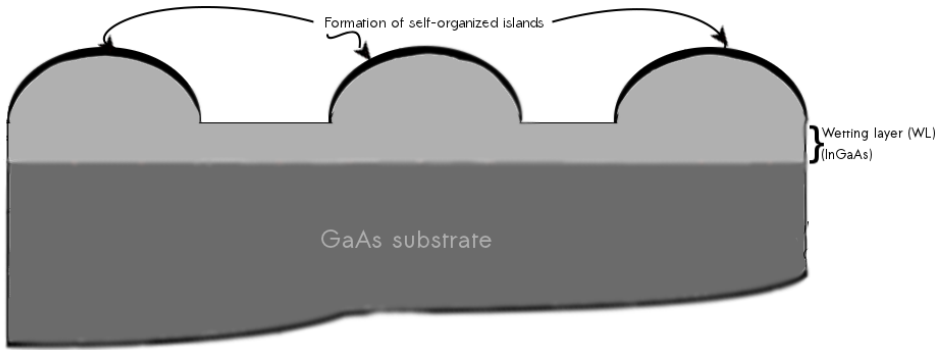


Fig. 3.2: The formation of self-organized absorbate islands(InAs) on a 2D wetting layer (WL).

Layer-plus-island growth is perhaps a more descriptive name of the SK growth mode. The critical thickness of InAs grown on GaAs is around 1.6-1.7 ML. Once exceeding this limit, the InAs islands form by self-organization. [29] Fig. 3.2 is an illustration of how QDs form on top of the wetting layer. The QDs are typically a few nm in height, and some tens of a nm in diameter. The QDs have a variety of different shapes; conical, pyramidal (Fig. 3.3), semi-spherical or lens-like shape. There is direct relationship between the height of the centroid point above the wetting layer(WL) and the internal strains in the QD. Hence, a lens-like shape is more stable than a semi-spherical or conical shape. InAs QD on a GaAs substrate grown by MBE typically have a low height of around 3 nm, which can vary in size by more than 10%. [30]

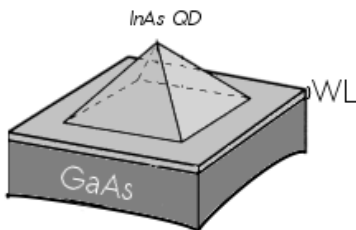


Fig. 3.3: One of many possible QD shapes: a pyramidal QD

Onset of QD growth

2D islands on terraces are atomic steps that form before the nucleation of 3D features like QDs. Fig. 3.4 illustrates how 2D islands form during MBE growth for the InAs/GaAs(001) system. The value indicated above Fig. 3.4 is the thickness of deposited InAs. One observation is that the topography is completely free of all 3D features for 1.42 ML deposited. As the amount of InAs increases, small QDs form on the steps of the 2D islands. The size of the 2D island is strongly dependent on growth conditions.

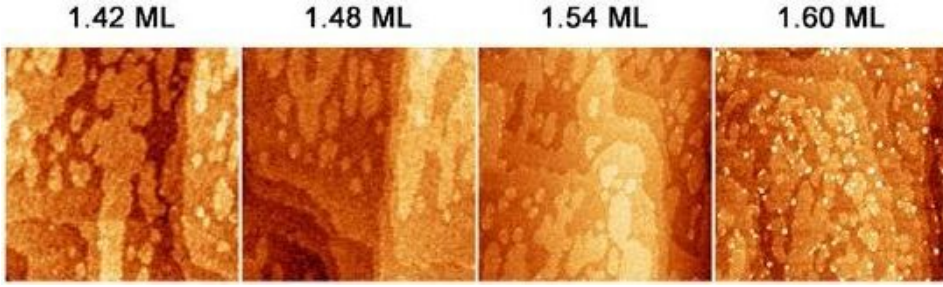


Fig. 3.4: $1\ \mu\text{m} \times 1\ \mu\text{m}$ images of topography changes during continuous MBE growth of InAs on GaAs. The amount of InAs varies from 1.42 ML to 1.60 ML from left to right. [31]

Mass transport mechanisms

A phenomenon recently discovered [32] is the effect of erosion for dots near a step edge of a terrace. Various types of surface mass transport in the InAs/GaAs 2D–3D transition have been documented in several studies, for example [31]. The diffusive mass transport may be explained by several explicit mechanisms with various times scales. Fig. 3.5 (A–C) illustrates how erosion might happen, above the step edge, and on a terrace (Fig. 3.5 (D)).

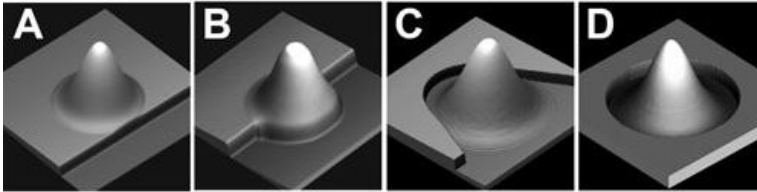


Fig. 3.5: Schematic drawing of erosion. (A) illustrates a nucleated QD above the step edge, before erosion. The same QD has eroded some of the step edge in (B), and the step is completely eroded in (C). (D) is after erosion. Reprinted from *Placidi et al.* [32]

In addition to erosion, several studies suggest that a process called In–Ga intermixing occurs during growth of the WL. [33] The QDs contain a significant amount of Ga after nucleation, drawn from the substrate below. Some studies have implied that the post-growth QD volume is larger than the deposited in the wetting layer during growth. [31] The excess mass could be explained by a mass transport from the substrate to the QDs. The mass transport happens during an initial stage of the transition in the 2D→3D phase, supported by observations of growth interruption using RHEED transition patterns. [32]

3.1.2 Experimental details: MBE

A *Varian Gen II Modular MBE* machine was used to deposit the samples described in this study. [34] The MBE machine has a 400g SUMO source for In, a dual filament source for Ga and a valved cracker source for As_2 . The InAs QDs were deposited by *Sedsel Fretheim Thomassen* on an GaAs substrate, mounted on a *Veeco 1/4-wafer* holder. The structure of the samples is shown in Fig. 3.6. The nominal growth parameters for all samples are listed in Table 3.1.

Table 3.1: The growth parameters of the samples: growth temperature, In growth rate and deposited InAs thickness. The In:As₂ ratio was approximately 1:40, and As flux $2 \cdot 10^{-6}$ torr for all samples.

Sample	Temperature ($T_{\text{QD}} \text{ }^\circ\text{C}$)	Growth rate (ML/s)	Thickness (Θ_{InAs} ML)
503-1	475	0.10	2.3
503-2	480	0.10	2.3
504-1	490	0.09	2.3
514-2	480	0.08	2.1
514-4	480	0.08	1.9
544-1	455	0.09	2.3

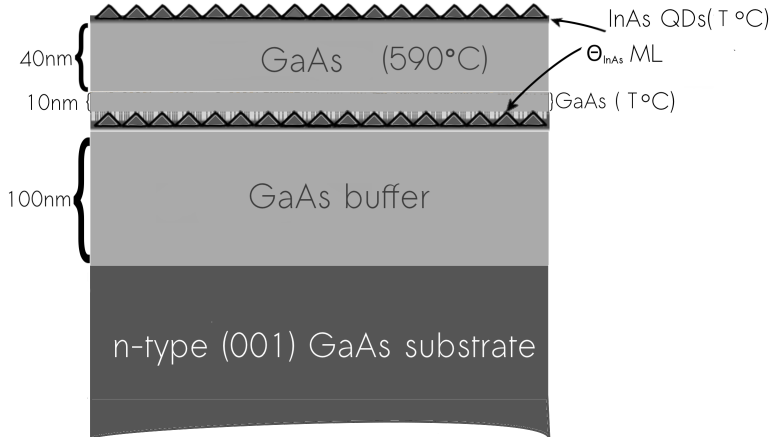


Fig. 3.6: A schematic drawing of the sample structure. The epitaxial layers of the substrate were grown at different temperatures. T_{QD} is the growth temperature for the InAs QDs plus the first 10 nm of the GaAs spacer. Two layers of InAs QDs, each with a thickness Θ_{InAs} . T_{QD} and Θ_{InAs} are listed in Table 3.1.

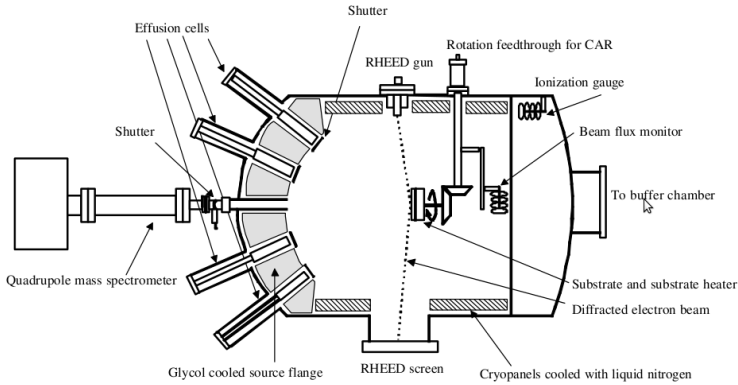


Fig. 3.7: A schematic illustration of the growth chamber. Only four effusion cells are included. [34]

The samples were deposited in the MBE growth chamber (see Fig. 3.7). The pressure in the growth chamber was $7 \cdot 10^{-9}$ Torr, before opening the beam shutters in the front of the effusion cells. The source flange was cooled with glycol (temp. -20°C), and the growth walls with liquid nitrogen. The temperature was measured by a pyrometer and a thermocouple in the proximity of the heater. The sample was heated to selected temperatures, and the layers grown epitaxially.

3.2 Sample characterization

This section contains the essentials of the experimental methods employed to characterize the QDs, namely *atomic force microscope* (AFM).

3.2.1 AFM basics

Scanning probe microscopy (SPM) is a branch of surface sensitive techniques where a sharp tip is scanning across a surface. The two most notable SPM types are *scanning tunnelling microscope* (STM) and AFM. STM was first discovered and developed by Gerber, Weibel, Binnig, and Rohrer in 1982 (IBM in Zürich, Switzerland). Gerber, Quate and Binnig invented the first AFM in 1986 as a joint intellectual endeavour between IBM and Stanford University (USA).

AFM has three primary modes of operation: tapping, non-contact and contact. In *TappingMode*TM AFM, the piezoelectric tube oscillates very rapidly. The tip softly "taps" on the sample surface during scanning when the cantilever is at its maximum extension. The feedback loop maintains a constant amplitude by changing the tip, and translates it to a topographic image of the surface. The piezoelectric tube oscillates at an even higher frequency in *Non-Contact Mode* AFM, but with a very small amplitude. The cantilever is influenced by *Van der Waals* forces, which

causes the amplitude and resonance frequency to decrease. The tip never touches the surface, but oscillates above the surface and generates an AC signal from the cantilever. The AC signal can be translated to a image of the surface. *Contact Mode* AFM operates by scanning a tip attached to the end of a cantilever across the sample surface while monitoring the change in cantilever deflection with a split photo-diode detector.

All measurements in this work were carried out using *Contact Mode* AFM. In addition, *Tapping Mode* AFM were explored in the start-up phase of the project to see if the *Contact Mode* tip made any scratches in the material. *Contact Mode* AFM was chosen because the samples were assumed to have a very smooth surface, taken into consideration the small size of the QDs. Therefore, high scan speeds can be used.

Contact Mode AFM

A schematic illustration of the AFM instrument is shown in Fig. 3.8. The piezotube moves relative to the stationary cantilever. The sample is placed on the top of the piezotube.

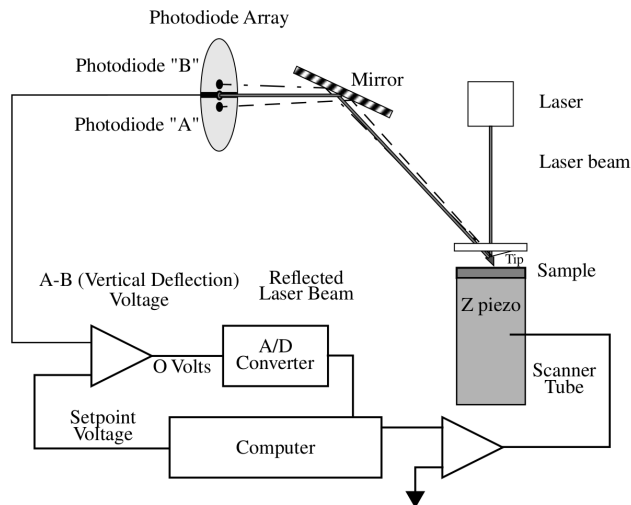


Fig. 3.8: A schematic of the active components in a *Contact Mode* AFM. The feedback loop regulates the cantilever so the deflection remains constant. [35]

A sharp tip is attached to the end of a cantilever. Laser light is reflected from the upper side of the cantilever to a split photo-diode detector. This makes it possible to measure the deflection of the cantilever.

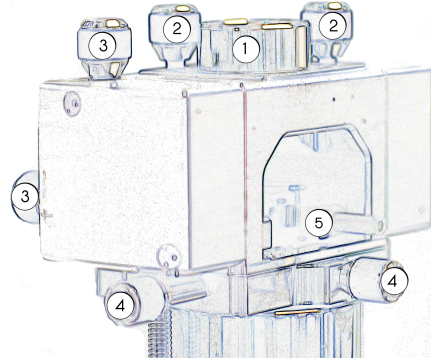


Fig. 3.9: A photograph of the AFM instrument, processed by a edge-detect filter. The laser source and mirror (1), laser aiming knobs (2), photodiode adjustment screws (3), X/Y head translator (4) and tip/sample (5).

A constant deflection (*set-point*) is maintained between the sample and cantilever by a negative feedback loop. The topography is measured by scanning the tip over the sample surface, back and forth. The piezoelectric scanner moves horizontally in two directions. The tip is maintained in contact with the surface, thus the name *Contact Mode*. Essentially, the force between the sample and the tip is usually held constant (*set-point*). The force \vec{F} could easily be calculated from Hooke's law:

$$\vec{F} = -k \cdot x \cdot \hat{e}_x$$

where k the spring constant and x the deflection of the cantilever. The spring constant varies in the range from 0.01 N/m to 1.0 N/m, and is determined by the thickness of the cantilever.

The laser spot is adjusted and aligned properly on the cantilever upper side by adjusting knobs (2), in Fig. 3.9. The position of the tip relative to the sample is adjusted by the X/Y head knobs (4). The photo-detector is adjusted by (3), where the upper and the lower knob corresponds to vertical and horizontal deflection. Before the tip engages, the vertical deflection is set to a value 2-3V lower than the set-point voltage. The starting value of vertical deflection determines how much force the tip would have as it jumps to contact on the surface. Larger force typically means better imaging, but increases the risk of damaging or contaminating the tip and sample. The initial *set-point* voltage is usually 0.0 V or 2.0 V.

Horizontal deflection is only important when measuring friction and lateral forces (*lateral force microscopy* (LFM)), and is recommended to be set to the default value of 0.0V when in *Contact Mode*.

Piezoelectric scanners

The AFM has an extremely high precision in both the the horizontal X/Y and the vertical Z direction. The scanning precision is made possible by a piezoelectric tube. A piezoelectric material contracts or extends proportional to an applied voltage. Piezoelectricity is electricity generated in response to a mechanical strain, or reversely a pressure created by an applied voltage.

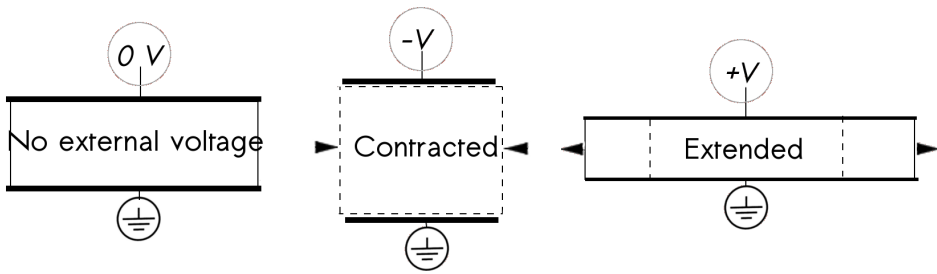


Fig. 3.10: How a piezoelectric material reacts to positive, negative and zero applied voltage.

There are five independent electrodes in the piezoelectric tube. The tube is controlled by five electrodes, as depicted in Fig. 3.11. The piezoelectric crystal expands and compresses, as an applied voltage varies. There is one large, piezoelectric ring controlling the vertical Z direction. The horizontal directions are regulated by four electrodes, namely, X/\bar{X} and Y/\bar{Y} . The \bar{X}/\bar{Y} act as counter-forces to X/Y , navigating the tip in the horizontal plane.

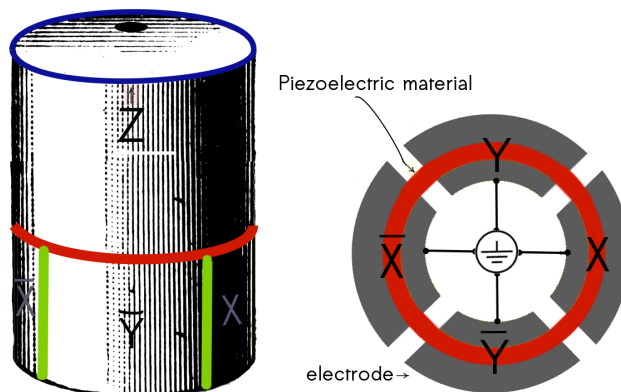


Fig. 3.11: A typical piezotube with five electrodes (Z , X , \bar{X} , Y , \bar{Y}). A voltage is applied in selected piezoelectric sections, causing them to extend or retract. Consequently, the lower edge of the tube moves in a desired X , Y or Z direction.

3.2.2 Experimental details: AFM

The samples were examined in two different *Digital Instruments NanoScope™* multi-mode SPMs, with *PicoForce* force spectroscopy control module from *Veeco*. The multi-mode SPM was operated in *Contact Mode* AFM (see previous section). The **sample/line** was generally set to 512 px, but set to at least 1024 px for $10\ \mu\text{m} \times 10\ \mu\text{m}$. Four different scan sizes were used at each location: $500\ \text{nm} \times 500\ \text{nm}$, $1\ \mu\text{m} \times 1\ \mu\text{m}$, $2\ \mu\text{m} \times 2\ \mu\text{m}$ and $10\ \mu\text{m} \times 10\ \mu\text{m}$. The software used a graphical user interface (GUI) to control and operate the AFM: *Nanoscope*© version 7.05 (*SINTEF* AFM) and 8.15 (*Biophysics* AFM). All scans were conducted using different scan angles, scan rates and various feedback parameters and force calibration constants. Fig. 3.12 shows the height (black/red) and tip deflection (grey-scales) of a typical $1\ \mu\text{m} \times 1\ \mu\text{m}$ AFM image. The visible "grains" are self-organized *quantum dots*.

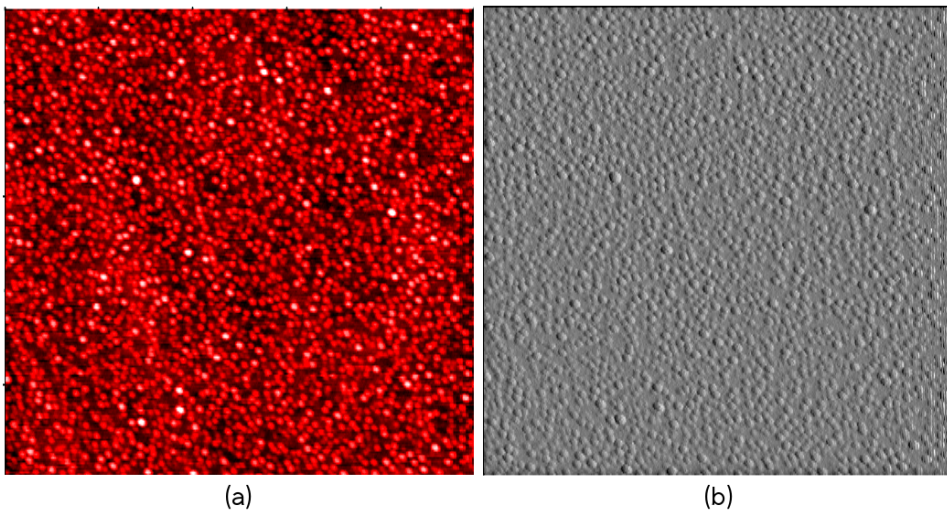


Fig. 3.12: $1\ \mu\text{m} \times 1\ \mu\text{m}$ AFM image. Two data type channels were used: (a) height (black/red) and (b) deflection (grey-scales). The height scale in (a) goes from 0 nm (black) to 5 nm (red) as a gradient.

Cantilever probes

In contact mode AFM, the probes used were made of silicon nitride (Si_3N_4). The probes consist of a cantilever with a sharp tip attached below, as shown in Fig. 3.13. Si_3N_4 has advantageous material properties, such as a very low coefficient of thermal expansion. It also has a superior wear resistance and strength over a wide range of temperatures, as shown in Table 3.2. The cantilever is coated with a thin gold coating to increase laser reflectivity, as seen in the microscope image of the *Contact Mode* probe in Fig. 3.14. In *Contact Mode AFM* it is crucial to have a cantilever which is easily deflected by small forces.

Table 3.2: Data sheet for the probe used in contact mode AFM (*OTR4-10*). [35] The values in the parentheses are for the large cantilever. See Fig. 3.13 for more details on the geometric parameters.

Triangular cantilevers	
Structure	amorphous
Material	Silicon Nitride
Density	3.29 g/cm ³
Thermal Conductivity	30
Coefficient of Thermal Expansion	3.3
Geometric angles	36 ± 2 °C
Length, cantilever	100 (200) nm
Thickness, cantilever	15 (30) nm
Spring constant	0.08 (0.02) kN/m
Reflective coating	Gold, 30nm

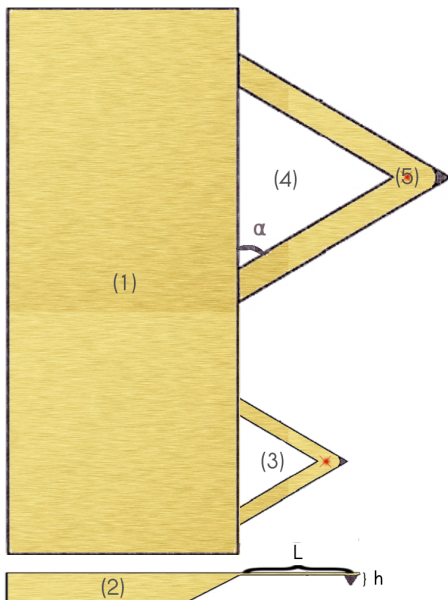


Fig. 3.13: A contact mode Si_3N_4 probe from a top side (1) and a rear view (2). There are two cantilevers on a contact mode probe; a small (3) and a large (4). The cantilever length is L , the tip height h and a side angle of $\alpha = 36 \pm 2^\circ$. The laser spot hits the cantilever at (5).



Fig. 3.14: A optical snapshot of the large and the small tip of a *Contact Mode* cantilever used in the lab. The geometric properties of the large and the small tip are described in Table 3.2. The dark spot at the end of each cantilever is the tip itself. The other dark spot on the cantilevers are most likely dust.

All six samples listed in Table 3.1 were studied by AFM. More than 100 AFM images were taken. In the following chapter, the image processing and data extraction are presented and discussed. The results from the AFM imaging are shown in chapter 5.

Chapter 4

Image processing and data extraction

This chapter is divided into four sections: image processing (Sec. 4.1), extracting raw data (Sec. 4.2), estimation QD volume (Sec. 4.3) and statistical tool (Sec. 4.4). This chapter starts with a two sections on raw data processing, especially explaining the impact of *Fast-Fourier transform* (FFT) and similar filters. The effect of a finite tip shape is also discussed. The third section describes eight different approaches to QD volume estimation, and outlines how they are implemented and utilized in this study. The final section contains some of the mathematical methods employed to analyse and present the data.

4.1 Image processing

This section covers the usage of *Gimp* and *Gwyddion* for processing and presentation of AFM images. Two different AFMs were used in this thesis work: one belonging to *Department of Physics (Biophysics lab., NTNU)*, the other owned by *SINTEF*. The *SINTEF* AFM was moved to Oslo in the middle of October 2011. The AFM on the *Biophysics lab.* had newer software, but otherwise the same characteristics as the *SINTEF* AFM - including identical type of AFM tip.

4.1.1 *Fast-Fourier Transform* (FFT) Filter

Most of the AFM images from the *Biophysics* AFM had systematic noise. $10\ \mu\text{m} \times 10\ \mu\text{m}$ AFM had little or weak, measurable noise. Most of the $500\ \text{nm} \times 500\ \text{nm}$ and $1\ \mu\text{m} \times 1\ \mu\text{m}$ images contained remarkable noise- therefore it was crucial to apply the FFT filter in order to extract the raw data. FFT filtering was, in most cases, not necessary for the AFM images from the *SINTEF* lab. Several procedures were explored to eliminate the noise - including turning off all nearby electronic equipment and lights. Similar noise were seen in *Tapping Mode* (TM) using a completely different cantilever type. It might be worth mentioning that the *Biophysics* AFM

had a repair and was calibrated around October 15th. The noise became weaker and changed to a higher frequency after the repair. The raw data did not change in any notable way, as the noise was subtracted regardless of what frequency it had. The source of the noise was not found, and it still remains unknown. The noise could be completely removed using a 2D *Fast-Fourier Transform* (FFT) Filter. 2D means that the frequency spectrum is two-dimensional i.e. has two spatial frequency components. In a typical AFM image, the frequencies components are defined in the image plane. Fig. 4.1 shows a $1\ \mu\text{m} \times 1\ \mu\text{m}$ AFM image before (a) and after (b) FFT filtering. The extracted image difference (a) and frequency spectrum (b) for the same AFM image can be seen in Fig. 4.2. The shape of the 2D frequency spectra show in Fig. 4.1 (b) was typically elliptic, and the major semi-axis was along x direction - snapped to the origin of the 2D frequency distribution. This indicates that the noise had higher frequency in y direction relative to x.

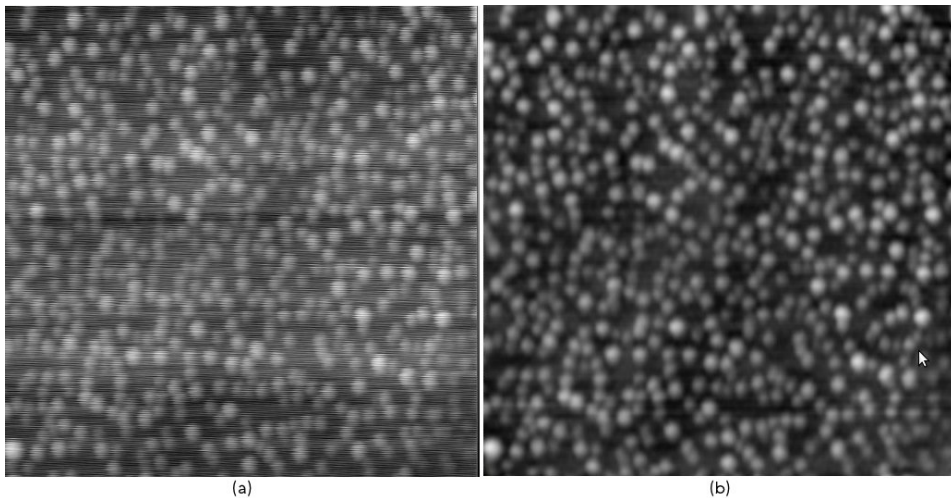


Fig. 4.1: An AFM Image before (a) and after (b) 2D *Fast-Fourier Transform* (FFT) filter

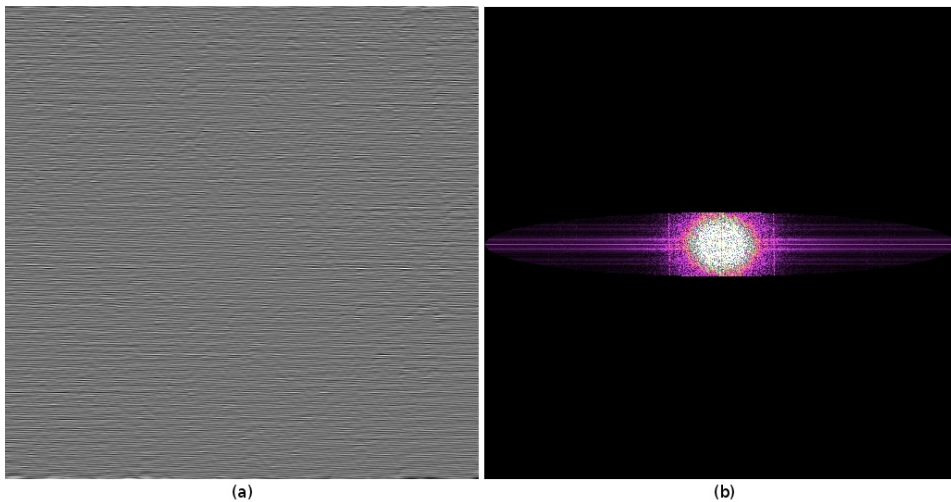


Fig. 4.2: Extracted image difference (a) and 2D frequency spectrum (b). The shape in (b) is elliptic with semi-major axis along x direction.

One crucial question is whether or not the FFT filtering influence or alter the raw data. FFT filtering was not necessary for the AFM images from the *SINTEF* lab, hence these images could be used as *references* in samples like *503-1* and *544-1* - which had AFM images from both the *SINTEF* and *Biophysics* AFM. The QD density, volume and diameter were estimated in the AFM images from the *Biophysics* lab before and after FFT filtering. The results were compared to similar data in the AFM images from the *SINTEF* AFM. The comparison was done using both $500\text{ nm} \times 500\text{ nm}$ and $1\text{ }\mu\text{m} \times 1\text{ }\mu\text{m}$ AFM images. The results demonstrated that the FFT filtered AFM image deviated much less from the results from the *SINTEF* lab, than the *Biophysics* AFM images without the FFT filter. The tendency seems to be that FFT filtering corrects the data. This can further be supported by investigating the z value in the raw *Biophysics* AFM images. *Gwyddion* recognizes the noise as actual height data. Thus, the noise results in a too high z value. It is important to point out that the FFT filter is far from being the only filter applied to the raw data before data extraction. The raw data files are processed in a series of filters, including tip convolution and several advanced techniques, described in Sec. 4.1. Most of the filters undoubtedly improve the precision of the data, and give more accurate results.

4.1.2 Estimated tip shape and size

The tip shape interacts with the surface topography in an AFM image, and the tip condition influences QD density, height and diameter. [36] The tip used in this study had the shape of a triangular pyramid, with sidewall angles of 36° . [35] A deformed tip shape or debris accumulated during scanning can cause various forms of distortions in the AFM images. There are two tip shape parameters affecting

the AFM image: the tip sidewall angles and the radius of curvature. The effect of tip shape is shown as an image profile in Fig. 4.3 below: a sharper tip can resolve smaller features than a dull tip. As a result, dull tips underestimate the QD density and height and overestimate the QD diameter. The impact of the tip shape on AFM images was explored thoroughly in [37].

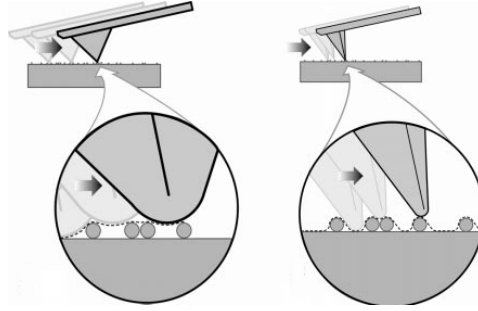


Fig. 4.3: Sphere-formed grains scanned with a dull tip (left) and a sharp tip (right). Reprinted from [38]

4.1.3 Deconvolution

The raw AFM image is not a picture of the real surface, but a convolution of the AFM tip and the surface. The effect of the tip deconvolution process on the AFM image is shown in Fig. 4.4. The surface was reconstructed by deconvoluting the surface, using an estimated tip shape. All data extracted in this study originated in deconvoluted AFM images. This section aims to find how the deconvolution affects the QD height data.

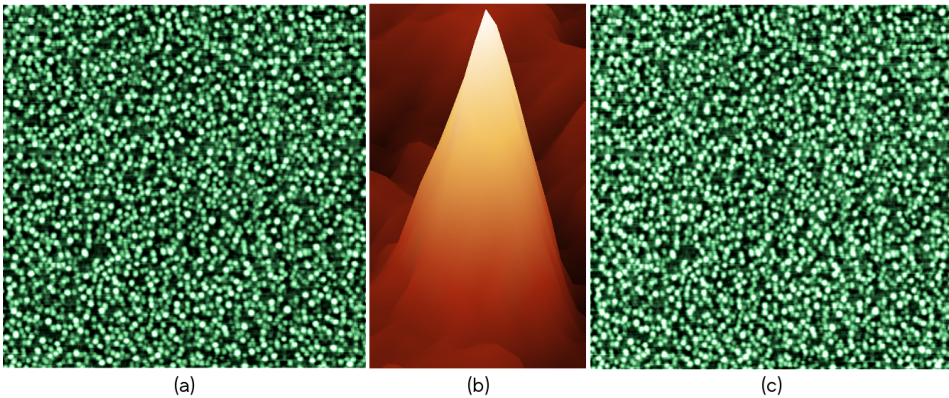


Fig. 4.4: Before and after deconvolution and background remove: the convoluted surface (a), estimated tip size and shape in 3D (b) and deconvoluted surface (c). The brightest point is 4.4 nm in (a) and 3.3 nm in (b).

The impact of deconvolution on QD height is shown in Fig. 4.5. The number of AFM images per sample was the same in both cases. As expected, the deconvolution process had an impact on the height data. Various samples were affected differently. The maximum QD height after deconvolution, was higher or the same for most of the samples. Sample *503-1*, *503-2* and *544-1* had no significant difference in height before and after deconvolution. The deviation was large and significant in sample *514-2*, as seen in Fig. 4.5. The QDs in sample *514-2* doubled their height after deconvolution. The deviation is also large for sample *504-1*. The data presented, suggest that maximum QD height remains the same or becomes higher in deconvoluted AFM images.

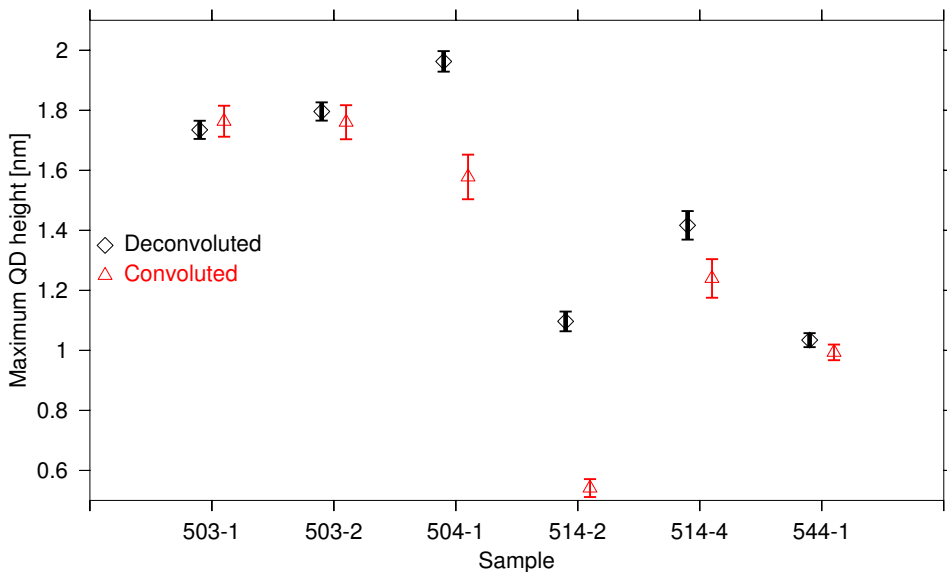


Fig. 4.5: The QD height before (**triangle**) and after (**diamond**) deconvolution. The estimates are from at least three (3) $500 \text{ nm} \times 500 \text{ nm}$ AFM images.

4.1.4 Processing AFM images

Gwyddion is probably one of the best free software available for SPM/AFM data processing. The data analysis and image processing in this thesis were mostly done using *Gwyddion*, including counting the QDs, finding the QD density and distributions of QD heights and diameters. The procedure below was used in *Gwyddion* to improve/correct the image, in the following order:

Procedure 1

- (1.1) 2D Fast-Fourier Filter (if systematic noise)
- (1.2) Correct lines by matching height median
- (1.3) Correct horizontal scars
- (1.4) Correction of median difference line
- (1.5) Remove scars
- (1.6) Mark grains (watershed/manual)
- (1.7) Remove polynomial background (3rd degree)
- (1.8) 2D Fast Fourier Transform (vertical noise)
- (1.9) Blind tip estimation
- (1.10) Deconvolution (surface reconstruction)
- (1.11) Finally, redo (1.2)-(1.7)

To deconvolute the image it is essential to use the procedure described in step (1.9) and (1.10) above. The shape and size of the estimated tip are important parameters in the deconvolution process. Finally, the raw data is extracted from the deconvoluted image.

Gimp was employed as a tool to improve the image quality and eyecandiness, most importantly to increase contrast locally to make the images more presentable and comprehensible. Filters used to improve the images includes, in chronological order, are found in the procedure below.

Procedure 2

- (2.1) Local contrast filter
- (2.2) Nonlinear swiss army knife
- (2.3) Despeckle
- (2.4) Deinterlace
- (2.5) Destripe
- (2.6) Antialias
- (2.7) Sharpen (safest) or unsharpen mask (most efficient)
- (2.8) Optimise contrast/brightness ratio

Image processing in *Gimp* was always done after a complete data analysis and image correction in *Gwyddion*. Images improved in *Gimp* were never used to do data analysis (count grains e.g.). The reason for this is potential "information loss" seen in some of the filters listed above. The real, observable information loss should be diminishable from the observers point of view.

Fig. 4.6 shows a raw $2\mu\text{m} \times 2\mu\text{m}$ AFM image first improved by **Procedure 1** in *Gwyddion*, then **Procedure 2** in *Gimp*.

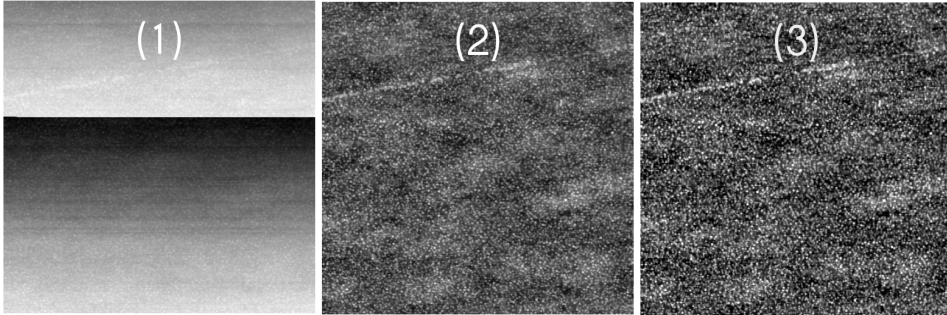


Fig. 4.6: A raw $2\mu\text{m} \times 2\mu\text{m}$ AFM image (1) corrected using *Gwyddion* (2) and finally optimized by *Gimp* (3).

The height scale is changed due to the removal of polynomial background and image deconvolution ((6), (7) and (8) in **Procedure 1**). High scan rates cause scan lines of systematic noise to appear to the right in the images. These lines of noise could be removed by a 2D FFT filter with elliptic shape with semi-major axis along the y axis.

The same processing procedure was used for all AFM images: **Procedure 1** followed by **Procedure 2**, as described in Sec. 4.1. Step (2) and (3) from **Procedure 2** (*Despeckle* and *Deinterlace*) were omitted for very high QD density $1\mu\text{m} \times 1\mu\text{m}$ AFM images. Since the smallest QDs in high-density AFM images often were recognized as noise, and the filters caused the QDs to blur and grow even more into each other. This can be seen in Fig. 4.7. The AFM images have to be magnified to see all QDs.

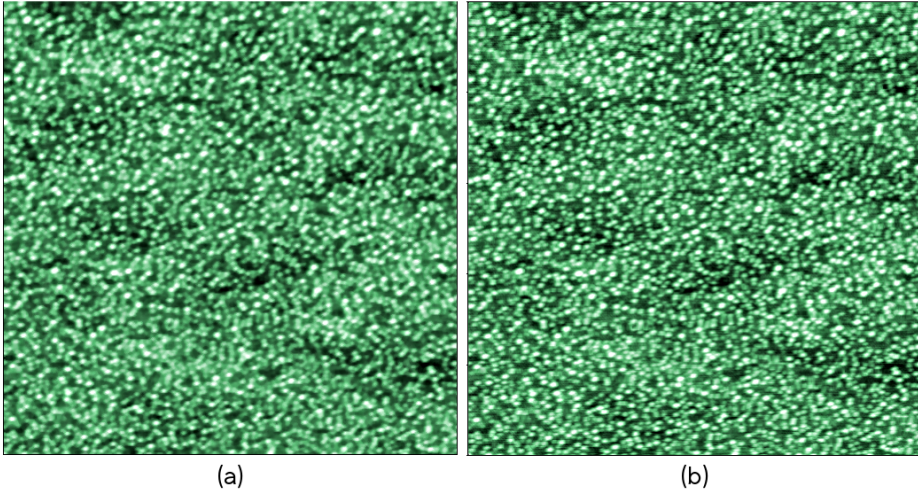


Fig. 4.7: A $1\ \mu\text{m} \times 1\ \mu\text{m}$ AFM image with very high QD density, improved in *Gimp* and following **Procedure 2** (a) full procedure (b) omitting *Desinterlace* (2.4) and *Destripe* (2.5).

4.2 Extracting raw data

Numerical data were only extracted from $500\ \text{nm} \times 500\ \text{nm}$ and $1\ \mu\text{m} \times 1\ \mu\text{m}$ AFM images. The images were in most cases magnified by a factor of 2, from $512\text{px} \times 512\text{px}$ to $1024\text{px} \times 1024\text{px}$, prior the masking process (step (1.6) in procedure 1). This was done using zooming function on the PC monitor, not by up-scaling or altering the AFM image itself.

To obtain quantitative data from the AFM images, the boundary of each QD had to be identified. There were two primary algorithms to mark QDs/grains in *Gwyddion*: *threshold* or *watershed*. The terminology "grains" / particles refers to observable QDs in an AFM image. Thresholding procedures can be a very simple and efficient way to mark grains. In the threshold algorithm, the grains are masked by setting an upper and a lower limit to height, slope and/or curvature of the grains. The grain mask can be constrained by one or all three parameters. For instance, threshold algorithm can mask all grains with a height between 1 nm and 2 nm. Systematic noise or sample contamination can be eliminated by limiting the QD size and/or height (maximum or minimum). The threshold algorithm can be used for distinguishing larger grains, from smaller ones. For images of insufficient quality or extremely high QD density, the accuracy of the thresholding algorithms can be very poor. This is illustrated in Fig. 4.9 (a), where a single mask covers a cluster of several QDs. Clusters of QDs were often identified as a single grain (see (b) in Fig. 4.8), a problem even greater in high QD density samples. The grains had to be corrected manually, and made the *threshold* algorithm both time-consuming and unreliable for high-density samples.

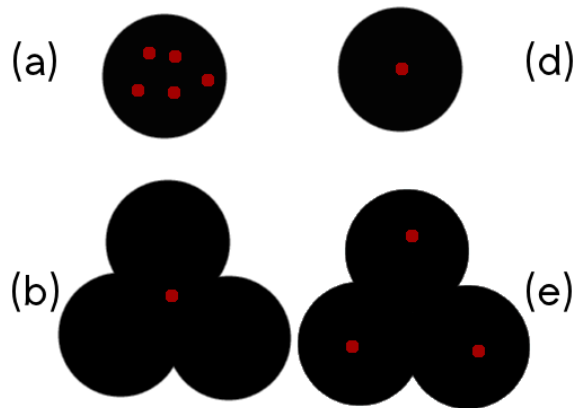


Fig. 4.8: Two common problems in the *watershed* algorithms: (a) a single grain is recognized as multiple grains (overestimation), (b) a cluster of grains is identified as one single grain (underestimation), (c) and (d) grain mask corrected manually.

The *watershed* algorithm is generally more trustworthy when it comes to counting QDs in images with high QD densities. In high-density images less manual correction is required compared to the *threshold* algorithm described above, because the problem of identifying a cluster of grains as one single grain occurred less frequently (see (b) in Fig. 4.8). *Watershed* did however often recognize one single grain as multiple grains (see (a) in Fig. 4.8), but this was partly solved by growing the mask a few pixels - so the multiple grains within a single grain overlapped to form one mask.

The *watershed* algorithm usually calculates the local minima by simulating *flooding*. The fundamental principle is that a drop of water eventually would fall into a local minima in a topography. The simulation of *flooding* roughly follows the principles outlined below. The AFM image is first partitioned into smaller segments (*superpixels* - a set of pixels), sorting each pixel in every superpixel after grey-level. The grey-level in the AFM images represents height data. The center of *flooding* starts in the brightest pixel in every image segment (*superpixels*). First the flooding expands to all closest-neighbour pixels and sorts them after grey-level (area 1). The darkest pixel in area 1 is the next centre of flooding. The flooding expands to all closest-neighbour pixels, categorizing after grey-level (area 2). In the next iteration, the second darkest pixel is flooded in area 1 and the darkest pixel is flooded in area 2; making new flooding areas and sorting all closest-neighbour pixels after grey-level. If the closest-neighbours of a centre of flooding has been *flooded* and they all have the same grey-level, the flooding centre will have the same grey-level as the closest pixels.

The method above locates a rim ("local minima") around each grain in the image, confining the outer boundaries of the grain. To count the total number of grains one simply counts the number of confined regions. One major drawback of the *watershed* method is that it sometimes recognizes a single QD not as one - but several

local maxima, counting the same QD several times. The area of each grain was in some cases expanded in an attempt to correct the problem. The second problem was that the algorithm recognized contamination or abnormalities as grains. The two issues above result in an over-counting, and could to some extent be avoided by choosing proper algorithm parameters. Although the marking algorithms in *Gwyddion* could easily identify and mark some of the grains, it was not a reliable counting method by itself in images with a high QD density. As a result, most of the maskings had to be cross-checked manually - sometimes adding, subtracting, merging or splitting grain masks.

The third problem was boundary QDs: QDs with a fraction of its visible area partly outside the captured image area. See Fig. 4.9 (b). A manual procedure to solve the issue was invoked as follows

- ◇ less than a $\frac{1}{2}$ QD is visible \Rightarrow : not counted
- ◇ more than a $\frac{1}{2}$ QD is visible \Rightarrow : counted as one QD

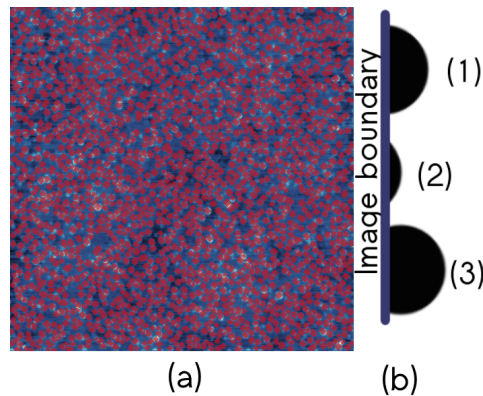


Fig. 4.9: (a) An attempt to count high-density grains (masked in red) in a $1 \mu\text{m} \times 1 \mu\text{m}$ AFM image (to the left). (b) Boundary grains (1) Counted as one grain: more than half of the total grain area is visible, compared to a full-sized grain. (2) Not counted. (3) Counted.

4.3 Estimating QD volume

The raw data to use for QD volume estimation consists of processed AFM image, where each QD is covered by a mask. The masks of individual QDs do not overlap, and the pixels within the mask contain height data for a single QD. Based on the base area and height data of the mask, the QD volume can be found.

This study aims to explore the potential of the AFM instrument, and the use of AFM images to estimate total QD volume. There are several possible approaches to estimate QD volume from an AFM image. The QDs can be approximated to geometrical figures, like cones or hemi-spheres. However, the exact shape of the QDs is not known and will probably vary from sample to sample - briefly discussed in Sec. 3.1.1. Totally eight volume estimation methods were developed and evaluated in this work, to find the best method to estimate QD volume from AFM images. The eight volume methods can be divided into three branches:

- ◇ *Surface area method* ($V_{h,0}$ and V_h): estimates the topography of the real 3D surface, and thus the height from the basis plane of the QD to the approximated surface is known for any given pixel. The total volume of the QD can then be found by summing over all volume elements with a base area of one pixel, and a varying height defined by the approximated surface. This is an approximation to a volume integration. The exact details of the surface approximation are described in section 4.3.1.
- ◇ *Pyramid/cone method* ($V_{h-max,0}$, $V_{h,max}$, V_{fusion} , V_L): finds the maximum z value within the QD, \bar{H} (maximum QD height), and calculates the volume assuming that the QD has the shape of a perfect cone or a pyramid. The projected area is the base area of the cone/pyramid. This method is a very common approximation, used in several studies in literature.
- ◇ *Mean value method* ($V_{h-mean,0}$, V_{h-mean}): estimates the mean value of all z values within the QD, \bar{h} (mean QD height). The QD volume is found by multiplying the mean height with projected QD area, $V = A_{proj} \cdot \bar{h}$. The projected QD area can easily be estimated if the boundaries of the QD is known. This is typically found by iterative algorithms.

Table 4.1 shows the formulas of the three branches of volume estimation methods. V_{fusion} is implemented the same way as the *pyramid/cone method*, but combines QD density and height from AFM data and effective QD diameter from SEM, to minimize the error. The effective QD diameter is converted to projected QD area, thus the volume formula for V_{fusion} can be expressed as:

$$\begin{aligned}
 V_{fusion} &= \frac{\bar{A}_{proj}^{(SEM)} \cdot \bar{h}_{max}^{(AFM)} \cdot \bar{N}_{QD}^{(AFM)}}{3} \\
 &= \frac{\pi (\bar{D}_{eff}^{(SEM)})^2 \cdot \bar{h}_{max}^{(AFM)} \cdot \bar{N}_{QD}^{(AFM)}}{12}
 \end{aligned}$$

where $\bar{D}_{eff}^{(SEM)}$ is the effective diameter from SEM data, \bar{H} the mean maximum QD height from AFM data and $\bar{N}_{QD}^{(AFM)}$ the mean number of QDs from all AFM images in a given sample.

Table 4.1: The eight volume estimation methods sorted in three branches with corresponding volume formula.

Volume methods	Principle	Formula
$V_{h,0}$ and V_h	Surface area	$\sum_{i=1}^n h_i \cdot A_{px}$
$V_{h-max,0}$, $V_{h,max}$, V_{fusion} , V_L	Pyramid/cone	$V = \frac{A \cdot \bar{H}}{3}$
$V_{h-mean,0}$ and V_{h-mean}	Mean value	$V = A_{proj} \cdot \bar{h}$

All the three branches above estimate the volume from z values within the boundaries of the QD mask. The QD volume can be estimated relative to different types of zero planes (reference z values). In this work, three types of zero basis planes were implemented:

- ◇ *Global zero plane* ($V_{h-mean,0}$, $V_{h-max,0}$, $V_{h,0}$): estimates QD volume relative to a global plane (at $z = 0$), set by *fix zero* - an extrapolated reference z value. The volume below $z = 0$ counts as negative volume.
- ◇ *Local zero plane* (V_{h-mean} , V_{h-max} and V_h): subtract a local plane defined as $z_{ref} = z_{min}$ for each QD. z_{min} is the minimal z value within the boundaries of the mask.
- ◇ *Laplacian plane*: V_L uses a Laplacian interpolation to find an individual basis plane from the surrounding z values, and calculates the volume between the basis plane and the surface. This is the most sophisticated method, but it is challenging to get an exact intuition on how accurate it works - since the size of the interpolation area is unknown.

4.3.1 Approximating the real QD surface

This section discusses a method for estimating the real 3D surface area of a QD, utilized by *surface area methods* described in the previous section. Uncertainties and errors in the surface approximation method would therefore also apply to the *surface area methods* (V_h and $V_{h,0}$).

Let z_j for j be the z value in four neighbour pixels positioned in the centre of the pixel, as illustrated in Fig. 4.10. A square is constructed with corners in the centre of each pixel. Each square is divided into four triangles. The surface area of one triangle, for example A_{23} , is given by

$$A_{23} = \frac{h_x h_y}{4} \sqrt{1 + \left(\frac{z_2 - z_3}{h_x}\right)^2 + \left(\frac{z_2 + z_3 - 2\bar{z}}{h_y}\right)^2} \quad (4.1)$$

The total surface area of a square can be found by adding the area of the four triangles that are formed inside each square :

$$A = A_{12} + A_{23} + A_{34} + A_{41} \quad (4.2)$$

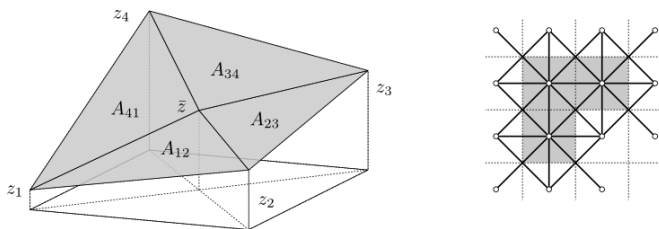


Fig. 4.10: Left: how the topography of the QD is determined using a triangle approximation. Right: summing all pixels and the corresponding half-triangles give the total surface area.

Suppose we divide the four triangles further in half into eight smaller triangles. Each pixel would then be composed of eight half-triangles, as illustrated in Fig. 4.10. The total area in the pixel is found by summing the areas in each half-triangle (mask in grey, Fig. 4.10), and the surface area in a grain is estimated by summing the surface area over all pixels in a grain. This is nevertheless an approximation. The half-triangles are flat and do not follow the curvature of the real surface. The grain boundary defines which pixels are inside or outside the QD.

4.3.2 Deposited QD volume converted to equivalent Mono Layers

The main motivation to convert the deposited QD volume to equivalent Mono Layers (ML), is to be able to compare the estimated volumes with deposited volumes, to see if Ga might be incorporated from the substrate or not. The equivalent ML has the advantage that it is independent of the size of the scan area. Hence, both $500 \text{ nm} \times 500 \text{ nm}$ and $1 \mu\text{m} \times 1 \mu\text{m}$ AFM images could be directly compared in terms of equivalent Mono Layers (ML).

For the *Zinc-Blende Structure* of InAs, the elastic stiffness tensor C can be expressed as [39]

$$C = \begin{bmatrix} C_{11} & C_{12} & C_{12} & 0 & 0 & 0 \\ C_{12} & C_{11} & C_{12} & 0 & 0 & 0 \\ C_{12} & C_{12} & C_{11} & 0 & 0 & 0 \\ 0 & 0 & 0 & C_{44} & 0 & 0 \\ 0 & 0 & 0 & 0 & C_{44} & 0 \\ 0 & 0 & 0 & 0 & 0 & C_{44} \end{bmatrix}$$

The relationship between the elastic compliance tensor and the elastic stiffness tensor, S , is found by Hooke's relation [39]

$$S_{11} = \frac{C_{11} + C_{12}}{(C_{11} - C_{12})(C_{11} - 2 \cdot C_{12})}$$

$$S_{12} = \frac{-C_{12}}{(C_{11} - C_{12})(C_{11} - 2 \cdot C_{12})}$$

Let us define z along the growth direction, $[0 \ 0 \ 1]$. Then the strain tensors ϵ_{ij} , are given by [40]

$$\epsilon_{xx} = \frac{a_{\parallel}}{a_0} - 1$$

$$\epsilon_{zz} = \frac{2 S_{12}}{S_{11} + S_{12}} \cdot \left(\frac{a_{\parallel}}{a_0} - 1 \right)$$

$$\epsilon_{xy} = \epsilon_{yz} = \epsilon_{zx} = 0$$

where $a_{\parallel, InAs} = a_{GaAs}^{bulk}$ is the strained lattice constant, and $a_0 = a_{InAs}^{bulk}$ the bulk lattice constant. Furthermore, it is possible to define ϵ_{zz} by the normal strained lattice constant $a_{\perp, InAs} = a_{InAs}^{strained}$

$$\epsilon_{zz} = \frac{a_{\perp}}{a_0} - 1$$

$a_{\perp, InAs}$ is found by substituting for ϵ_{zz} in the equation above, and multiplying both equations with a_0

$$a_{\perp} = a_0 + \frac{2S_{12}}{S_{11} + S_{12}} \cdot (a_{\parallel} - a_0) \quad (4.3)$$

Let V_{dep} be the volume of QDs in a total area A . Assume that the volume is distributed with 100% uniformity. The corresponding height of the volume is

$$h = \frac{V}{A}$$

and converted to monolayers, we get

$$h_{ML} = \frac{h}{\frac{a_{\perp}}{2}}$$

where a_{\perp} is the out of place, strained lattice constant. For the InAs / GaAs system at 300K, $a_{\perp} \approx 6.50\text{\AA}$, which is larger than the corresponding lattice constant for In (6.06\AA) and Ga (5.65\AA).

4.4 Statistical tools

This section is included for the reader to understand the data analysis process. The statistical tools were essential in the data analysis, and were mostly performed using spreadsheets (*Gnumeric*), and in some cases general-purpose statistical software like *Stata* and *Octave*. Most of the graphs were drawn using *Gri* programming language (vector graphics).

4.4.1 Calculating the Quantum Dot(QD) density

All QD densities were estimated from $500\text{ nm} \times 500\text{ nm}$ and $1\text{ }\mu\text{m} \times 1\text{ }\mu\text{m}$ AFM images only. A high quality image was needed to mask QDs in $1\text{ }\mu\text{m} \times 1\text{ }\mu\text{m}$ AFM images accurately, especially in high-density samples like *544-1*. Low-quality images could not be used. $2\text{ }\mu\text{m} \times 2\text{ }\mu\text{m}$ AFM images were not chosen because the counting uncertainty was too high, since many of the QDs merged together at this scale and were impossible to separate. The population size of QDs is on average four times larger for $1\text{ }\mu\text{m} \times 1\text{ }\mu\text{m}$ compared to $500\text{ nm} \times 500\text{ nm}$ AFM images. Fewer high-quality AFM images are needed in order to get a representative data set.

The scans were performed in at least three locations per sample, separated by a few millimetres. The X/Y offset for piezo-scanner was typically set to zero. Two samples, *503-1* and *503-2*, had a few images with X/Y offsets, and thus a little drift can be seen in some of the images. All scans were conducted using different scan angles, scan rates, deflection point and feedback loop parameters. The main motivation to choose at least three different locations for each sample, was to probe the sample homogeneity. Counting QDs in the same AFM image repetitively gives the counting uncertainty. The counting uncertainty in a sample piece says very little about the sample variance in local QD density. Since the scanning regions only

were separated by a few millimetres, it was expected that the the characteristics of each image only differed slightly. The sample pieces were all expected to have a quite homogeneous distribution of QDs, since they were from the centre region of the quarter wafer. The mean QD density refers to the mean counted value based on three or more images in a single location, each image counted one or several times.

Based on the number of QDs, the QD density in AFM images is found by the following equation:

$$\rho_{QD} = \frac{\# \text{counted QDs}}{\text{area in } cm^2} \quad (4.4)$$

4.4.2 Sample mean and sample variance

The homogeneity in QD size, height, volume and density for several samples have been studied. The sample variance is an important tool to determine the distribution of QD size and density across the sample.

Let U_1, \dots, U_n be independent measurements from a normally distributed population of N QDs. Suppose the population has a mean of μ and a variance σ^2 . Then $\bar{U} - \mu$ is Student's t-distributed with $N - 1$ degrees of freedom, which is normally distributed for a large population N . The sample mean (\bar{U}) and the sample standard deviation (s_U) could easily be estimated by

$$\bar{U} = \frac{1}{N} \cdot \sum_{i=1}^N U_i \quad (4.5)$$

and

$$s_U = \sqrt{\frac{1}{N-1} \sum_{i=1}^N (U_i - \bar{U})^2} \quad (4.6)$$

where s_U is an unbiased estimator.

4.4.3 Pearson's product-moment coefficient

The motivation for calculate *Pearson's product-moment* coefficients is to find how parameters correlate to each other, such as how island size correlates to QD density. *Pearson's product-moment* coefficients indicate whether hypotheses based patterns in observation could be correct, and may well reveal more hidden patterns and correlations in the data set.

Pearson's product-moment coefficients can be defined as follows. Let U and V be two stochastic variables with standard deviations ρ_U and ρ_V and expected values μ_U and μ_V . Then the correlation between the two variables is defined as

$$\rho_{U,V} = \text{corr}(U, V) = \frac{\text{cov}(U, V)}{\sigma_U \sigma_V} = \frac{E[(U - \mu_U)(V - \mu_V)]}{\sigma_U \sigma_V}, \quad (4.7)$$

where cov is the covariance, E the expected value(operator) and $\rho_{U,V}$ is the *Pearson product-momentum correlation* coefficient. Interpretation

- ◇ $\rho_{U,V} = 0 \Rightarrow U$ and V is independent
- ◇ $|\rho_{U,V}| < 1 \Rightarrow U$ and V weakly or strongly correlated/anti-correlated
- ◇ $\rho_{U,V} = \pm 1 \Rightarrow U$ and V linear correlated/anti-correlated

The closer the coefficient is to ± 1 , the stronger the correlation must be between U and V .

4.4.4 Error in the approximation of effective diameter

Consider a circle with diameter D , and an ellipse where the semi-major axis a is twice the length of the semi-minor axis b . The area of the ellipse is $A_{ellipse} = \pi a b = \frac{1}{2}\pi a^2$ and the area of the circle is $\frac{1}{4}\pi D^2$. The circumference of the circle is $C_{circle} = \pi D$, for the ellipse a good approximation is

$$C_{ellipse} \approx \pi (a + b) \left(1 + \frac{3 \left(\frac{a-b}{a+b} \right)^2}{10 + \sqrt{4 - 3 \left(\frac{a-b}{a+b} \right)^2}} \right).$$

Since the semi-major axis $a = 2b$, the expression reduces to

$$C_{ellipse} \approx \frac{\pi a(9 - \sqrt{35})}{2} \approx 1.54196a \pi$$

The effective diameter is found by requiring

$$C_{circle} = C_{ellipse} \implies \pi D_{eff} = 1.54196a \pi \implies D_{eff} = 1.54196a$$

The area of the circle with the effective diameter

$$A_{circle} = \frac{1}{4}\pi D_{eff}^2 \approx \frac{1}{4}\pi(1.54196a)^2 \approx 0.59441016\pi a^2$$

Assuming that $A_{ellipse}$ is a closer estimate to the true projected area, the error by approximating the ellipse to a circle is

$$\frac{A_{circle} - A_{ellipse}}{A_{ellipse}} = \frac{(0.59441 - 0.5)\pi a^2}{0.5\pi a^2} \approx 0.189$$

This implies that, under the assumptions

- ◇ all QDs have an elliptic shape
- ◇ the semi-major and semi-minor axes, a and b , is s.t. $a < 2b$

the error in projected areas, estimated from effective diameter is less than 20%. This is a very conservative estimate, as most of the QDs investigated in this study had an approximate circular shape $a \approx b$.

Chapter 5

Results and discussion

In this chapter the AFM images and the data extracted are presented and discussed. The nominal growth parameters for all six samples are found in Table 3.1. Typical AFM images from all samples are shown in Sec. 5.1, and numerical data extracted from the images are found in sections 5.2 to 5.5. Contour background maps for the *wetting layers* are shown in Sec. 5.6, for all samples. Defects are presented in Sec. 5.7, using $10\ \mu\text{m} \times 10\ \mu\text{m}$ AFM images. Large QDs and their characteristics are also investigated. The chapter finishes with a section on errors and uncertainties. All error bars presented are 95% confidence intervals.

5.1 AFM images

A handful of the best AFM images are presented below. The scanning parameters were optimized manually to the local topography of each scanning area. Feedback loop settings (proportional gain, integral gain and deflection point) and force calibration constants were also optimized. Sample *504-1* and *514-4* were captured using *biophysics* AFM only, whereas *514-2* were taken by the *SINTEF* AFM, and *503-1*, *503-2* and *544-1* captured by a combination of both. The AFM images of sample *514-2* and *514-4* were taken over a short period of time, a few days at the most. Many of the images in sample *514-2* and *514-4* was even taken with the same AFM tip, the same day. On the contrary, *503-1* and *544-1* were captured over a few months, mostly with different tips. It was particularly hard to take good images of sample *503-1* and *544-1*, the conditions had to be very optimal in order to get a satisfying quality image quality.

All AFM images shown in this section have the same height scale, going as a linear gradient from 0 nm (black) to 5 nm (white). Keep in mind that the human eye sees brightness logarithmic. It was essential that all AFM images were processed using the exact same procedures. These procedures are described in Sec. 4.1. Thus, all images should be comparable and can be interpreted by the same premises. Some information loss in the AFM images is expected due to down-scaling and the finite printer resolution.

5.1.1 Sample 503-1

Four AFM images from sample 503-1 are shown in Fig. 5.1. The images are from three distinct locations, several millimetres apart. Image (a) and (d) are approximately from the same location, only displaced by a few μm due to re-engaged tip. The AFM images have scan sizes of $2\ \mu\text{m} \times 2\ \mu\text{m}$ (a) and $1\ \mu\text{m} \times 1\ \mu\text{m}$ (b), (c) and (d) respectively. Image (b) is acquired at the *Biophysics* lab, and image (a), (c) and (d) are from *SINTEF* lab. General differences between *SINTEF* and *Biophysics* AFM images were discussed in chapter 4.

The size and shape of the QDs are nearly identical in (c) and (d), but a little different in (b). The same AFM tip was used in (c) and (d). The QDs are stretched diagonally in the AFM image to the (b). This might be caused by a small amount of drifting. Drifting is known to increase QD size in one particular direction. Thus, the measured QD volume becomes an overestimate. Drifting can be minimized by proper calibration and limiting the use of X/Y offset. X/Y offset was only applied in some images from sample 503-1 and 503-2.

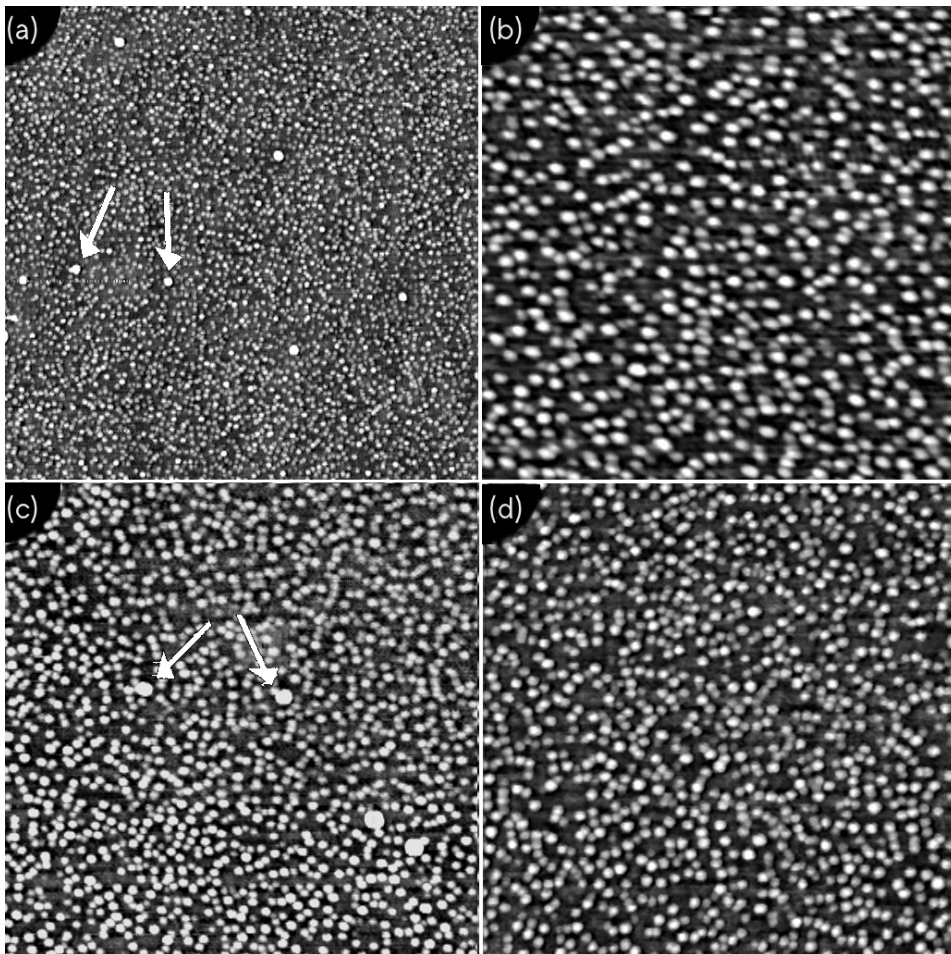


Fig. 5.1: $2\ \mu\text{m} \times 2\ \mu\text{m}$ (a) and $1\ \mu\text{m} \times 1\ \mu\text{m}$ AFM images (b), (c) and (d) of sample 503-1, in three different locations. Image (a) and (d) are from the same location.

Eight large QDs can be observed in Fig. 5.1 (a), whereas two large QDs are indicated by white arrows. Image (c) has four observable large QDs. This illustrates the great variation in large QD density from location to location: a single $1\ \mu\text{m} \times 1\ \mu\text{m}$ AFM image is thus not representative for the distribution of large QDs. A higher scan size or several $1\ \mu\text{m} \times 1\ \mu\text{m}$ images have to be used in order to get an accurate measure of the distribution of large QDs in a given sample. (b) had larger projected QD area, largest volume per QD and had lowest QD density compared to (c) and (d). Image (c) had both highest QD density and largest estimated QD volume. The estimated total QD volume deviated very little between (b) and (d).

5.1.2 Sample 503-2

Typical AFM images of sample 503-2 are shown in Fig. 5.2. All AFM images from sample 503-2 were acquired using the *Biophysics* AFM. Image (a) and (d) are from the same location on the sample piece. The projected QD area, mean height and volume per grain were not significantly different between the images (b), (c) and (d). The QD density was slightly higher in (c) relative to image (b), and lower in (d). Large QDs can be seen in all images in Fig. 5.2. Generally, the QDs is less defined, larger and more elliptic in (d) - an effect best explained by drifting.

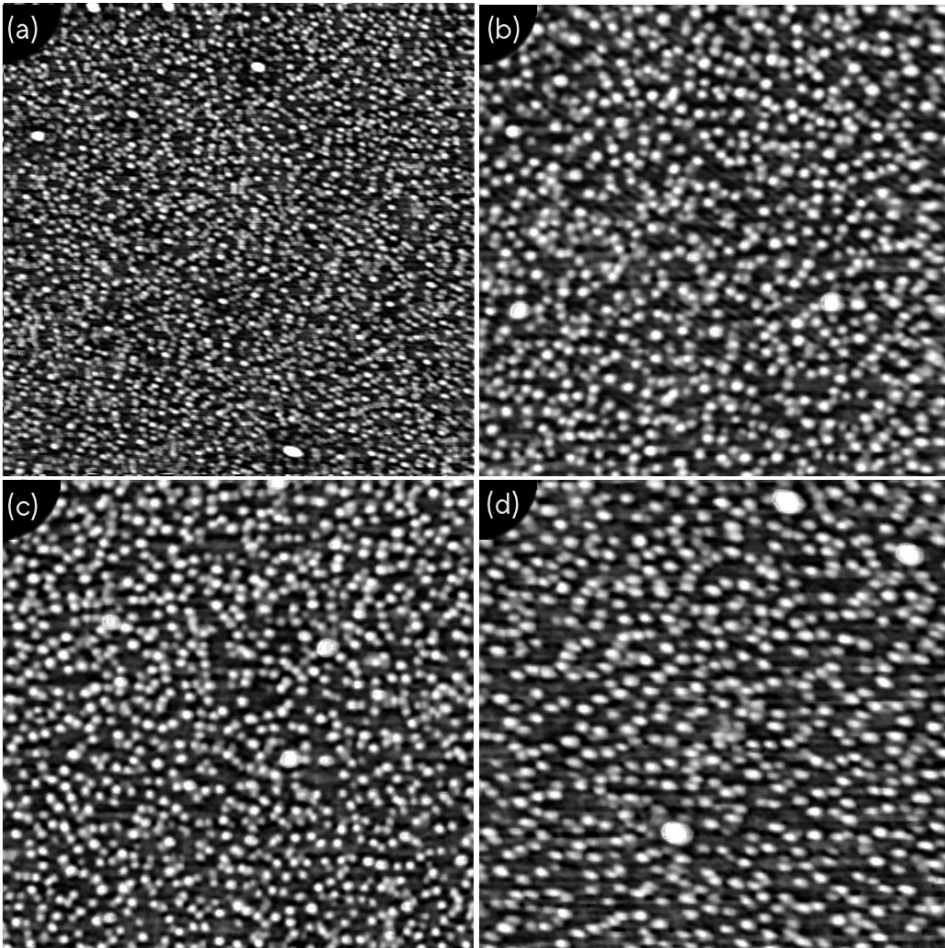


Fig. 5.2: $2\ \mu\text{m} \times 2\ \mu\text{m}$ (a) and $1\ \mu\text{m} \times 1\ \mu\text{m}$ AFM images (b), (c) and (d) of sample 503-2, in three different locations. Image (a) and (d) are from the same location.

Image (b) has a weak pattern in the background. The pattern is found everywhere in Fig. 5.2 (b), but can only be seen with magnification. Fig. 5.3 is a small, magnified section of image (b) in Fig. 5.2. The pattern can be seen as diagonal lines in the background of Fig. 5.3. The diagonal pattern was not caused by image processing, as the same structure was visible in the raw image.

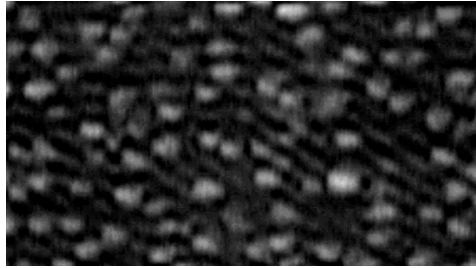


Fig. 5.3: Fig. 5.2 (b) magnified. Diagonal lines can be seen in the background.

5.1.3 Sample 504-1

AFM images of sample 504-1 are presented in Fig. 5.19. Only the *Biophysics* AFM were employed to collect data of sample 504-1. The two very bright QDs in (d) are large QDs. Assuming for now that image (a) is representative for the entire sample, it seems like there are a lower density of large QDs than observed in sample 503-1 and 503-2. The QDs in 504-1 appear larger when compared to high-density QD like 503-1, viewing from AFM images. The shape and size of the QDs are different in image (b) and (c), indicating a dull tip in image (c). Sample 503-2 and 504-1 had the highest measured mean QD height of all samples, but lower QD density than 503-1.

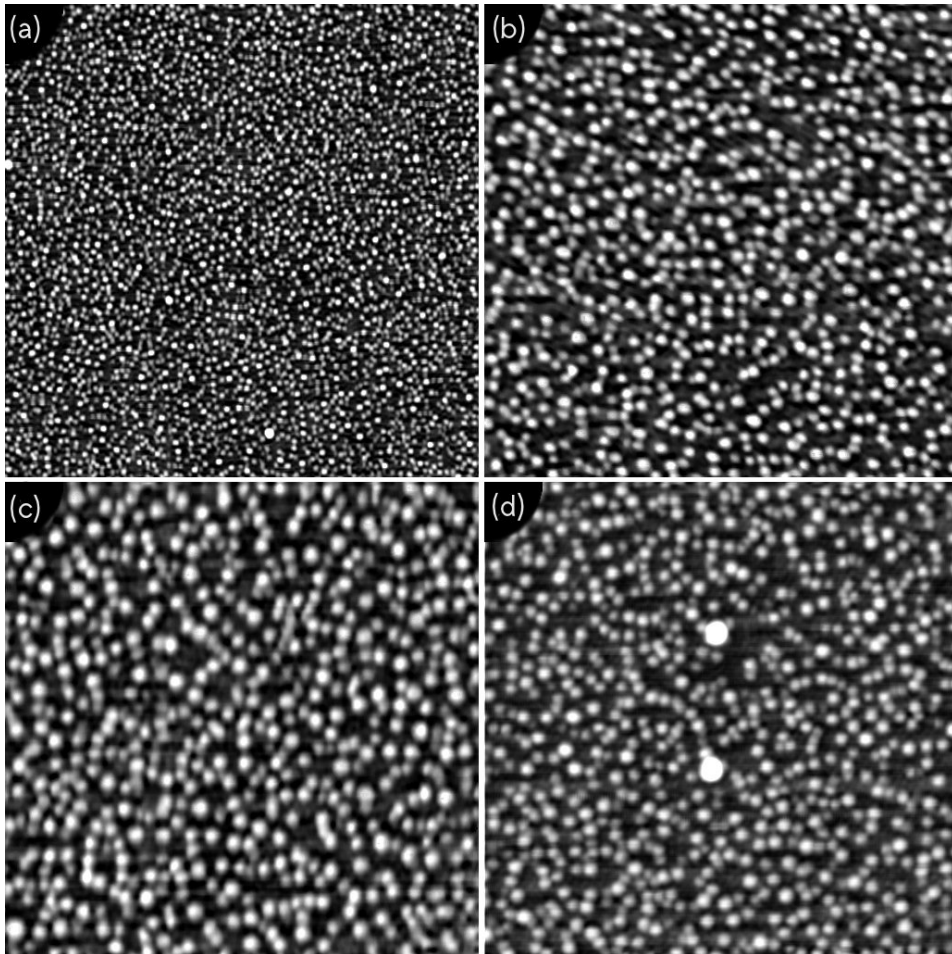


Fig. 5.4: $2\ \mu\text{m} \times 2\ \mu\text{m}$ (a) and $1\ \mu\text{m} \times 1\ \mu\text{m}$ AFM images (b), (c) and (d) of sample *504-1*, in three different locations. Image (a) and (d) are from the same location.

5.1.4 Sample *514-2*

Four different AFM images from three locations are shown in Fig. 5.5. These AFM images were acquired using the *SINTEF* AFM only. Image (a) is from the same location as (d). The QD density in sample *514-2* is lower and the diameter larger than in samples like *503-1* (Fig. 5.1). Some local variations in QD density can be observed, as the QDs seem to cluster and leave open spaces between them. There are few observed large QDs in sample *514-2*. The shape and size of the QDs seem to be the same in all $1\ \mu\text{m} \times 1\ \mu\text{m}$ AFM images, perhaps a little larger in image (b). No significant difference in projected QD area was found between the images. On the other hand, variations in height was found. The QDs in image (b) were higher mean height, relative to image (c). The QD height was about the same in (c) and

(d).

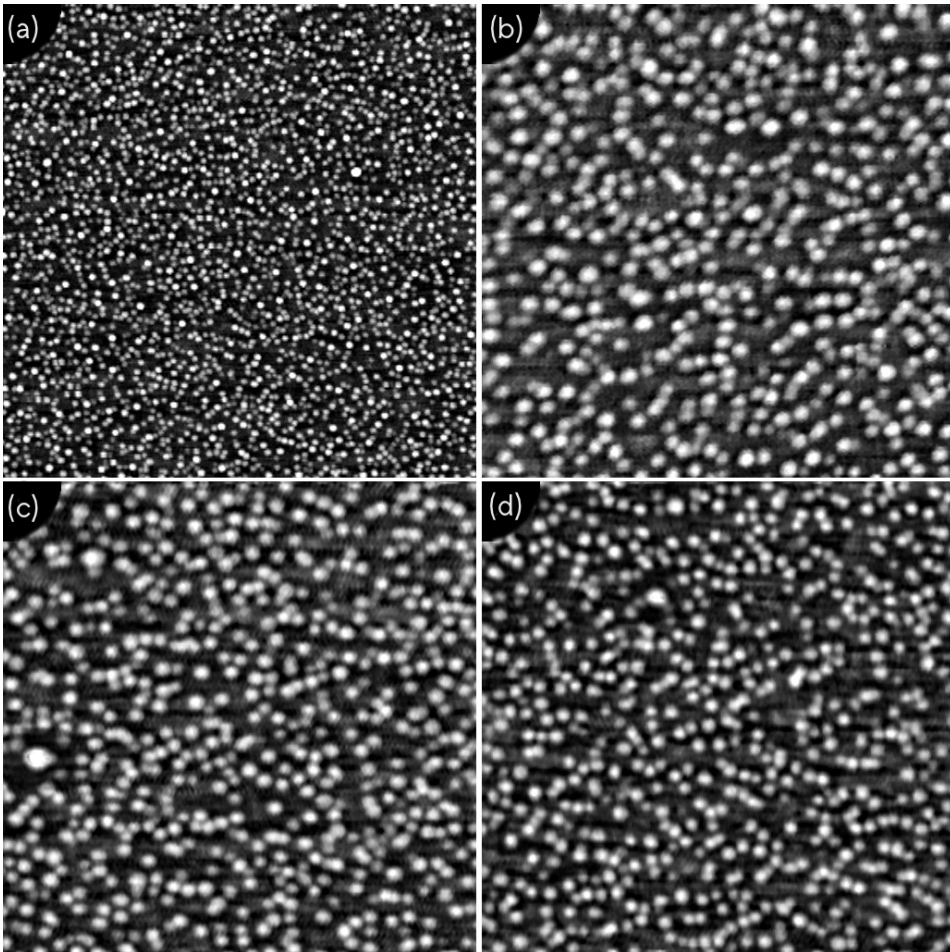


Fig. 5.5: $2\ \mu\text{m} \times 2\ \mu\text{m}$ (a) and $1\ \mu\text{m} \times 1\ \mu\text{m}$ AFM images (b), (c) and (d) of sample *514-2*, in three different locations. Image (a) and (d) are from the same location.

5.1.5 Sample *514-4*

One $2\ \mu\text{m} \times 2\ \mu\text{m}$ (a) and three $1\ \mu\text{m} \times 1\ \mu\text{m}$ (b), (c) and (d) AFM images are presented in Fig. 5.6. The images were all captured by the *Biophysics* AFM. It is apparent from the AFM images in Fig. 5.6 that sample *514-4* has lower QD density than most of the other samples presented in this work. Generally, no or very few large QDs were observed in sample *514-4*. The QD height is not significantly different in image (b), (c) or (d). The background is more visible than in other samples due to the low QD density.

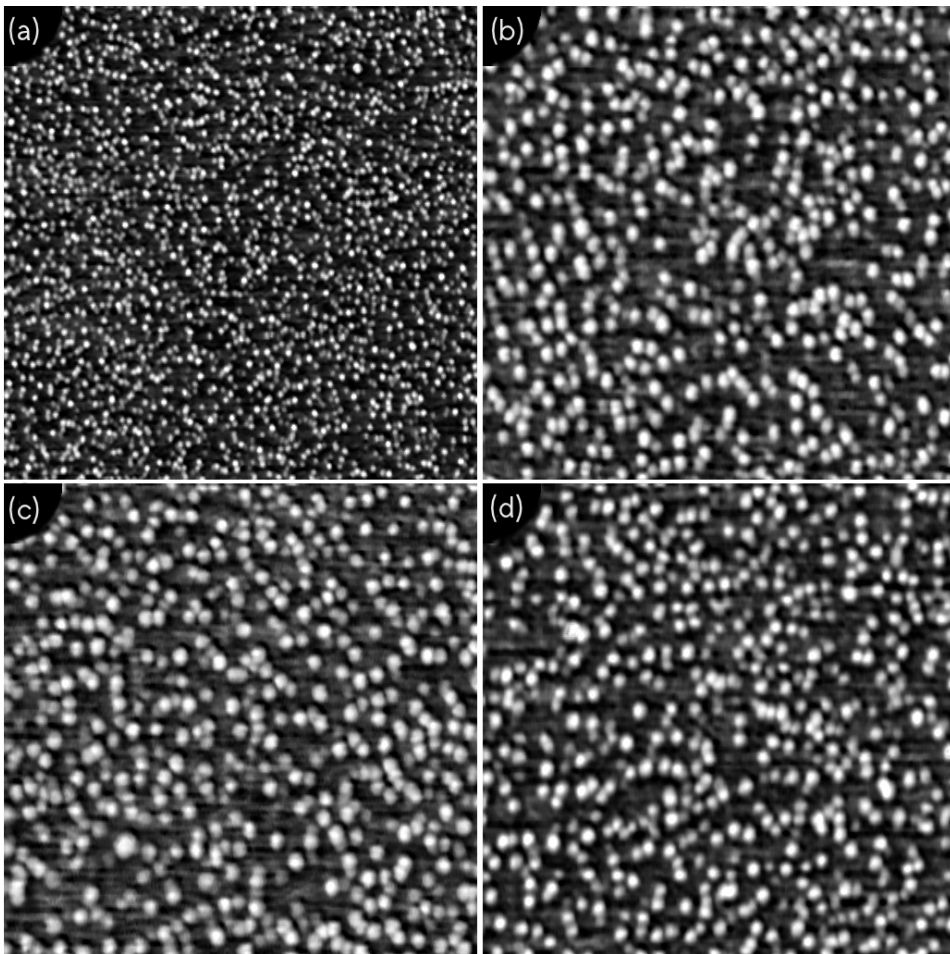


Fig. 5.6: $2\ \mu\text{m} \times 2\ \mu\text{m}$ (a) and $1\ \mu\text{m} \times 1\ \mu\text{m}$ AFM images (b), (c) and (d) of sample *514-4*, in three different locations. Image (a) and (d) is from the same location.

5.1.6 Sample *544-1*

Four AFM images of sample *544-1* are presented in Fig. 5.7. Image (a) and (b) are both from an identical position using the *Biophysics* AFM, but (c) and (d) were both captured using the *SINTEF* AFM. *544-1* was the most thoroughly examined. It was extremely hard to acquire sharp images of sample *544-1*, and very time-consuming to extract raw data.

Sample *544-1* had the highest QD density of all samples in this study. This can actually be seen by comparing image Fig. 5.7 (a) to similar $2\ \mu\text{m} \times 2\ \mu\text{m}$ AFM images of all other samples. Sample *504-1*, *514-2* and *514-4* clearly have larger and less dense QDs than *544-1*. The QDs of image (d) seem to grow systematically

along diagonal lines. Many of the QDs have grown together and they are hard to separate. The background is barely visible, but local height variation near the large QDs can be seen by assuming that the height distribution is the same for all QDs in the sample. Alternatively, the mean QD height near the large QDs is smaller than elsewhere. Sample *544-1* and *514-2* had the lowest measurable mean and maximum QD height of all samples.

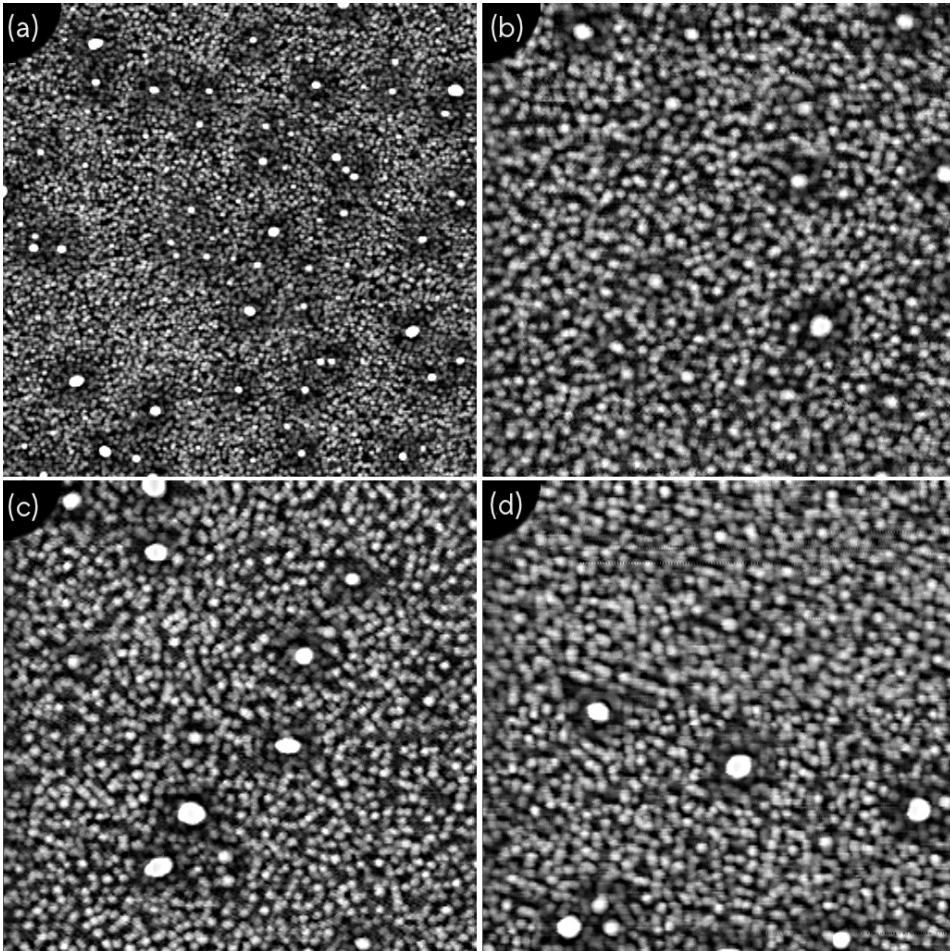


Fig. 5.7: $2\ \mu\text{m} \times 2\ \mu\text{m}$ (a) and $1\ \mu\text{m} \times 1\ \mu\text{m}$ AFM images (b), (c) and (d) of sample *544-1*, in three different locations. Image (a) and (b) are from the same location.

Sample *544-1* also had the highest density of large QDs. Most of the large QDs are surrounded by somewhat square-shaped areas, which later in this work will be named *square defects*. As seen in Fig. 5.7, some of these *square defects* have merged and some of them contain more than only a single large QD. The contrast and grey scale are the same in Fig. 5.7, as for all other AFM images in

this section. These *square defects* have been observed in images from both the *SIN-TEF* and the *Biophysics* AFM for all resolutions and all samples - except for *514-4*.

Until now, AFM images of varying scan size and from different samples have been shown. Raw data from AFM images were extracted and analysed, as described in Sec. 4.1. The numerical results are presented in the following sections, starting with QD density and followed by projected QD area and QD height - needed for the volume estimations in section 5.5.

5.2 QD density

The QD density is an essential characteristic of a InAs/GaAs(100) QD sample. QD density refers in this section to the density the majority QDs i.e. the relatively small ones, excluding the large QDs seen in most of the samples. QD density is a crucial parameter in the QD-IBSC design, and is controlled by growth parameters such as growth temperature and InAs thickness. Small QDs could be seen in all images presented in Sec. 5.1. Estimates of the QD density are listed in Table 5.1 below with relative uncertainty, from both AFM and SEM estimates. ρ_{500nm} and ρ_{1000nm} are based on AFM images from at least three different locations. ρ_{SEM} is based on SEM data, found by *Sedsel Fretheim Thomassen*. The relative uncertainty was smaller for most samples in the SEM estimates, as seen in Table 5.1. QD densities are plotted in Fig. 5.8. The data are plotted with error bars in three cases: estimated from $500\text{ nm} \times 500\text{ nm}$ AFM images (**black**), $1\text{ }\mu\text{m} \times 1\text{ }\mu\text{m}$ AFM images (**red**) and SEM images (**blue**). Fig. 5.8 reveals that sample *503-1* and *544-1* had largest relative uncertainty of all samples.

Table 5.1: The total QD density (ρ) and relative uncertainty (R) for the estimates $500\text{ nm} \times 500\text{ nm}$ AFM images (ρ_{500nm}), $1\text{ }\mu\text{m} \times 1\text{ }\mu\text{m}$ AFM images (ρ_{1000nm}) and SEM data (ρ_{SEM}).

Sample	ρ_{500nm} (10^{11} cm^{-2})	ρ_{1000nm} (10^{11} cm^{-2})	ρ_{SEM} (10^{11} cm^{-2})	R_{500nm} (%)	R_{1000nm} (%)	R_{SEM} (%)
503-1	1.00	1.13	1.10	10.6%	11.8%	1.6%
503-2	0.85	0.85	0.80	9.1%	7.0%	3.4%
504-1	0.68	0.71	0.57	1.9%	5.0%	3.7%
514-2	0.74	0.61	0.70	4.2%	0.9%	2.2%
514-4	0.51	0.52	0.58	0.2%	1.8%	2.6%
544-1	1.48	1.68	1.79	3.1%	4.7%	4.1%

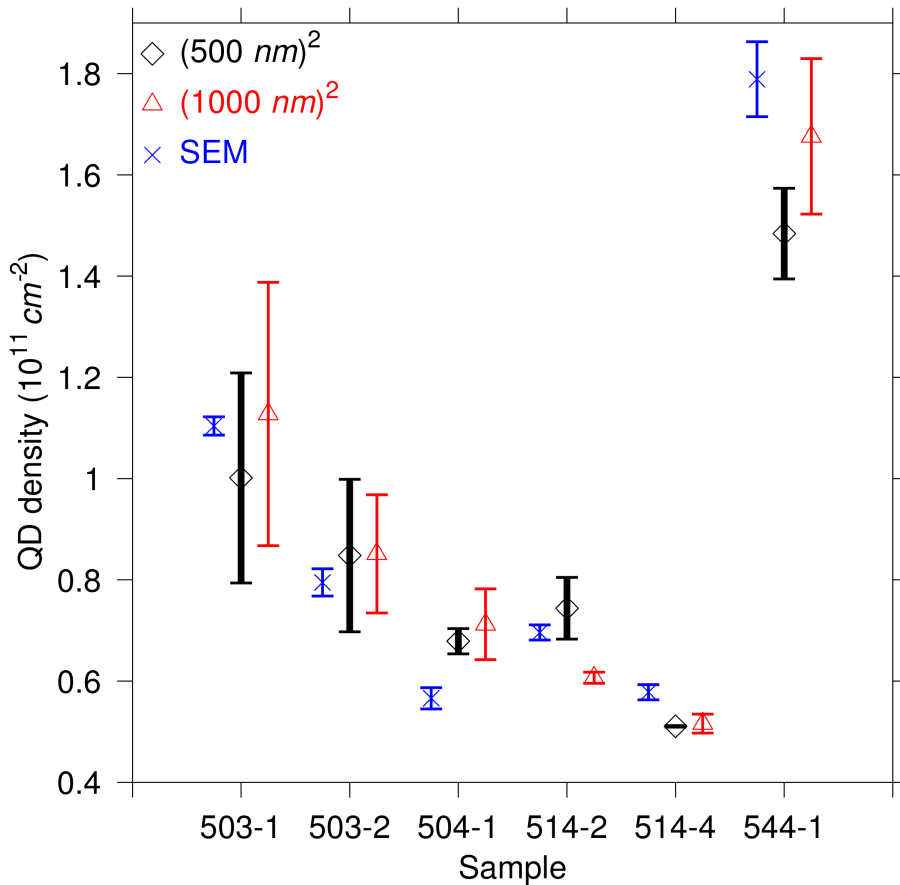


Fig. 5.8: The QD density estimated from $500 \text{ nm} \times 500 \text{ nm}$ AFM images (**black**), $1 \mu\text{m} \times 1 \mu\text{m}$ AFM images (**red**) and SEM data (**blue**), showing the error bars for each estimate.

An overlap between AFM and SEM data can be seen in Fig. 5.8 for sample *503-1*, *503-2* and *504-1*. SEM data deviates significantly from AFM data for sample *504-1* and *514-4*. The two estimates from AFM images seem to agree within the error bars for all samples, excluding sample *514-2*. For *514-2*, the $500 \text{ nm} \times 500 \text{ nm}$ AFM images predicts a higher QD density than $1 \mu\text{m} \times 1 \mu\text{m}$ AFM images.

It can be seen from Fig. 5.8 that sample *544-1* has the highest QD density of all the six samples. Sample *504-1* and *514-4* had the lowest QD density. According to the SEM data in Table 5.1, no significant difference in QD density was uncovered between *504-1* and *514-4*. However, ρ_{QD} was found to be significant lower for *514-4* than all samples for both $500 \text{ nm} \times 500 \text{ nm}$ and $1 \mu\text{m} \times 1 \mu\text{m}$ AFM images.

5.3 Projected QD area

Fig. 5.9 shows three estimates of the projected area per QD, presented with error bars for all parameters. One of the estimates are from SEM data (**Cross**). The mean area is based upon all QDs. The AFM estimates are from $500 \text{ nm} \times 500 \text{ nm}$ (**diamond**) and $1 \mu\text{m} \times 1 \mu\text{m}$ (**triangle**) AFM images. The various estimates give very different results. The AFM estimates from $500 \text{ nm} \times 500 \text{ nm}$ and $1 \mu\text{m} \times 1 \mu\text{m}$ AFM images deviates as much as 50%. The SEM estimates are not within the error bars of the AFM estimates for almost all samples. Hence, the estimated projected area from SEM does not seem to agree with similar estimates from the AFM data.

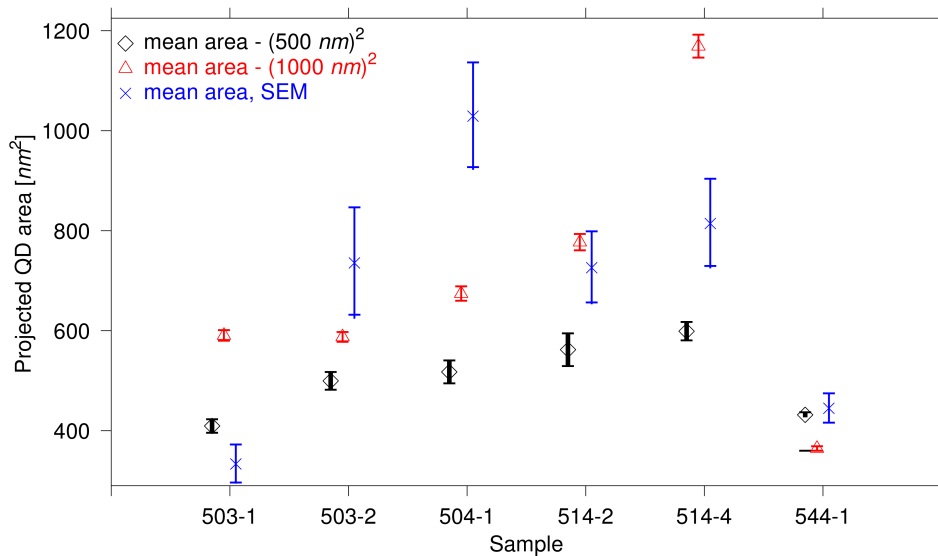


Fig. 5.9: The projected QD area as estimated from $500 \text{ nm} \times 500 \text{ nm}$ AFM images (**black**), $1 \mu\text{m} \times 1 \mu\text{m}$ AFM images (**red**), peak area (**blue**) and small QD area (**green**) from the from SEM images. The parameters are plotted with error bars.

Furthermore, it is clear from Fig. 5.9 that the projected areas from $500 \text{ nm} \times 500 \text{ nm}$ and $1 \mu\text{m} \times 1 \mu\text{m}$ AFM images does not fall within the error bars of each other. The estimates from $500 \text{ nm} \times 500 \text{ nm}$ and $1 \mu\text{m} \times 1 \mu\text{m}$ AFM images varies significantly, $1 \mu\text{m} \times 1 \mu\text{m}$ AFM images being significantly larger in all samples but *544-1*. The projected area from the $1 \mu\text{m} \times 1 \mu\text{m}$ AFM images is more coherent with the SEM data than the estimates from $500 \text{ nm} \times 500 \text{ nm}$ AFM images.

Discussion: Projected QD area

Why are the estimates from the AFM and SEM dissimilar? There could be several factors contributing to wrong estimates. The projected area per QD from AFM data is calculated from the number of pixels within the boundary of the masked grain. For SEM data, the projected QD area is estimated from a quantity called effective diameter. The effective diameter assumes that the QD has a circular shape. In practice, it is found by measuring the length of the grain boundary and dividing by π . This is a rough approximation to the real QD, which in most cases have an elliptic shape. This error accounts for an estimated relative error of less than 20%. This error adds to the typical measurement errors. The error in effective diameter could not alone explain the huge gap between the AFM and SEM estimates. There must be another source of error.

Recall that the quality of the tip could have a tremendous impact on the projected area of the QDs. The effect of the AFM tip was observed in several AFM images shown earlier in this chapter, and described thoroughly in previous studies. [37] The AFM typically measures a too large projected QD area. This might explain why the $(1000\text{nm})^2$ estimates generally are larger than similar estimates from $(500\text{nm})^2$ images. The $(1000\text{nm})^2$ estimates are measured less accurately, and thus appear to be larger than found in $(500\text{nm})^2$ estimates.

SEM is much more precise method compared to AFM for estimating projected QD area and diameter. The SEM estimates were expected to give lower projected QD areas than the AFM estimates, but the opposite trend was seen in Fig. 5.9. An explanation might be that the algorithm for the QD rim extraction from the SEM images possibly overestimates the rim length. Detailed analysis of this issue is beyond the scope of this thesis. A hybrid SEM / AFM volume estimation method, V_{fusion} , was introduced to possibly reduce the error in QD volume estimates - combining the best from both imaging techniques.

5.4 QD height

Fig. 5.11 shows the average estimated QD height, (a) maximum QD height (\bar{H}) and (b) mean QD height (\bar{h}). The numerical values are found in Table 5.2. The estimates are from $500 \text{ nm} \times 500 \text{ nm}$ (**diamond**) and $1 \mu\text{m} \times 1 \mu\text{m}$ AFM images (**triangle**). All parameters are defined **inside** a masked grain, and are estimated from several (≥ 3) AFM images. The QD height (\bar{H}) was found by subtracting the maximum from the minimum z-value, occurring inside the grain, and \bar{h} by finding the difference (**inside** a grain) between the mean of all z-values and the minimum z-value inside, as seen in Table 5.3 and Fig. 5.10. For all samples, 95% of all $500 \text{ nm} \times 500 \text{ nm}$ AFM images had QDs with a height between 0.75 nm and 2.26 nm. AFM is generally expected to give better and more reliable height estimates than SEM. [36]

Table 5.2: The mean (\bar{h}) and maximum (\bar{H}) QD height estimated from $500 \text{ nm} \times 500 \text{ nm}$ (\bar{H}_{500nm} , \bar{h}_{500nm}) and $1 \mu\text{m} \times 1 \mu\text{m}$ (\bar{H}_{1000nm} , \bar{h}_{1000nm}) AFM images.

Sample	\bar{H}_{500nm} (nm)	\bar{H}_{1000nm} (nm)	\bar{h}_{500nm} (nm)	\bar{h}_{1000nm} (nm)
503-1	1.73	2.05	0.89	0.99
503-2	1.80	2.18	0.89	1.07
504-1	1.96	2.10	0.98	1.04
514-2	1.10	1.44	0.56	0.75
514-4	1.42	2.01	0.78	0.96
544-1	1.03	1.40	0.59	0.59

Table 5.3: Definitions of z-values **occurring inside** a grain.

Parameter	Description
\bar{z}	mean of all z-values
z_{min}	minimum z-value
z_{max}	maximum z-value
$\bar{h} = \bar{z} - z_{min}$	mean QD height
$\bar{H} = z_{max} - z_{min}$	max. QD height

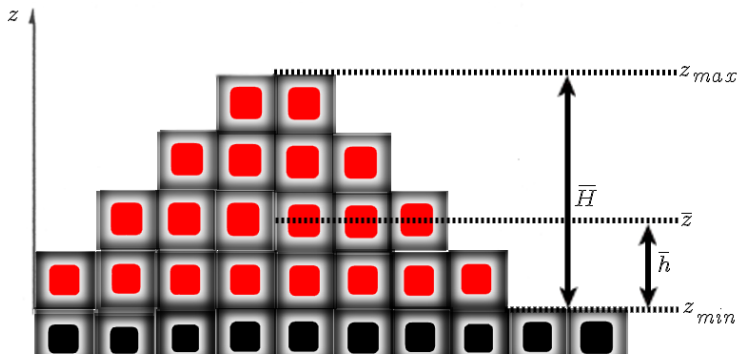


Fig. 5.10: A illustration of the z -values occurring inside a grain. The masked QD/grain is in red, and the unmasked area in black.

Two estimates of maximum QD height \bar{H} are presented in Fig. 5.11 (a). Sample *514-2* and *544-1* have the lowest QD height of all samples. Sample *514-4* had the largest deviation between the two estimates (**diamond** and **triangle**). Both estimates seem to suggest that sample *514-4* has higher QDs than *514-2* and *544-1*. The QD height is about the same in *503-1*, *503-2* and *504-1*. *503-2* or *504-1* had the highest QDs, depending on choice of estimate. Correlations between maximum QD height (\bar{H}) and volume estimates were found. For instance, the correlation for *surface area method* (V_h) was estimated to be 0.71 (see Sec. 4.4.3). That is not unexpected since QD volume is a function of the QD height.

Fig. 5.11 (b) shows the mean QD height (\bar{h}) of all z values within the boundary mask. The mean QD height roughly follows the same pattern as seen in Fig. 5.11 (a). Little deviation in \bar{h} were seen between *503-1*, *503-2* and *504-1*. Similarly, no significant difference in \bar{h} were found between *514-2* and *544-1*.

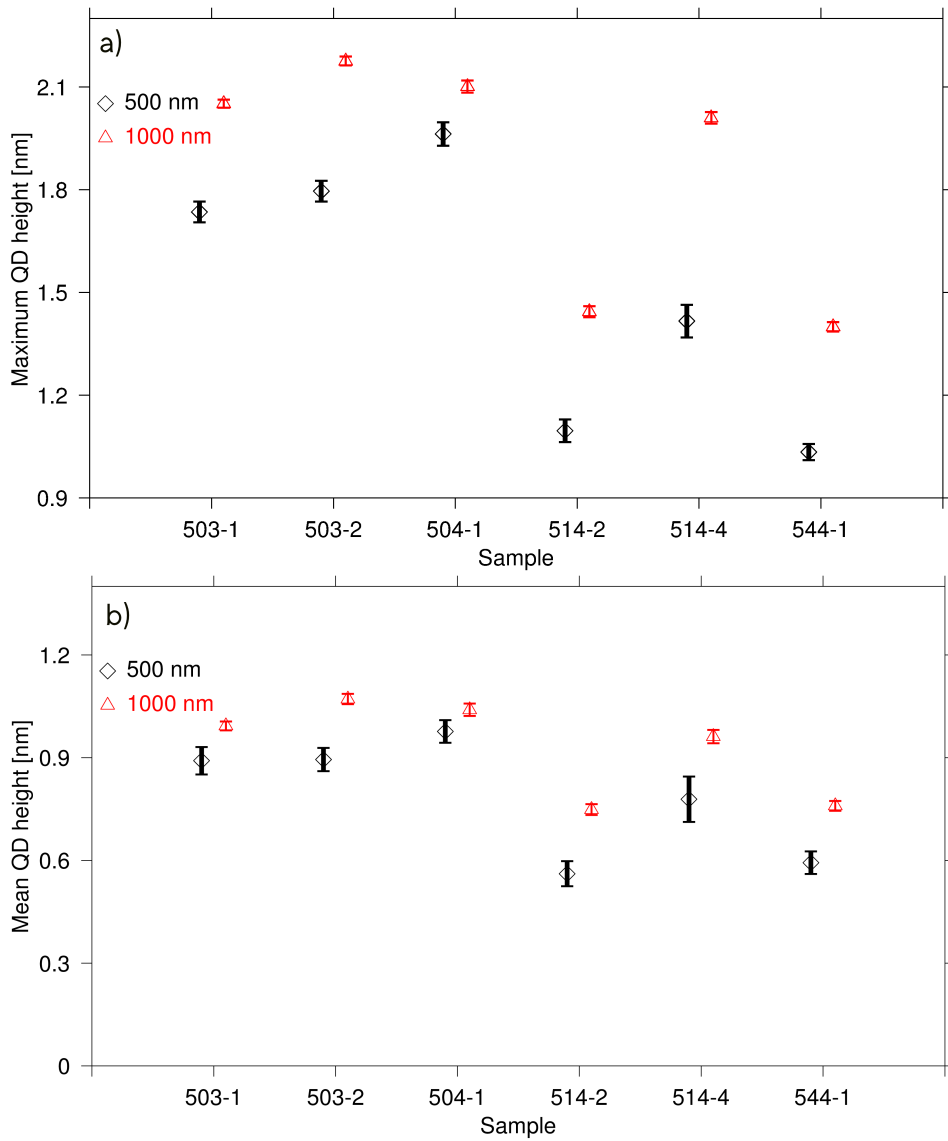


Fig. 5.11: The maximum (a) and mean (b) QD height plotted with error bars, estimated from both $500\text{ nm} \times 500\text{ nm}$ (**diamond**) and $1\text{ }\mu\text{m} \times 1\text{ }\mu\text{m}$ AFM images (**triangle**). Maximum (\bar{H}) and mean (\bar{h}) QD height are defined in Table 5.3.

Discussion: QD height

The height of the QDs shown in Fig. 5.11 and Table 5.3 were lower than found in a previous studies of the same samples. Fig. 5.12 shows height distributions for sample *503-1*, *503-2* and *504-1* from the previous study. [41] The red lines in Fig. 5.12 indicate the QD heights obtained from $(500\text{ nm})^2$ estimates, see Table 5.2.

All QD heights from this master work were significantly lower than the peak heights in Fig. 5.12. Peak QD height refers to the maximum QD height estimated from a distribution of all observed QDs. The peak height could be a superposition of two or more height distributions, as the dashed lines indicate in Fig. 5.12. The curves plotted in Fig. 5.12 are based on AFM images taken relatively soon after fabrication. The images were not deconvoluted before raw data extraction. In this study, the QD height increases slightly from *503-1*, *503-2* to *504-1* for estimates from $(500\text{ nm})^2$ images. However, for the estimates from the $(1000\text{ nm})^2$ images - the results were inconclusive. In Fig. 5.12, the peak height in *504-1* (c) was significantly larger than *503-2* (b).

The low QD height obtained in this study is not likely a result of image processes. In Sec. 4.1.3, the deconvolution was found to *increase* the maximum QD height. Deconvolution had varying impact on the different samples in this study, as seen in Fig. 4.4. Corrections from deconvolution were done for sample *514-4*, *504-1* and *514-2*. *503-1*, *503-2* and *544-1* had little deviations and few corrections.

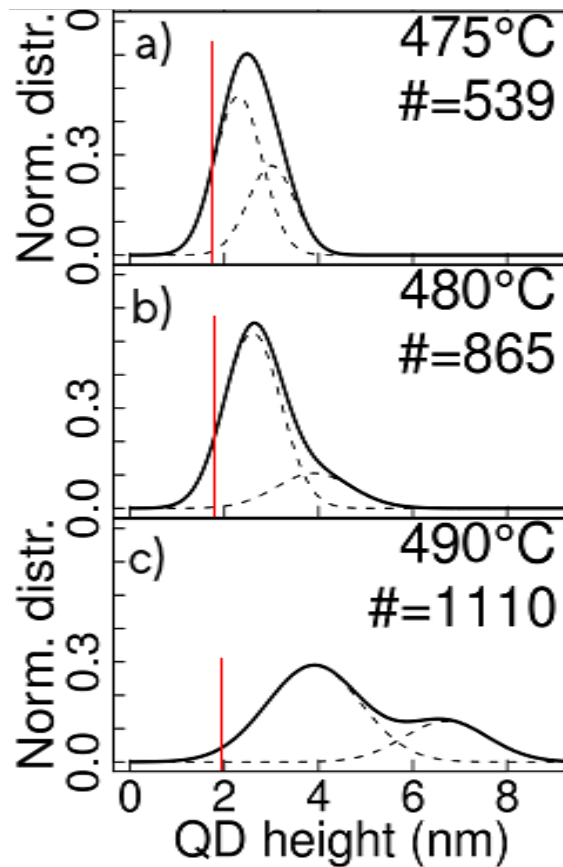


Fig. 5.12: The height distribution for (a) 503-1 (475 °C), (b) 503-2 (480 °C) and (c) 504-1 (490 °C) found in a previous study. [41] The maximum QD heights from this master work, estimated from $(500 \text{ nm})^2$ images, are shown as red lines in the figure (a) 1.73 nm, (b) 1.80 nm and (c) 1.96 nm. All new values from this study were outside 2.35σ of the mean peak for each height distribution.

The QD height varies from sample to sample naturally as a result of different growth parameters. However, not all variation in QD height may come directly from the growth process. Some of the deviation in the QD height could be explained by other mechanisms, such as *oxidation*.

Fig. 5.13 illustrates how oxidation can affect the measured QD height. The samples were exposed to air over a period of several months. Many metals are known to form oxides over time, when exposed to air. Gallium (Ga) and Indium (In) are not particularly reactive in air compared to Arsenic (As). It is probably As that will be oxidized over time. Arsenic has material properties resembling elements in the same group in the periodic system, such as Phosphorus (P) and Antimony (Sb). Arsenic forms compounds like crystalline, hygroscopic oxides As_2O_3 and As_2O_5 , which are soluble in water. It is also believed that oxides of InGaAs could

form. [42] This oxide layer could coat the valleys, as well as the peaks or QDs. The QD height could be effectively lowered if the oxidation process goes at a notable higher rate in the deep valleys, than near the QDs. The thickness of the oxide layer is time-dependent and depends on the availability of Oxygen. Exactly how thick the oxide layers are, and how rapidly it grows, is not known in this study.

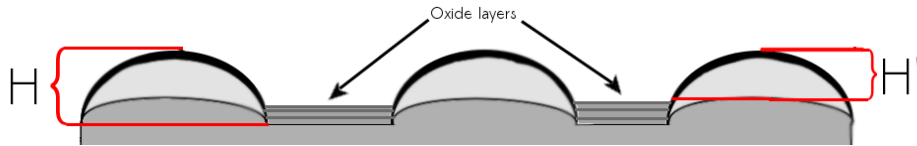


Fig. 5.13: H is the QD height before formation of an oxide layer. H' is the measured QD height at the lab after the sample has been exposed to air over some period of time.

It is hard to predict what impact the oxidation processes had on the samples examined in this study. The measurements were not taken over a short period of time, but spread out over several months. Most importantly, this study was carried out 6-12 months after the measurements presented in Fig. 5.12. Depending on how fast the oxidation process is, the different AFM images could have varying oxide layer thickness at the time the images were captured. *Oxidation* might even explain why the measured QD height is lower in study, compared to Fig. 5.12 and similar studies. It is possible that low valleys oxidise at a faster rate than less deep valleys, because the protecting InAs layer is thinner - thus, effectively lowering the measured QD height. Unfortunately, a thoroughly investigation of oxide layer thickness was beyond the scope of this study. It is possible that the height uncertainty can be reduced by doing all the AFM imaging over a short period of time, right after the fabrication of the samples.

5.5 Total QD volume

Volume was estimated independently from both $500\text{ nm} \times 500\text{ nm}$ and $1\text{ }\mu\text{m} \times 1\text{ }\mu\text{m}$ AFM images, using eight different methods. These methods were described in Sec. 4.3. One method exploit both AFM and SEM data. AFM and SEM data were presented in Table 5.1 and Fig. 5.9.

5.5.1 From $500\text{ nm} \times 500\text{ nm}$ AFM images

The total estimated QD volume converted to equivalent monolayers is presented in Fig. 5.14, estimated using eight different approaches from $500\text{ nm} \times 500\text{ nm}$ AFM images only. The QD volume is estimated from at least three locations from each sample. Table 5.4 shows how the eight estimation methods correlate to each other. V_h , $V_{h\text{-mean}}$ and $V_{h\text{-max}}$ is strongly correlated, as seen in Table 5.4. Similarly, the a strong correlation between $V_{h\text{-mean},0}$ and $V_{h,0}$ was 0.99 - and 0.90 between $V_{h\text{-max},0}$ and $V_{h,0}$. Consequently, $V_{h\text{-mean},0}$, $V_{h,0}$, and $V_{h\text{-max},0}$ all follows the

same trend of increasing estimated QD volume from sample *503-1*, *503-2* and *504-1*, and almost the same volume for *514-2*, *514-4* and *544-1*. *503-1*, *503-2* and *504-1* and have very similar estimated QD volumes for V_{h-mean} , V_h , and V_{h-max} . The trend is the same for *514-2*, *514-4* and *544-1*, but these estimates were all smaller than *503-1*, *503-2* and *504-1*.

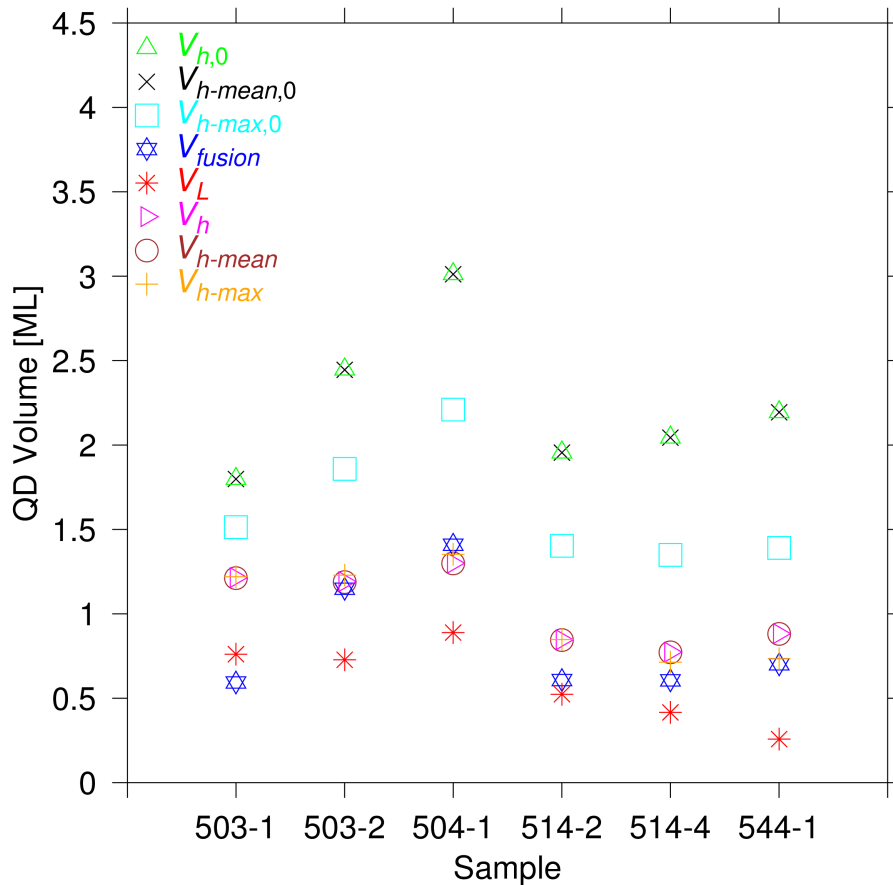


Fig. 5.14: Total QD volume in monolayers (ML) from eight estimates for all six samples, as described in Sec. 4.3. Calculated from several $500\text{ nm} \times 500\text{ nm}$ AFM images for each sample.

Table 5.4: Correlation table of all eight volume estimates from 500 nm × 500 nm AFM images.

Method	h,0	h-mean,0	h-max,0	L	fusion	h	h-mean	h-max
h,0	1.00	0.99	0.90	0.49	0.96	0.55	0.55	0.54
h-mean,0	0.99	1.00	0.90	0.48	0.96	0.55	0.55	0.54
h-max,0	0.90	0.90	1.00	0.81	0.97	0.83	0.83	0.85
L	0.49	0.48	0.81	1.00	0.66	0.90	0.90	0.96
fusion	0.96	0.96	0.97	0.66	1.00	0.72	0.72	0.72
h	0.55	0.55	0.83	0.90	0.72	1.00	0.99	0.98
h-mean	0.55	0.55	0.83	0.90	0.72	0.99	1.00	0.98
h-max	0.54	0.54	0.85	0.96	0.72	0.98	0.98	1.00

V_{fusion} was the only volume estimate that included SEM data. It is apparent from Fig. 5.14 that V_{fusion} follows the same increasing pattern from *503-1*, *503-2* to *504-1*. V_{fusion} is stronger correlated to $V_{h-mean,0}$, $V_{h-max,0}$ and $V_{h,0}$ than to V_h , V_{h-mean} and V_{h-max} , as seen in Table 5.4. However, V_{fusion} deviates very little from V_h , V_{h-mean} and V_{h-max} if *503-1* is omitted from the data set. V_{fusion} fits better, in terms of absolute volume, to the estimates from V_h , V_{h-mean} and V_{h-max} . $V_{h-mean,0}$, $V_{h,0}$ results in volumes estimates that typically are 2-3 times larger than V_{fusion} and V_h .

The final volume method utilized in this section was V_L . V_L is, mathematically, the most advanced method employed in this work. V_L correlates strongly to V_h , V_{h-mean} and V_{h-max} , and more weakly to $V_{h-max,0}$. V_L deviates from all other volume estimation methods for sample *544-1*. V_L had generally lower total QD volume than all other methods.

The observations above, summarized

- ◇ $V_{h-mean,0}$, $V_{h,0}$, and $V_{h-max,0}$: strongly correlated; different volumes for *503-1*, *503-2* and *504-1*, but non-significant deviations in estimated volume for *514-2*, *514-4* and *544-1*.
- ◇ V_{h-mean} , V_h , and V_{h-max} : strongly correlated; same volume for *503-1*, *503-2* and *504-1* (group 1) and *514-2*, *514-4* and *544-1* (group 2).
- ◇ V_{fusion} strongly correlated to $V_{h-mean,0}$, $V_{h,0}$, and $V_{h-max,0}$, but generally has an absolute volume that is closer to V_{h-mean} , V_h , and V_{h-max} .
- ◇ V_L gives a lower estimate than the other methods for all samples (excluding *503-1*), but seem to roughly follow the same pattern as V_{h-mean} , V_h , and V_{h-max} - except for sample *544-1*.

5.5.2 From $1\ \mu\text{m} \times 1\ \mu\text{m}$ AFM images

Fig. 5.15 shows the corresponding total QD volume estimated from $1\ \mu\text{m} \times 1\ \mu\text{m}$ AFM images only. An first, and most obvious observation from Fig. 5.15, is that the estimated QD volumes is larger for all eight estimation methods when compared to Fig. 5.14. The deviations is significant and more than 30% in all cases, and sometimes above 150%. Even though the absolute estimated volumes are deviating much, can some similarities be drawn from Fig. 5.14 and 5.15.

Table 5.5 is a correlation table illustrating the relationship between the eight volume estimation methods. A strong correlation is seen between V_h , V_{h-mean} and V_{h-max} , analogously to Fig. 5.14. There is equivalently a close relationship between $V_{h,0}$ and $V_{h-mean,0}$, as seen in Table 5.5. Similarly, the relationship between V_{fusion} and the other estimation methods are much weaker for Fig. 5.14 compared to 5.15. The pattern for V_{fusion} is very similar in both Fig. 5.14 and 5.15, and are strongly correlated (0.96). This is the strongest correlation between Fig. 5.14 and 5.15 of all QD volume estimation methods.

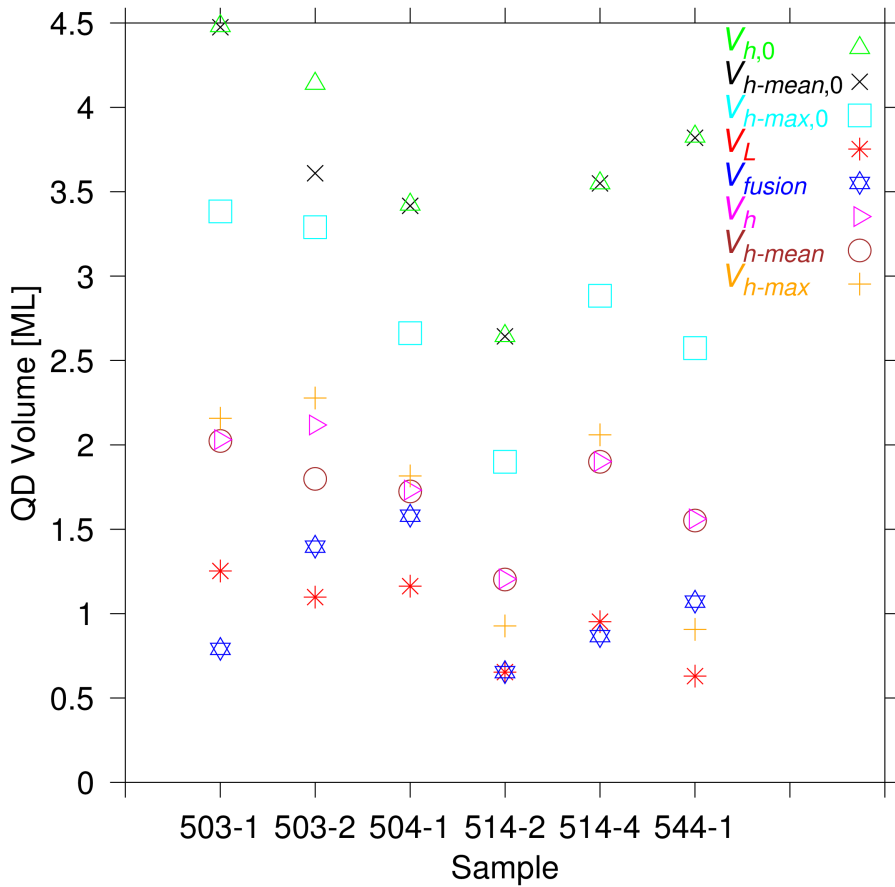


Fig. 5.15: Total QD volume in monolayers (ML) from eight estimates, as described in Sec. 4.3. $1\ \mu\text{m} \times 1\ \mu\text{m}$ AFM images.

Table 5.5: A correlation table of all eight volume estimates from $1\ \mu\text{m} \times 1\ \mu\text{m}$ AFM images.

Method	h,0	h-mean,0	h-max,0	L	fusion	h	h-mean	h-max
h,0	1.00	0.94	0.94	0.61	0.22	0.85	0.82	0.63
h-mean,0	0.94	1.00	0.84	0.56	0.07	0.72	0.82	0.51
h-max,0	0.94	0.84	1.00	0.78	0.29	0.98	0.93	0.86
L	0.61	0.56	0.78	1.00	0.41	0.80	0.81	0.90
fusion	0.22	0.07	0.29	0.41	1.00	0.37	0.23	0.33
h	0.85	0.72	0.98	0.80	0.37	1.00	0.93	0.93
h-mean	0.82	0.82	0.93	0.81	0.23	0.93	1.00	0.87
h-max	0.63	0.51	0.86	0.90	0.33	0.93	0.87	1.00

The estimated volume from $V_{h,0}$ and $V_{h-mean,0}$ decreases from *503-1*, *504-1* to *514-2*. V_h , V_{h-mean} and V_{h-max} are analogously decreasing, relative to *503-1*, for sample *504-1* to *514-2*. Similarly, there seems to be an increasing volume from *514-2*, *514-4* to *544-1* for $V_{h,0}$ and $V_{h-mean,0}$. V_h , V_{h-mean} , V_{h-max} and $V_{h-max,0}$ increases from *514-2* to *514-4*, but not for *544-1*. $V_{h-max,0}$ roughly follows the same pattern as V_{h-max} , as seen in Table 5.5. V_{fusion} does not strictly follow the same pattern as any other estimation method, reflected in Table 5.5. V_{fusion} have increasing volume from *503-1*, *503-2* to *544-1*, and the volume is raising from *514-2*, *514-4* to *544-1*. $V_{h,0}$, $V_{h-max,0}$, $V_{h-mean,0}$ and V_{fusion} all have increasing volume from *514-2*, *514-4* to *544-1*. The trend is the same for V_h , V_{h-mean} and V_{h-max} , ignoring sample *544-1*.

The general findings from Fig. 5.15 and Table 5.5 are:

- ◇ $V_{h,0}$, $V_{h-mean,0}$, $V_{h-max,0}$ strongly correlated, but also a little weaker correlated to V_h , $V_{h,mean}$, V_{h-max} .
- ◇ V_h , $V_{h,mean}$, V_{h-max} strongly correlated, and follows the same pattern.
- ◇ V_L and V_{h-max} roughly follow the same pattern as V_h . V_L and V_{h-max} are accordingly smaller and larger relative to V_h for all samples.
- ◇ V_{fusion} not correlated to any of the other estimation methods. Correlated to V_{fusion} in Fig. 5.14.
- ◇ $V_{h,0}$, $V_{h-mean,0}$, followed by $V_{h-max,0}$, estimate the highest absolute QD volumes. The estimates from $V_{h,0}$, $V_{h-mean,0}$ are about 2-3 times greater than V_h , $V_{h,mean}$. V_L and V_{fusion} estimate the lowest absolute QD volumes.

5.5.3 Sample homogeneity

The samples in this study had variations in QD density and homogeneity between the samples and locations. All sample pieces were cut from the centre region of the 1/4-wafer. In general, the centre region is the most homogeneous region of the 1/4-wafer. [37] Inhomogeneity was still observed, certainly more pronounced in some samples than others. Fig. 5.16 and 5.17 show $500\text{ nm} \times 500\text{ nm}$ and $2\text{ }\mu\text{m} \times 2\text{ }\mu\text{m}$ AFM images from each sample. The images in Fig. 5.16 and 5.17 are in the same order as in Table 3.1 : (a) *503-1*, (b) *503-2*, (c) *504-1*, (d) *514-2*, (e) *514-4* and (f) *544-1*. The nominal growth temperature and deposited amount of InAs during growth are indicated for each sample in the figure text. It was easier to attain high-quality images of low-density samples like *514-2* and *514-4*, and almost impossible to capture images of the same kind of quality from samples like *544-1*.

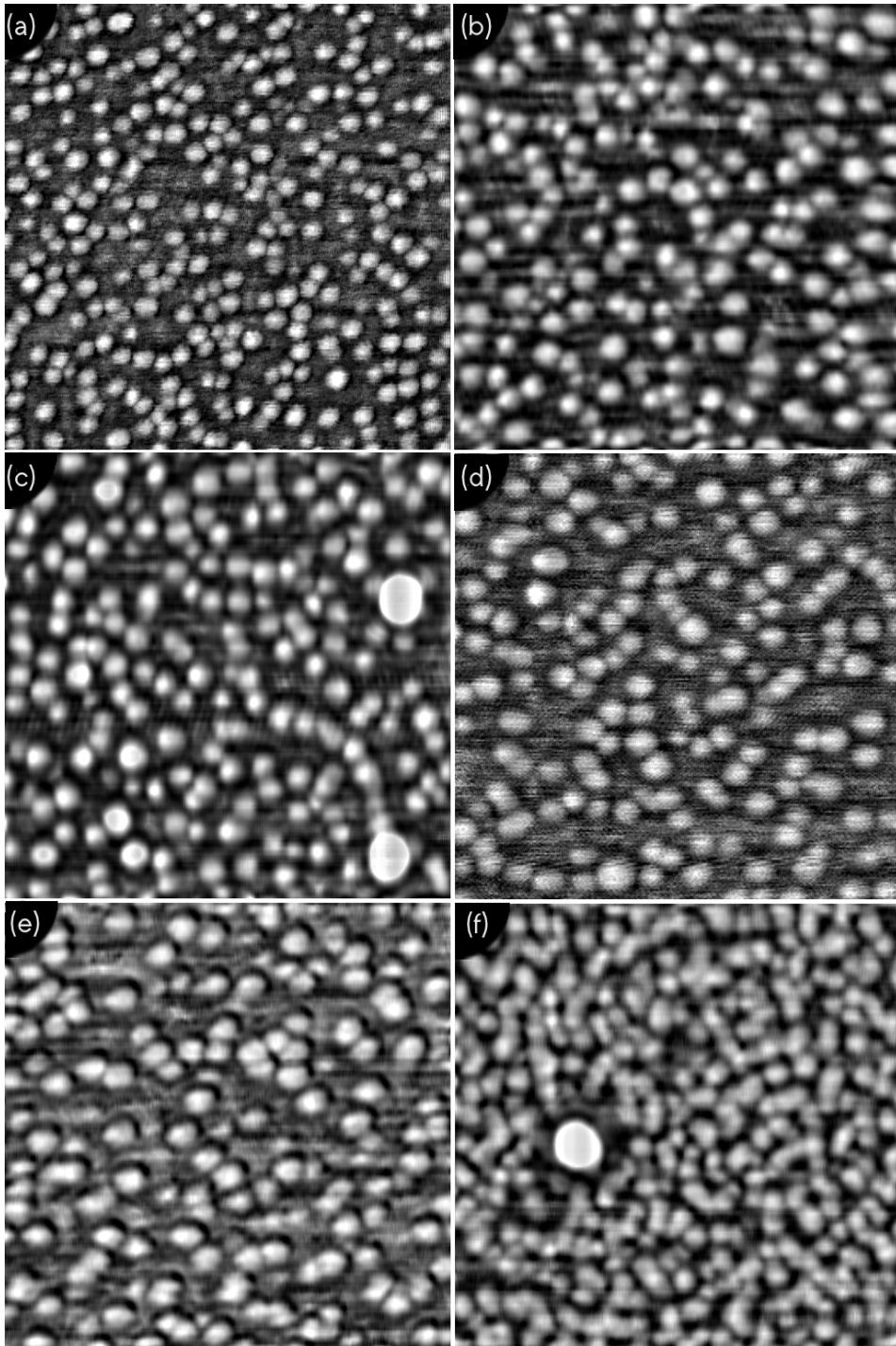


Fig. 5.16: $500\text{ nm} \times 500\text{ nm}$ AFM images of all six sample pieces, as described in Table 3.1. (a) *503-1* (475°C , 2.3 ML), (b) *503-2* (480°C , 2.3 ML), (c) *504-1* (490°C , 2.3 ML), (d) *514-2* (480°C , 2.1 ML), (e) *514-4* (480°C , 1.9 ML) and (f) *544-1* (455°C , 2.3 ML).

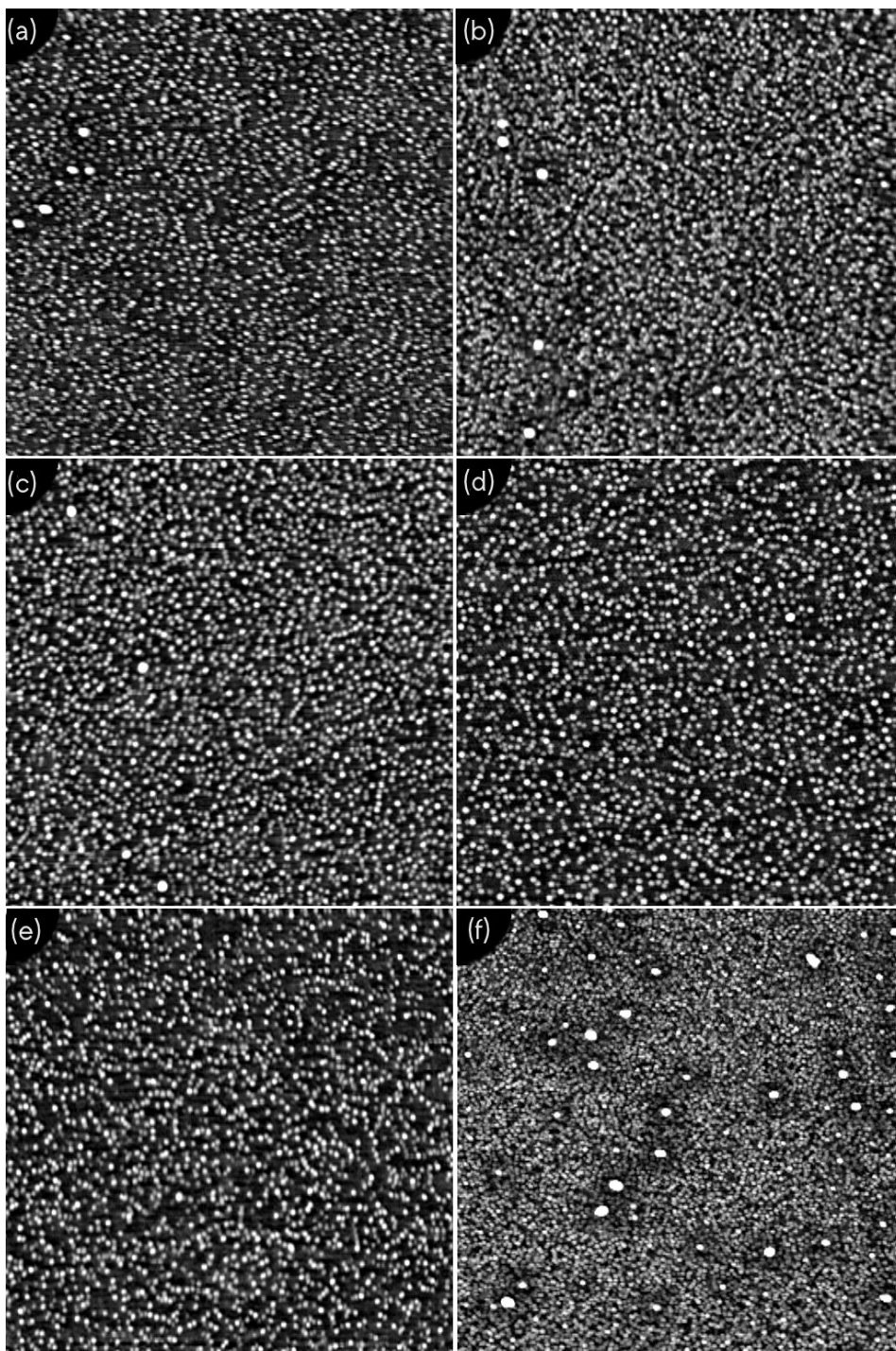


Fig. 5.17: $2\ \mu\text{m} \times 2\ \mu\text{m}$ AFM images of all six sample pieces, as described in Table 3.1. (a) *503-1* (475°C , 2.3 ML), (b) *503-2* (480°C , 2.3 ML), (c) *504-1* (490°C , 2.3 ML), (d) *514-2* (480°C , 2.1 ML), (e) *514-4* (480°C , 1.9 ML) and (f) *544-1* (455°C , 2.3 ML).

Sample homogeneity could most certainly have an impact on volume estimates, and is a potential source of error. Two samples were carefully selected to examine the effect of inhomogeneity: $504-1$ and $514-4$. Fig. 5.19 has $500\text{ nm} \times 500\text{ nm}$ and $1\text{ }\mu\text{m} \times 1\text{ }\mu\text{m}$ AFM images of $504-1$ from three different locations, as indicated in the figure. Fig. 5.18 shows the estimated total QD volume for sample the corresponding AFM images, in the three locations. The QD volumes to the left and right are estimated from $500\text{ nm} \times 500\text{ nm}$ and $1\text{ }\mu\text{m} \times 1\text{ }\mu\text{m}$ AFM images, respectively.

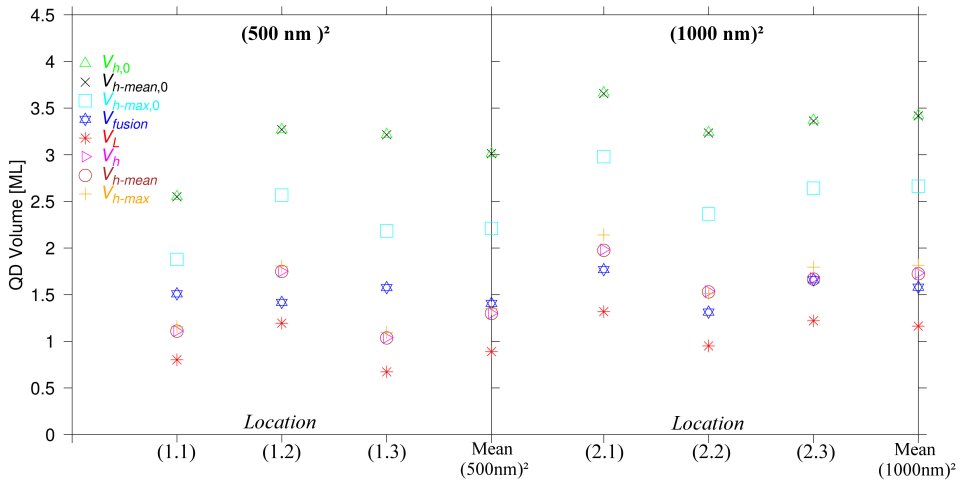


Fig. 5.18: Total estimated volume in equivalent monolayers (ML) from eight estimates for $500\text{ nm} \times 500\text{ nm}$ (1.1), (1.2), (1.3) and $1\text{ }\mu\text{m} \times 1\text{ }\mu\text{m}$ (2.1), (2.2), (2.3) AFM images of sample $504-1$, in three different locations - as indicated in the figure. The corresponding AFM images are shown in Fig. 5.21.

The $500\text{ nm} \times 500\text{ nm}$ AFM images have varying image quality, as seen in Fig. 5.19. The QDs in location (1.3) look flat, as a result of a more blunt tip. The change in tip quality might explain why V_h , V_{h-mean} , V_L and $V_{h,max}$ are larger in image (1.2) relative to image (1.1), as seen in Fig. 5.18. The methods using the global fix zero plane result in the same estimated volume for image (1.2) and (1.3). Problems could arise when QDs are merged close together, as seen at several places in image (1.3). Recall from chapter 3, for the methods using a local zero plane, the zero reference point was chosen as the lowest z value within the boundary mask. Some of the mask does not cover the background properly if the masked grain has merged with enveloping QDs. This could potentially give an underestimation, but is probably a greater problem in samples with higher QD densities ($503-1$ and $544-1$). There are eight methods to estimate the QD volume, as described in Sec. 4.3. The general trend is that the total QD volume is larger in image (1.2) than in image (1.3). It is hard to conclude that the actual QD volume is different in image (1.2) relative to image (1.3), because of the quality of the QDs in image (1.3). As discussed above, a blunt tip and merged QD results in an underestimate in QD volume - as seen in Fig. 5.18 (I).

Sample *504-1* is an example of an inhomogeneous sample. The $500\text{ nm} \times 500\text{ nm}$ and $1\text{ }\mu\text{m} \times 1\text{ }\mu\text{m}$ AFM images shown in Fig. 5.19 give some contradicting results. The estimated volume is smaller in image (2.2) relative to image (2.1) or (2.3), only opposed by V_L and/or V_{fusion} . The volume in image (2.2) is not significantly smaller than image (2.3), but the volume in (2.1) is significantly larger than in both (2.2) and (2.3). That is, $(1000\text{nm})^2$ estimates suggest a opposite trend than found for the $(500\text{nm})^2$. A blunt tip in (1.3) might account for some of the deviation, as discussed above. Unfortunately, it could not explain the aberration between (1.1) and (2.1). The mean values were calculated for all samples to increase the accuracy of the volume estimates. The mean value of $(1000\text{nm})^2$ estimates has an excess volume of 0.5 ML, compared to the $(500\text{nm})^2$ estimates, as seen in Fig. 5.18.

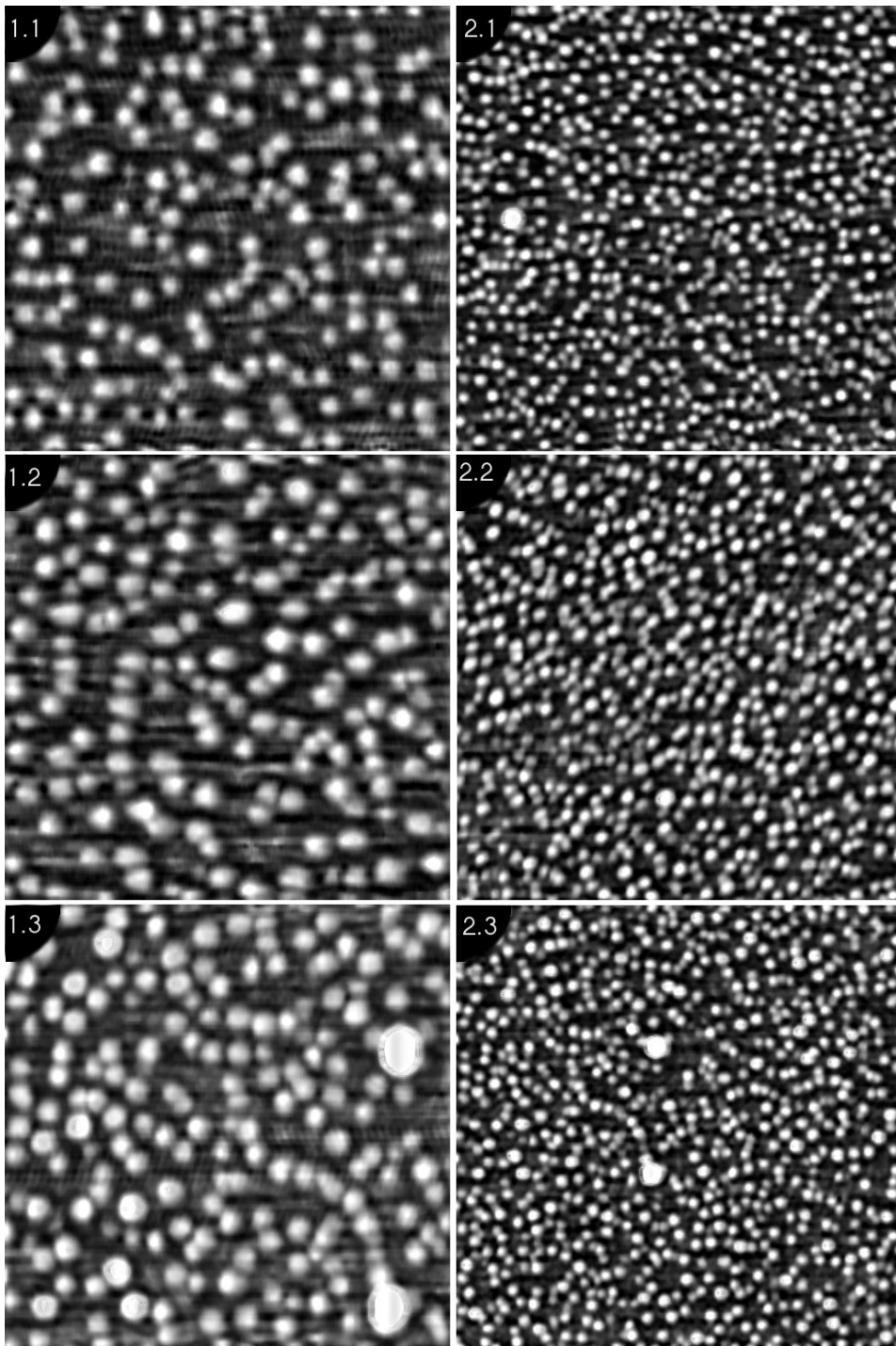


Fig. 5.19: 500 nm × 500 nm (1.1), (1.2), (1.3) and 1 μm × 1 μm (2.1), (2.2), (2.3) AFM images from sample *504-1*, in three locations - as indicated in Fig. 5.18.

Fig. 5.21 shows three $500\text{ nm} \times 500\text{ nm}$ (3.1), (3.2), (3.3) and three $1\text{ }\mu\text{m} \times 1\text{ }\mu\text{m}$ (4.1), (4.2), (4.3) AFM images from sample 514-4. The estimated total QD volumes for the images in Fig. 5.21 are presented in Fig. 5.20.

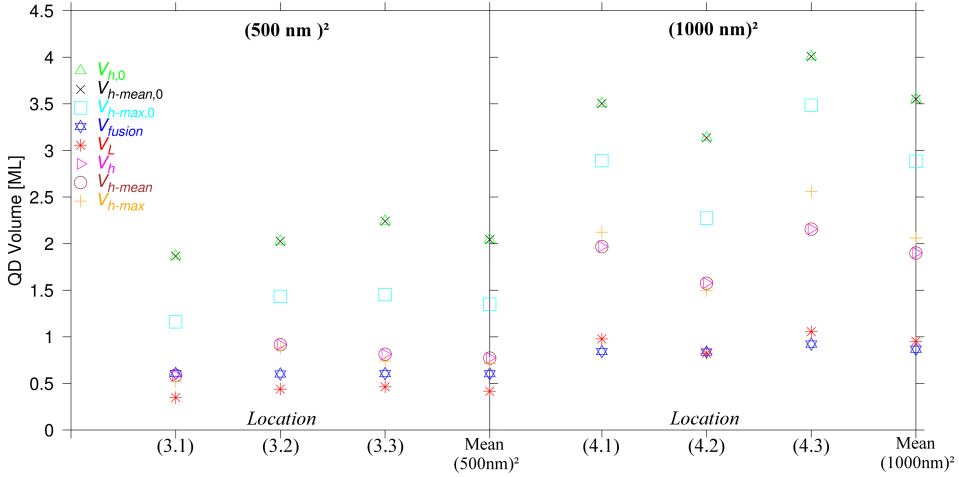


Fig. 5.20: Total estimated volume in equivalent monolayers (ML) from eight estimates of sample 514-4 for $500\text{ nm} \times 500\text{ nm}$ (3.1), (3.2), (3.3) and $1\text{ }\mu\text{m} \times 1\text{ }\mu\text{m}$ (4.1), (4.2), (4.3) AFM images, in three different locations - as indicated in the figure. The corresponding AFM images are shown in Fig. 5.21.

Sample 514-4 is more homogeneous than 504-1. There is less variation in estimated QD volume between the images in Fig. 5.20 compared to Fig. 5.18. The estimated volume for the *surface area method* (V_h) is smaller in (4.2) and larger in (4.3) - compared to image (4.1). The QDs in Fig. 5.21 (3.1), (3.2) and (3.3) seem enlarged and flat. The effect is not related to the sharpness of the tip, since all three AFM images were captured using a different tip. The uneven, slightly cubic shape of the QDs does not appear in the unconvoluted AFM images, and is a known effect of convolution (most apparent in image (3.3)). Image (3.3) has weak interference in the background. There are large, open areas without visible QDs in the AFM images. One abnormally large QD can be seen in image (3.2), but it is way smaller than typical large QDs examined in other samples.

Fig. 5.21 is an example of a homogeneous sample, in contrast to Fig. 5.19. The images shown in Fig. 5.21 are very much alike. The same consistency can be seen in Fig. 5.20. The only exception is image (4.2). The estimated volume is lower in image (4.2) relative to image (4.1) and (4.3), caused by a lower QD height. The $(500\text{ nm})^2$ volume estimates were smaller than corresponding $(1000\text{ nm})^2$ estimates for all methods.

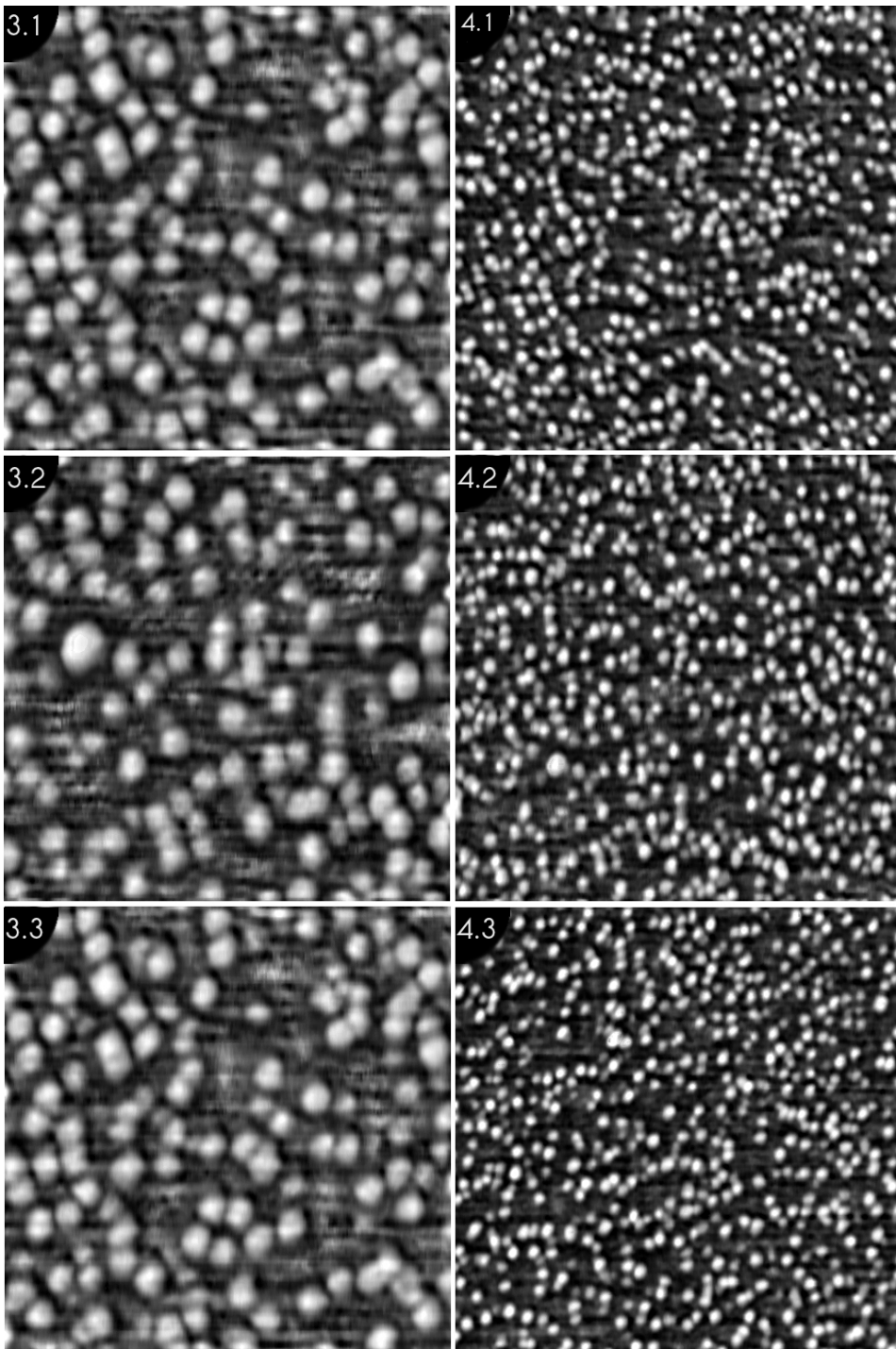


Fig. 5.21: 500 nm \times 500 nm (3.1), (3.2), (3.3) and 1 μ m \times 1 μ m (4.1), (4.2), (4.3) AFM images from sample *504-1*, in three locations - as indicated in Fig. 5.18.

5.5.4 Discussion: Estimates of total QD volume

Eight methods have been presented using two different scan sizes. This section aims to find the most suitable method for estimating the total QD volume from the samples investigated in this study.

Which method?

Eight different approaches to estimate QD volume were presented in Sec. 4.3. Each method has its own strengths and weaknesses. Choice of zero plane was crucial to determine the height and volume of the QD. In some of the methods, namely $V_{h,0}$, $V_{h-mean,0}$ and $V_{h-max,0}$, the fix zero point was used to extrapolate a global zero plane. The QD height was relative to the same reference z value for all QDs. It is not a correct approximation, since the fix zero plane usually is extrapolated below the local valleys, surrounding the QDs. As a result, these methods add the volume a few layers below the QDs; making the volume a overestimate.

V_{h-mean} , V_h , V_{h-max} , V_{fusion} and V_L were methods, that instead of a global reference point, employed a local zero plane. In the four first methods, the reference z value was simply z_{min} - or the minimal z value found inside of the mask of covering each QD. The mask was chosen to cover a area including the QD and the surrounding area, sometimes manually or checked by inspection. The height was then measured relative to the lowest valley. Problems can arise from this method if the mask covers an atomic step, a deep eroded valley or an area that contains several QDs that have melted together. The first two effects are examples of underestimates, and the last is an example of an overestimate. None of the effects can be avoided entirely.

V_L is a method utilizing a Laplacian interpolation which basically calculates the zero plane from an area surrounding the QD. In practice, it is found from the z value of several valleys. This is a very sophisticated method, and one major weakness is that it is not possible to control the size of the interpolation area surrounding each QD. It is observed in Fig. 5.14 and 5.15 that V_L gives a smaller deposited volume compared to all other methods. Based on the results, it is likely that interpolation area too small - making the V_L an underestimate. The strength of V_L is that it potentially can solve all of the problems described in local zero plane method above.

There are totally eight distinct methods to estimate the QD volume: $V_{h-mean,0}$, $V_{h,0}$ and $V_{h-max,0}$ that applies a global zero plane and V_{h-mean} , V_h , V_{h-max} , V_{fusion} and V_L using a local zero plane. The methods can furthermore be divided into three branches: mean value method (V_{h-mean} , $V_{h-mean,0}$ and V_L), triangle method (V_{h-max} , $V_{h-max,0}$ and V_{fusion}) and box method (V_h and $V_{h,0}$). There is a good overlap between the three methods V_h , V_{h-mean} and V_{h-max} , as seen in Fig. 5.14 and 5.15. A general trend seen in Fig. 5.14 and 5.15 is that V_{h-max} deviates slightly more from V_h than for V_{h-mean} . This is probably because V_{h-max} is a much more rough approximation than V_h and V_{h-mean} , namely a conical approximation. Similarly, there is a good overlap between $V_{h,0}$ and $V_{h-max,0}$ - but

$V_{h-max,0}$ deviates more than from $V_{h,0}$ than V_{h-max} deviate from V_h .

The *surface area method* (V_h) is expected to be the most accurate and realistic approximation using AFM data. Hence it takes the curvature of the QD into account, by estimating the real surface of the QDs. It is important to emphasise that the real surface is estimated by small half-triangles - so it is not an exact model of the QD topography (see Sec. 4.3.1). V_{fusion} is also anticipated to be one of the best approximation methods. The method uses QD diameter and density from SEM, and height from AFM. AFM is known to measure diameter inaccurately, documented in several studies. [37] A great variation in projected QD area was seen in Fig. 5.9. Therefore, a major source of error could be eliminated by not using the projected QD area from AFM data. The author concludes, considering all the pros and cons of the estimation methods above, that the *surface area method* (V_h) and the hybrid SEM/AFM method (V_{fusion}) are the most suitable methods for predicting the total QD volume.

What resolution?

Total QD volume was independently estimated from both $500\text{ nm} \times 500\text{ nm}$ (Fig. 5.15) and $1\text{ }\mu\text{m} \times 1\text{ }\mu\text{m}$ (Fig. 5.15) AFM images. One strength of using the $1\text{ }\mu\text{m} \times 1\text{ }\mu\text{m}$ AFM images, is that the number of QDs on average is four times larger than images of resolution $500\text{ nm} \times 500\text{ nm}$. However, it is quite possible that the QDs from three separate locations of $500\text{ nm} \times 500\text{ nm}$ AFM images corresponds to a representative QD population for that given sample piece. The population size for sample *514-2* is at least 600 QDs for $500\text{ nm} \times 500\text{ nm}$ and 2400 grains for $1\text{ }\mu\text{m} \times 1\text{ }\mu\text{m}$ AFM images. Samples with higher QD density than *514-2* have correspondingly larger population sizes, as there is a linear relationship between sample sizes and QD densities. The amount of data was huge for all samples, including over 10 000 QDs in for samples such as *503-1* and *544-1*. All results were based on AFM images from at least three locations, each separated by a few millimetres. More deviation between the single locations had been expected if the sample size had been to small. Even few hundred QDs gave a fairly good prediction of mean values and variance for the entire sample.

Volume is a function of QD height, size and shape. Are the QD height, size and shape measured more accurately in $500\text{ nm} \times 500\text{ nm}$ AFM images? Firstly, it is easier for the tip to resolve closely bounded grains with a higher resolution. The resolution was 512 px per line for both $500\text{ nm} \times 500\text{ nm}$ and $1\text{ }\mu\text{m} \times 1\text{ }\mu\text{m}$ AFM images. Effectively, this means that the resolution is two times greater per area for $500\text{ nm} \times 500\text{ nm}$ AFM images - or two times more raw data per area. Computational algorithms were in most cases employed to recognize grain boundaries. More raw data per area could result in more defined grains, hence, better estimates. Secondly, it is much easier to mask grains in $500\text{ nm} \times 500\text{ nm}$ than $1\text{ }\mu\text{m} \times 1\text{ }\mu\text{m}$ AFM images. The argument is simply that the QDs are four times bigger at the same magnification, which makes the boundary of the grains more visible and defined. Therefore, uncertainties in masking are expected to be larger for $1\text{ }\mu\text{m} \times 1\text{ }\mu\text{m}$ AFM

images.

Data from $1\ \mu\text{m} \times 1\ \mu\text{m}$ AFM images are less accurate, especially for the samples with very high QD density such as *503-1*, *503-2* and *544-1*. This conclusion is partly based on previous experience with similar samples. [37] Additionally, extra AFM images were added to low-density samples, such as *514-2* and *514-4*, to increase the sample size even more. It is the author's point of view that $500\ \text{nm} \times 500\ \text{nm}$ AFM images are to be preferred as long as the QD density is relatively high.

5.5.5 Comparison of samples

Under the assumption that V_{fusion} and V_h are the most accurate methods, and $500\ \text{nm} \times 500\ \text{nm}$ the optimal scan size, the tendencies found in Fig. 5.14 can be summarized as follows:

- ◇ *514-2*, *514-4* and *544-1* have approximately the same total QD volume. *544-1* has possibly a greater volume than *514-2*.
- ◇ *503-2* and *504-1* have larger total QD volume than *514-2*, *514-4* and *544-1*.
- ◇ *504-1* has a larger volume than *503-2*.
- ◇ It is suggested that *503-1* (V_{fusion}) or *514-2* / *514-4* (V_h) has the lowest estimated QD volume.
- ◇ *503-1* has the same or smaller volume than *503-2* and *504-1*. V_h suggests the same, although V_{fusion} seems to imply a smaller volume.

In this study, exploring possibilities using AFM was the main objective. V_h is judged to be the best AFM method, whereas the hybrid SEM / AFM method could be used when SEM data is available. However, the SEM data used in V_{fusion} was not acquired in this study. As a result, V_h was chosen to be the primary volume estimation method for the rest of this study.

Growth parameters and V_h

The samples in this study can be divided two series. *Series I* has increasing deposited InAs thickness, constant growth temperature ($480^\circ\ \text{C}$) and contains sample *514-4* (1.9 ML), *514-2* (2.1 ML) and *503-2* (2.3 ML). *Series II*, including sample *544-1* ($455^\circ\ \text{C}$), *503-1* ($475^\circ\ \text{C}$), *503-2* ($480^\circ\ \text{C}$) and *504-1* ($490^\circ\ \text{C}$), has increasing growth temperature and the same deposited InAs thickness (2.3 ML). *Nominal values* of deposited InAs thickness and growth temperature for all samples are found in Table 3.1. Fig. 5.22 shows estimated volume from *surface area method* (V_h) plotted for *Series I* (a) and *Series II* (b). The estimated volume V_h increases as the deposited InAs thickness is incremented from 1.9 ML, 2.1 ML to 2.3 ML. Similarly, increments in growth temperature result in a increasing estimated volume V_h . This correlation seems linear.

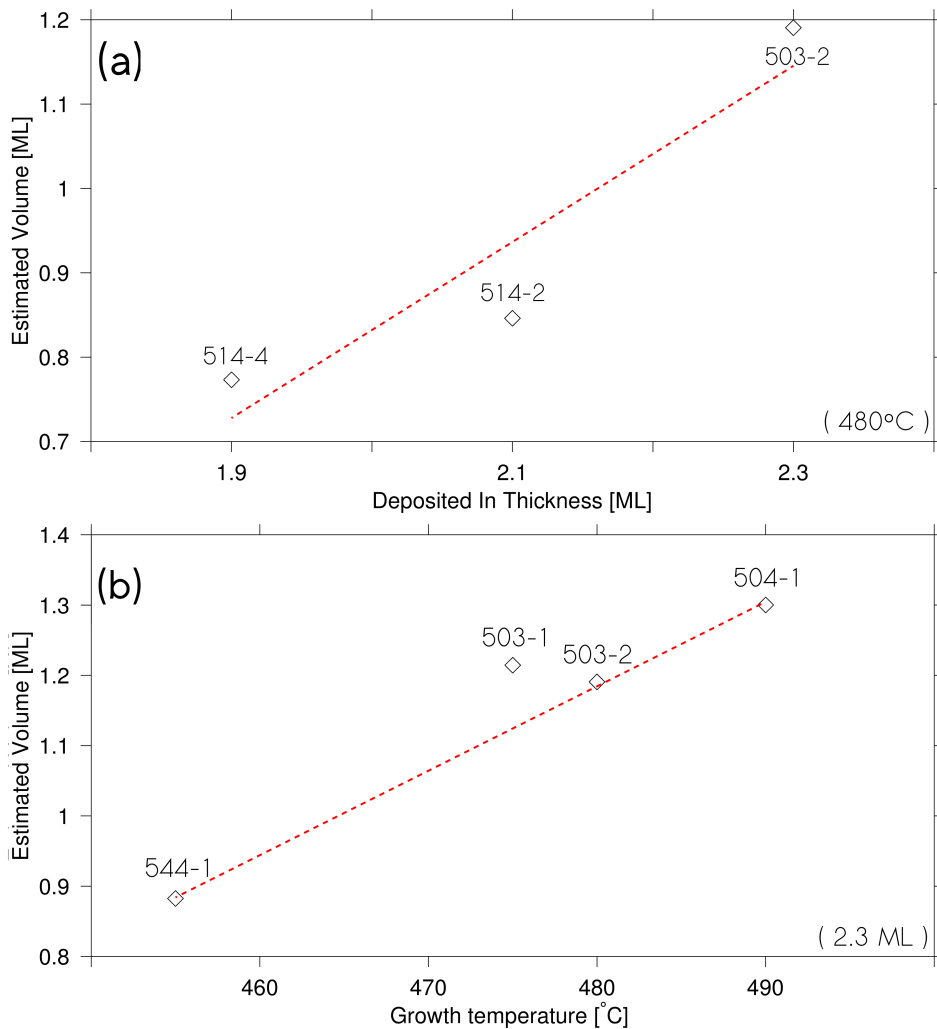


Fig. 5.22: Estimated total QD volume from V_h versus (a) deposited InAs thickness, Θ_{InAs} (*Series I*) and (b) growth temperature, T_{QD} (*Series II*). The red, dashed lines are linear regressions, excluding the outliers (*514-2* and *503-1*). The estimates are from $500 \text{ nm} \times 500 \text{ nm}$ AFM images only (Fig. 5.14).

Let us assume that the linear fits in Fig. 5.22 are correct. The deviation from the linear model can be explained by a deviation between nominal and real growth parameters. As an example, *503-1* in Fig. 5.22 (b) will move vertically down towards the linear fit as the real InAs thickness becomes closer to 2.1 ML. Similarly, *514-2* move upwards if the real growth temperature is greater than 480°C .

Estimated QD volume and deposited InAs during growth

Another aspect with the absolute QD volumes estimated in this study, is that the absolute volumes are significantly smaller than the amount of InAs deposited during growth. This were seen for all $(500 \text{ nm})^2$ estimates, and all estimation methods using *local zero plane*. A couple of the $(1000 \text{ nm})^2$ estimates based on *global zero plane* suggest otherwise (see Fig. 5.15), but as the methods are not reliable - as previously discussed. The estimated QD volume is about under half of the deposited InAs, as seen in *Series I* - Fig. 5.22. One explanation could be the low measured QD height. The low QD height is not likely to be a result of image processing, but could be a product of mechanisms such as oxidation - as explained in Sec. 5.4.

Compared to previous studies

Fig. 5.23 presents the results from the *surface area method* (V_h) compared to a previous study, where all samples except *544-1* were investigated. [41] The previous study gave some unexpected results, and it was therefore decided to re-measure these samples in this master thesis work. Table 5.6 shows numerical values of the volume estimates for all three studies. Volume estimates from the previous study are denoted by $V_{x,T}$ and $V_{x,\Theta_{InAs}}$, as indicated in Fig. 5.23. The comparison of the studies were divided into two series, analogously to previous sections. *Series I*, in Fig. 5.23 (a), demonstrates a linear trend for both V_h and $V_{x,\Theta_{InAs}}$, and strongly correlated estimates (0.99). The strong correlation can be seen in Fig. 5.23 (a), where *514-4* and *503-2* are above the linear fit, and *514-2* is below - deviating most from linear fit. Both $V_{x,\Theta_{InAs}}$ and V_h seem to imply a linear increase in estimated volume, as the amount of deposited InAs during growth (Θ_{InAs}) becomes larger. The volume estimates of $V_{x,\Theta_{InAs}}$ are about 0.3-0.4 ML larger than V_h , as seen in Table 5.6. However, the absolute volume estimates are smaller than Θ_{InAs} for both $V_{x,\Theta_{InAs}}$ and V_h .

Table 5.6: Volume estimates from this master work (V_h) and the previous study of the same samples ($V_{x,T}$ and $V_{x,\Theta_{InAs}}$).

Sample	V_h (nm)	$V_{x,T}$ (nm)	$V_{x,\Theta_{InAs}}$ (nm)
503-1	1.21	1.29	n/a
503-2	1.19	1.61	1.61
504-1	1.30	2.88	n/a
514-2	0.85	n/a	1.10
514-4	0.77	n/a	1.13
544-1	0.88	n/a	n/a

The volume estimates (V_h and $V_{x,T}$) deviated much in Fig. 5.23 (b). It has been suggested in this study, that estimated volume (V_h) increases as a function of growth temperature (T_{QD}). An increasing trend was found for $V_{x,T}$, but it seemed non-linear. The numerical values of $V_{x,T}$ were fitted by exponential regression. The deviation between V_h and $V_{x,T}$ is very small for sample *503-1*, but increases drastically for *503-2* and *504-1*. Fig. 5.12 could explain the divergence between V_h

and $V_{x,T}$, for *Series II*. A significant increase in QD height, would most certainly affect the QD volume. Little difference in QD height was seen between sample *503-1*, *503-2* and *504-1*, in this master work. The QD height in this master work was significantly lower for sample *504-1*, probably explaining the lower QD volume. Consequently, the low QD volume for V_h in *504-1* could be a result of *oxidation*. The height distributions for *503-1* and *503-2* were not so different for Fig. 5.12. Different volume estimation methods and uncertainties in measurements could account for some of the deviations seen in Fig. 5.23 (b), but *oxidation* probably explains the divergence in *series II*.

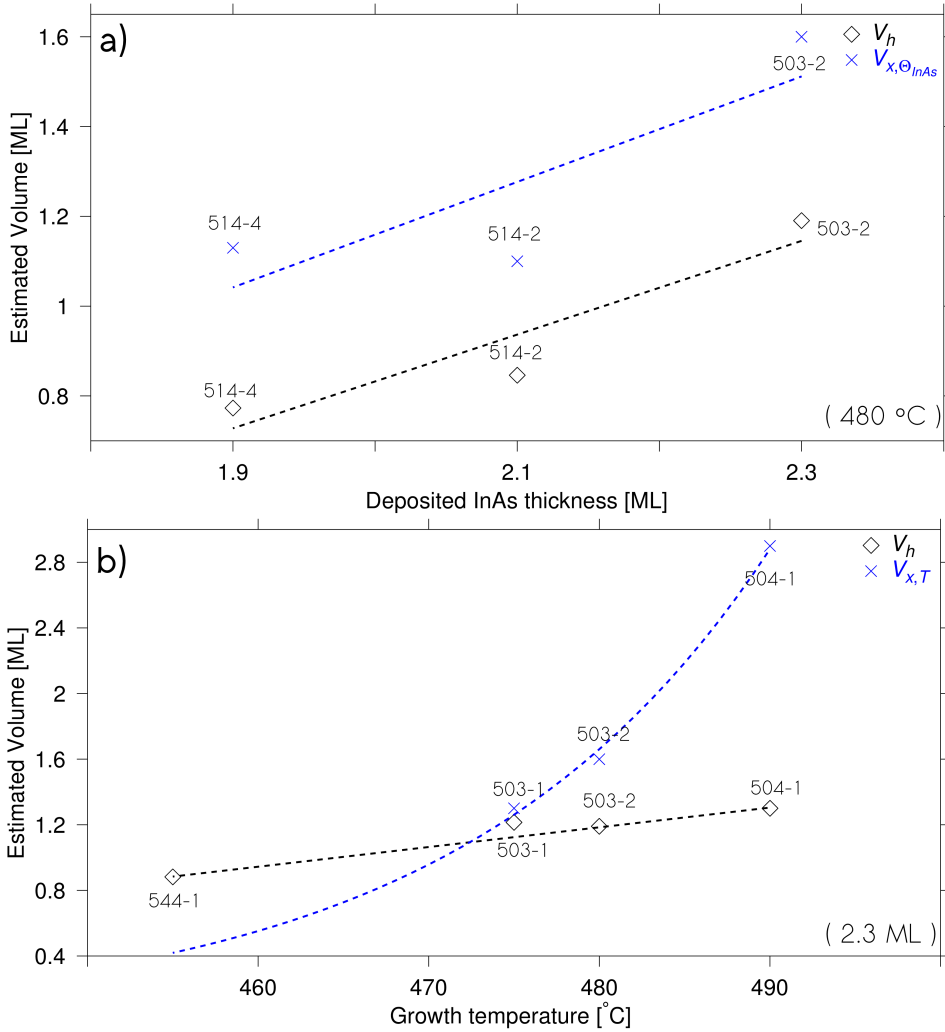


Fig. 5.23: Estimated total QD volume from *surface area method* (V_h) and a previous study on the same samples ($V_{x,\Theta_{InAs}}$ and $V_{x,T}$) [41] (a) deposited InAs thickness, Θ_{InAs} (*Series I*) and (b) growth temperature, T_{QD} (*Series II*). The curves are fitted by linear and exponential regression.

Tip deconvolution was not performed for the previous results. Lack of deconvolution can explain the unexpected non-linear increase in QD volume with T_{QD} , if 503-1 and 503-2 were imaged with a blunt tip and 504-1 with a sharp. This information is not available at the moment of writing this thesis.

5.6 AFM images of the wetting layer

AFM images of the *wetting layer* were made in order to see the background in the AFM images, to possibly locate the terraces on the *wetting layer* (WL) surface. In the rest of this section, these images will be called *wetting layer maps* or *WL maps*. The main motivation of this section is to establish a relationship between terraces and QD growth. One $2\ \mu\text{m} \times 2\ \mu\text{m}$ AFM image from each sample piece is presented in this section. The height scale is **inverted**, going as a gradient from white (0 nm) to black (≥ 2.5 nm). Data deviating more than 2.5 nm from the zero fix plane is represented by black. The AFM images in this section all have the same height scale, contrast level and were processed in the exact same manner.

Fig. 5.24 shows a *WL map* of sample *503-1*. Large regions of continuous grey level can be seen in the background. These regions are likely to be terraces: large, continuous plateaus of constant height. See Sec. 3.1.1. The terraces have varying height relative to each other, seen as various degrees of grey level saturation. The background in sample *503-1* seems have two grey levels. Recall that the height scale is *inverted*, so lighter areas are actually below the more darker. One observation is that the local QD density appears to actually be higher in the darker, higher terraces. Alternatively, it could reflect a higher QD density close to the terrace edge. The QD density is higher in the transition between the light and dark terraces. The local QD density is correspondingly lower in the lighter regions. The QD density seems to be lowest in the interior of the light grey regions.

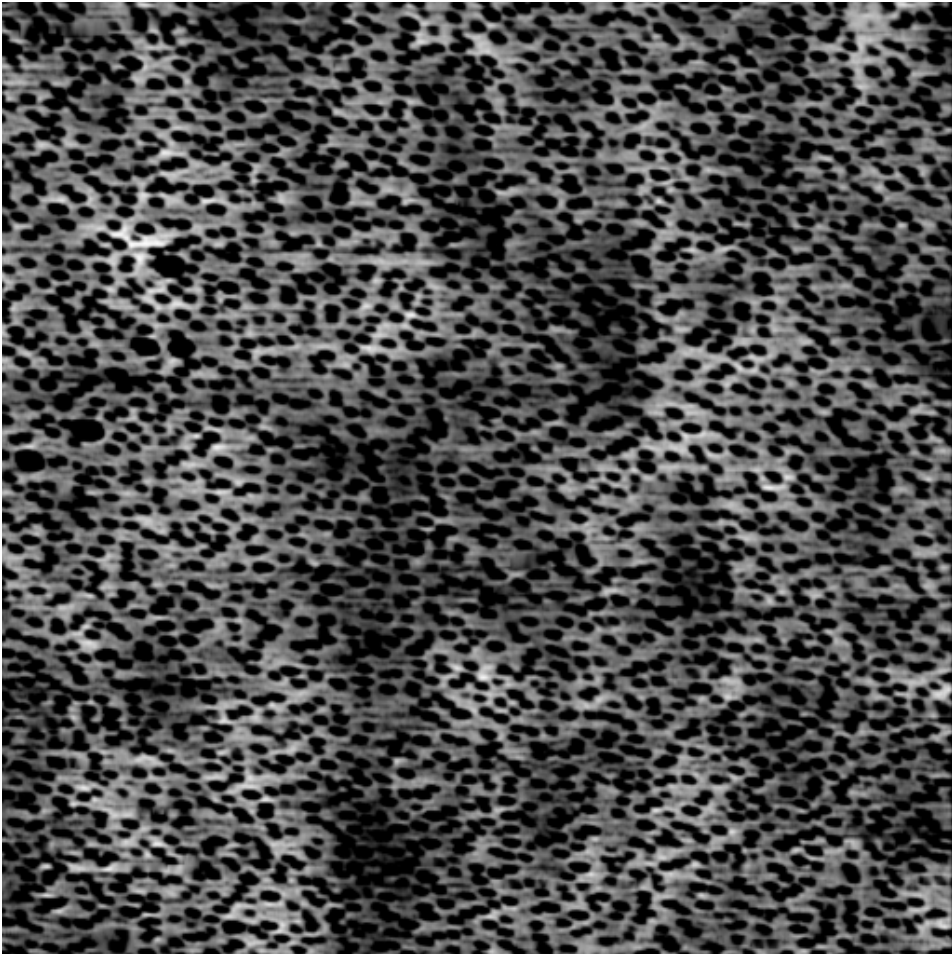


Fig. 5.24: A $2\ \mu\text{m} \times 2\ \mu\text{m}$ *WL map* of sample *503-1*. Grown at 475°C and 2.3 ML deposited.

A $2\ \mu\text{m} \times 2\ \mu\text{m}$ *WL map* of sample *503-2* is presented in Fig. 5.25. There is less variation in grey saturation between the dark and light areas, reflecting a smaller relative height difference. Many of the QDs have grown into continuous clusters. Clustering of QDs is typically found in the darker regions. Clustering is known to be related to a higher QD density, implying that the QDs is more dense in the darker, higher regions. It is not evident from Fig. 5.25 if this accumulation of QDs occurs near edges, or if it is a phenomena related to the darker regions in general.

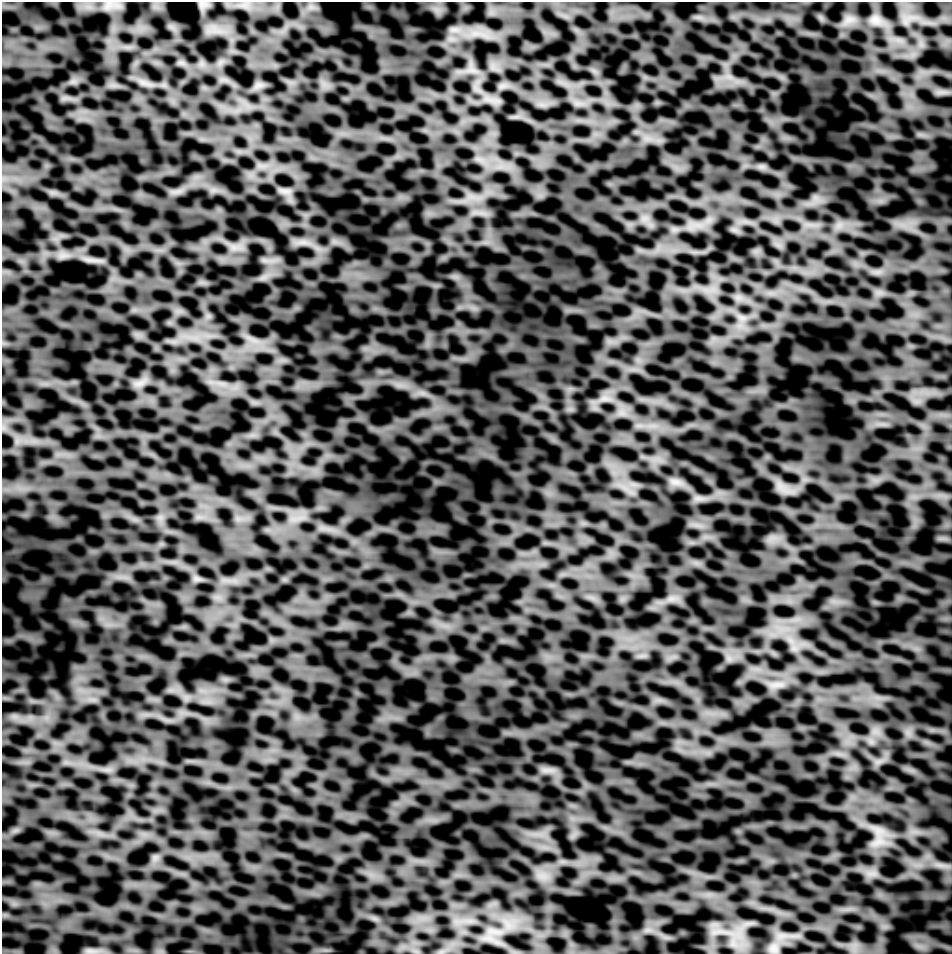


Fig. 5.25: A $2\ \mu\text{m} \times 2\ \mu\text{m}$ *WL map* of sample *503-2*. Grown at 480°C and 2.3 ML deposited.

Fig. 5.26 shows a *WL map* of sample *504-1*. Terraces can be seen in the background. The overall size of each terrace and the variation in background are not very different from sample *503-1*. Sample *504-1* had lower QD density than *503-1* or *503-2*. Local differences in QD density can be observed between the light and dark areas. There is a higher QD density in the dark regions, especially near the transition region between the dark and the light regions. Based on previous observations, it was hypothesised that clustering of QDs takes place at the step edge. Fig. 5.26 is inconclusive, but does not contradict or rule out the possibility of an increased QD density near the step edge. The results are inconclusive because the high-density regions observed Fig. 5.26 could be related to higher 2D *islands* in general, hence not a direct result of step edges.

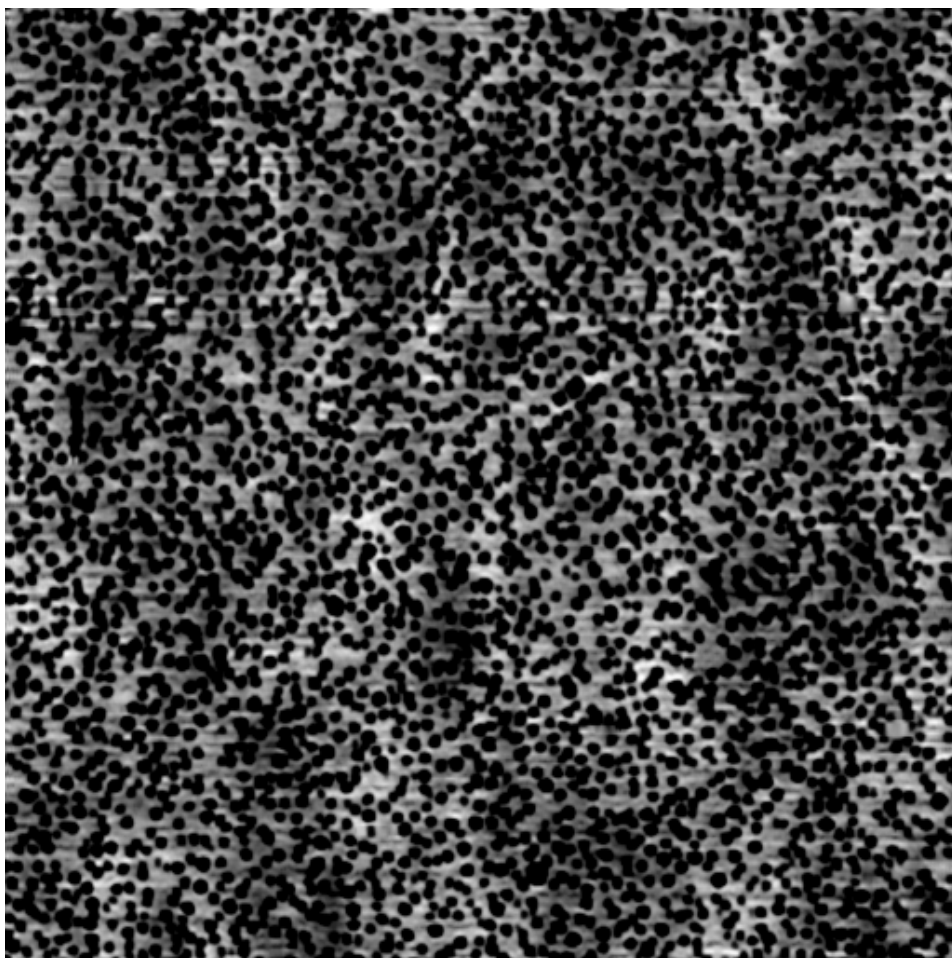


Fig. 5.26: A $2\ \mu\text{m} \times 2\ \mu\text{m}$ *WL map* of sample *504-1*. Grown at 490°C and 2.3 ML deposited.

A *WL map* of sample *514-2* can be seen in Fig. 5.27. Sample *514-2* had lower QD density than all other samples, except for possibly *514-4*. The terraces could be divided into two height levels based on grey saturation: light grey (0.5 nm) and dark grey (1.2 nm). The lighter regions have lower QD density than the higher, darker terraces. Thus, a general tendency of QD clustering on the higher, darker terraces is observable. Fig. 5.27 suggests that there is an accumulation of QDs at the terrace edge, seen at several locations. Another observation, is that the size of the QDs at the step edge look larger than other QDs in the image. For instance, many small and few large QDs are seen in the lighter, lower terraces. In contrast, there are very few small and many large QDs in the dark regions. If this observation reflects a general pattern, and the QD volume is larger at the step edge - it would be a circumferential evidence of step erosion (see Sec 3.1.1).

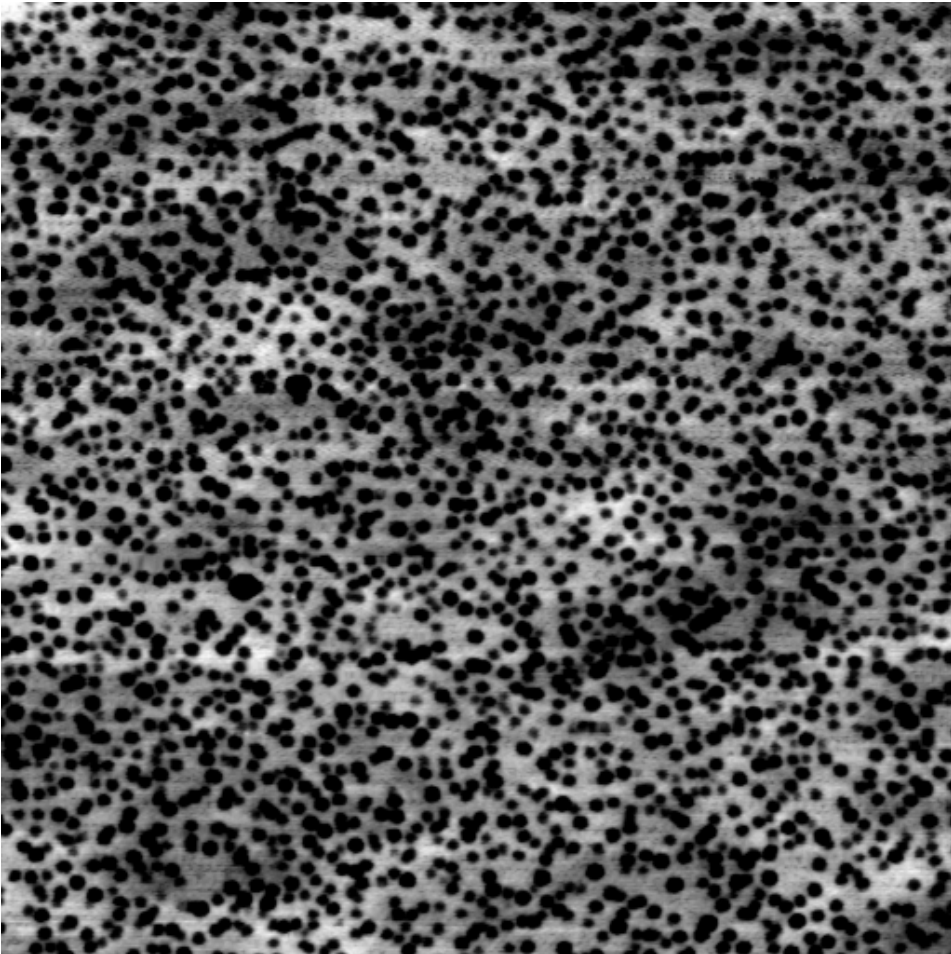


Fig. 5.27: A $2\ \mu\text{m} \times 2\ \mu\text{m}$ *WL map* of sample *514-2*. Grown at 480°C and 2.1 ML deposited.

The background of sample *514-4* is presented by a *WL map* in Fig. 5.28. Three distinct height levels were identified, each separated by at least 0.5 nm. The darkest regions appear like small islands with a much higher QD density relative to the rest of the image. The lowest terrace is almost white and have a much smaller QD density than the two other terraces. The third, intermediate terrace is sandwiched between the dark islands and the white terraces at some places. The intermediate terrace has a lower QD density than the dark islands, and higher or the same QD density as the lowest terrace. A pattern of clustering at the step edge of the dark islands is seen several places in Fig. 5.28. In addition, the size of the QDs on the dark islands seems to be larger than the QDs found in the interior of the lowest terrace.

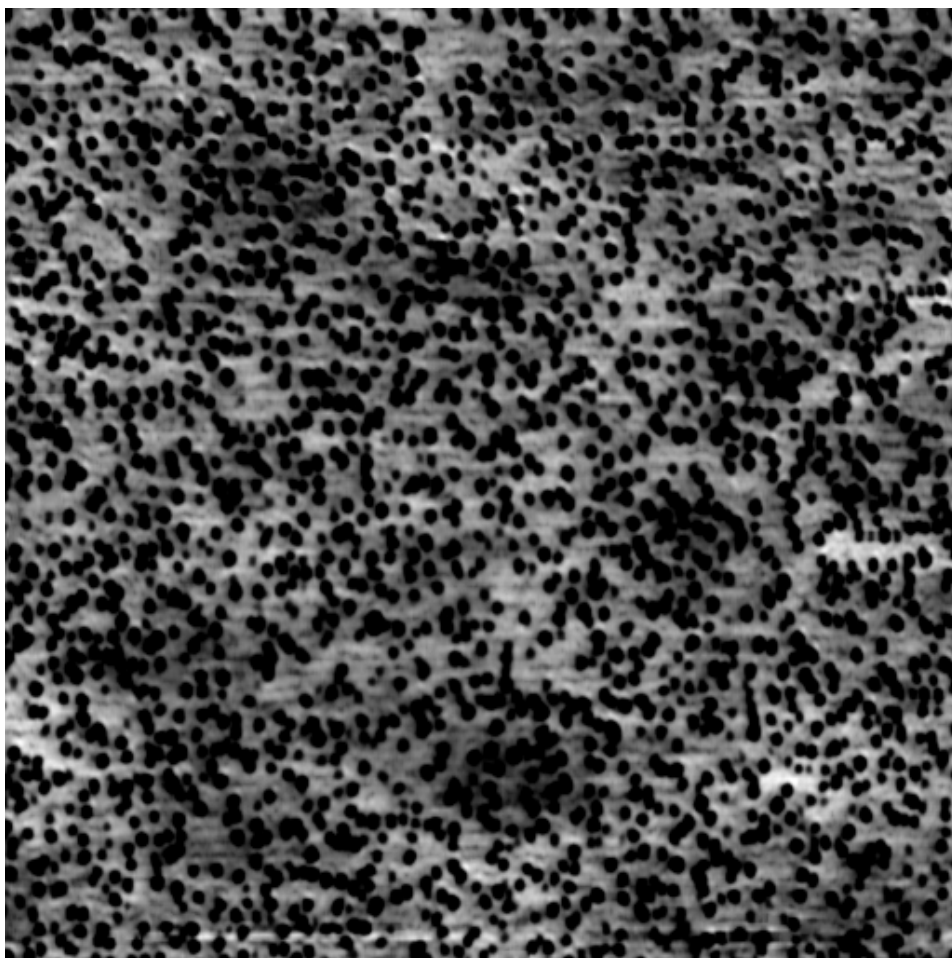


Fig. 5.28: A $2\ \mu\text{m} \times 2\ \mu\text{m}$ *WL map* of sample *514-4*. Grown at 480°C and 1.9 ML deposited.

Fig. 5.29 shows a *WL map* of sample *544-1*. It was very hard to make a good *WL map* of sample *544-1*. *544-1* had very high QD density, and most of the surface was covered by QDs. It was still possible to extract some information of the topography, assuming that the QDs had the same height distribution for all positions in the AFM image. Recall that regions of relatively lower height are more white than darker, higher areas. Changes in mean QD height were observed locally, and could be used as an indicator - supporting the existence of terraces in sample *544-1*. Accordingly, local variations in QD density are visible in Fig. 5.29. The dark regions seem to have a higher degree of QD clustering, and therefore a higher QD density.

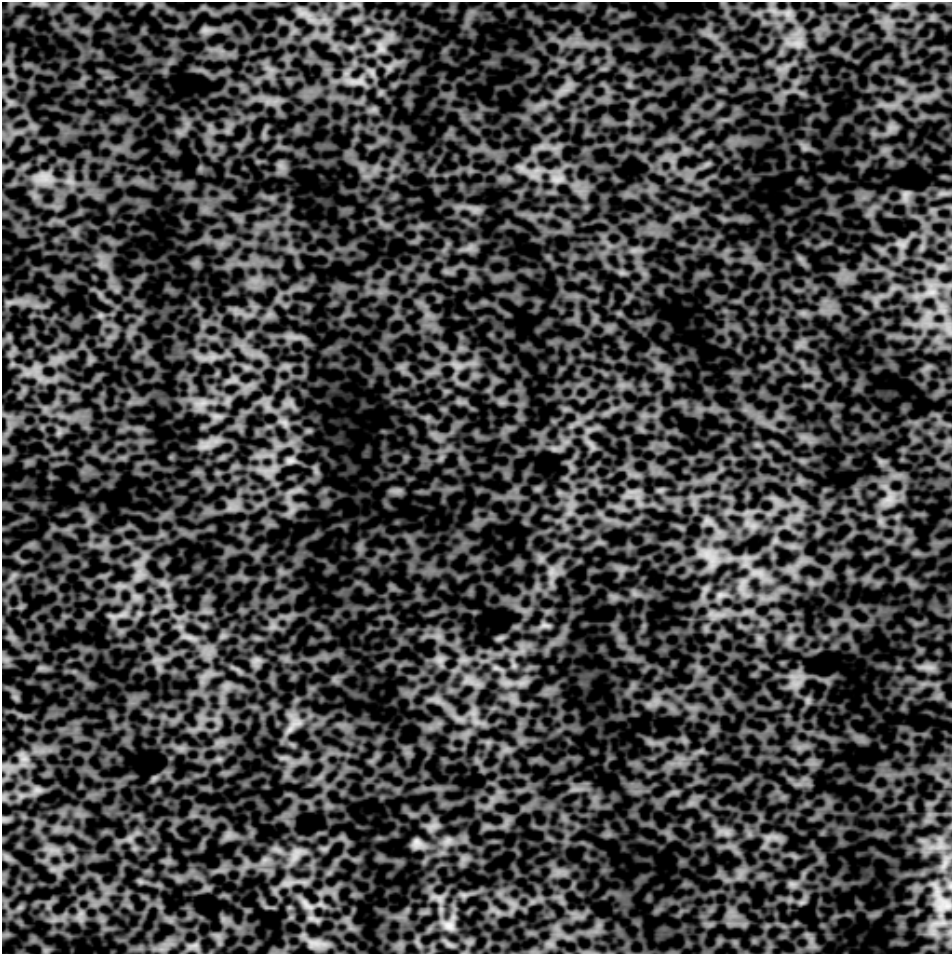


Fig. 5.29: A $2\ \mu\text{m} \times 2\ \mu\text{m}$ *WL map* of sample 544-1. Grown at 455°C and 2.1 ML deposited.

5.6.1 Discussion: terraces and growth of QDs

In this section we have found some qualitative observations suggesting a certain relationship between terraces and growth of QDs. In several of the *WL maps* in the section above, QDs tended to cluster near the steps of the terraces. However, the observations in this study were inconclusive and more hard evidence is needed in order to strengthen the hypothesis.

The terraces observed in the *WL maps* of the previous section are believed to be 2D islands. In some studies [32], it has been concluded that the erosion happens for QDs nucleated over the step edge. Nucleation of QDs seems more common near the step edges. The hypothesis could be falsified due to a finite tip resolution. Also, the *WL maps* suggested larger QDs near the step edges compared to the interior

of the islands - a possible indication of step erosion. This was most apparent in Fig. 5.27 and 5.28.

5.7 Imaging of defects

In 2010, *Gradkowski et al* demonstrated how the defect density on a sample surface could be monitored by AFM. [43] The samples contained a single QD layer capped with a 300 nm thick spacer, and had no QDs on the top surface. *Transmission Electron Microscopy* (TEM) images revealed that the defects seen in AFM images were correlated to stacking faults, emerging from anomalous large QDs buried under the thick GaAs spacer layer. One TEM image is shown in Fig. 5.30 (b), which suggests that the defects are associated with abnormally large QDs. The origin of the *square defects* is illustrated in Fig. 5.30 (c). The size of the *defects* seen in the TEM images below are comparable to defects observed in corresponding AFM studies.

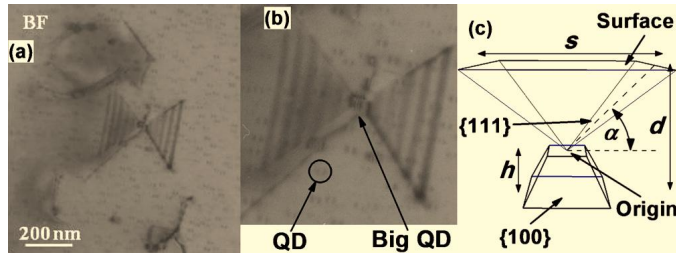


Fig. 5.30: (a) A $2\ \mu\text{m} \times 2\ \mu\text{m}$ bright field TEM micrograph of the sample structure, (b) a large buried QD depicted as a source for the defect and (c) the formation of the square defect shown schematically. [43]

Fig. 5.31 from [43] contains a representative $10\ \mu\text{m} \times 10\ \mu\text{m}$ AFM image showing the *square defects*. General bunching of atomic steps is visible in the background of the surface structure. Fig. 5.31 (b) shows a close-up look on the *square defect*. According to [43], the size of the *square defects* are around $440\ \text{nm} \times 440\ \text{nm}$.

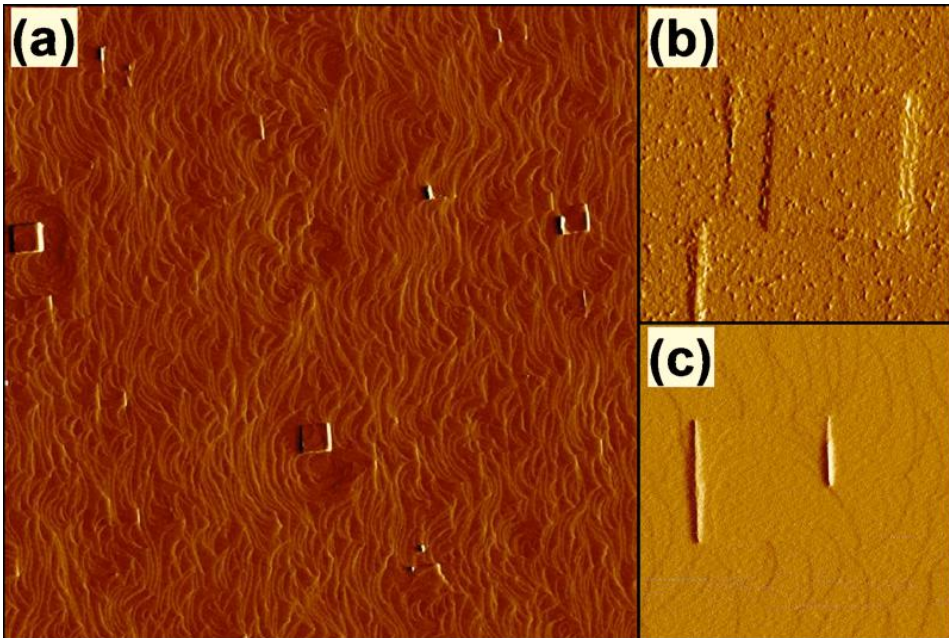


Fig. 5.31: (a) a $10\ \mu\text{m} \times 10\ \mu\text{m}$ AFM image reveal several square defects. (b) zoomed-in. [43]

The *QD-IBSC* group decided to test the method of *Gradkowski et al* on our samples. $10\ \mu\text{m} \times 10\ \mu\text{m}$ AFM images of our samples are presented below. All AFM images have increased contrast, which means that the height difference between the various grey scales is smaller than in a typical raw AFM image. The height scale goes as a gradient from 0 nm (black) to 7.5 nm (white) for all AFM images. The images have resolution $1024\text{px} \times 1024\text{px}$, except for *514-4* that has higher resolution.

5.7.1 Sample *503-1*

Fig. 5.32 is a $10\ \mu\text{m} \times 10\ \mu\text{m}$ AFM image of sample *503-1*. Dark square-shaped areas surrounding large QDs can be observed in Fig. 5.32. These areas are lower relative to the "lighter" areas surrounding the squares. The grey shade of the dark areas inside each square are similar, the mean height is about the same inside all squares. Let the dark squares seen in Fig. 5.32 be denoted by *square defects* in the rest of this work. The horizontal scars visible in Fig. 5.32 are a scanning artefact, likely to be caused by a too high deflection point. The large QDs are inhomogeneously distributed, some regions have fewer large QDs than the rest of the image. Some of the *square defects* overlap. None of the *square defects* are perfectly parallel, but the angle of the corner sides is close to 90° .

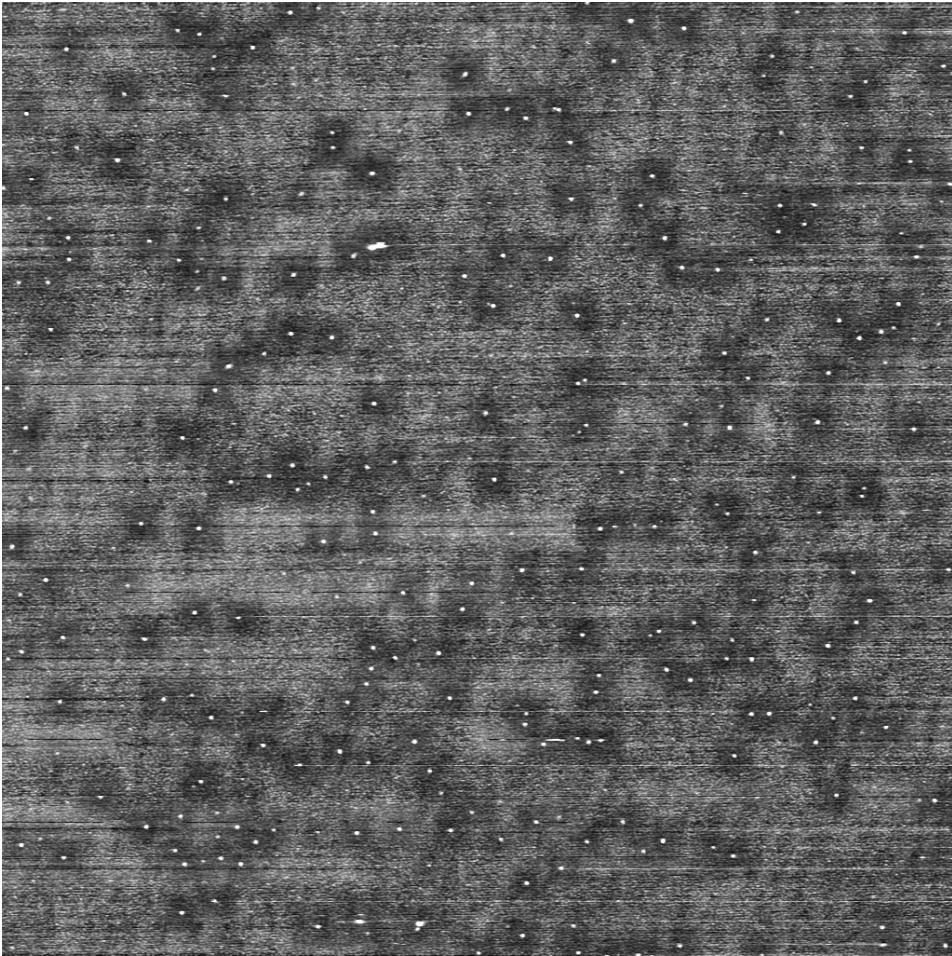


Fig. 5.32: A high contrast $10\ \mu\text{m} \times 10\ \mu\text{m}$ AFM image of sample *503-1*.

5.7.2 Sample *503-2*

Fig. 5.33 shows a $10\ \mu\text{m} \times 10\ \mu\text{m}$ AFM image of *503-2*. *Square defects*, analogously to those seen in Fig. 5.32, is visible in Fig. 5.33. It is clear that there is some variation in *square defects* size, and there are deviations from the square shape. The background in sample *503-2* is darker with some lighter areas, especially near the left half of the image. The dark background results in a smaller contrast difference between the *square defects* and the surrounding regions. In practice, it means that the plateaux amplitude or mean depth inside a *square defect* is smaller relative to *503-1*. Sample *503-2* had a lower density of *square defect* than *503-1*.

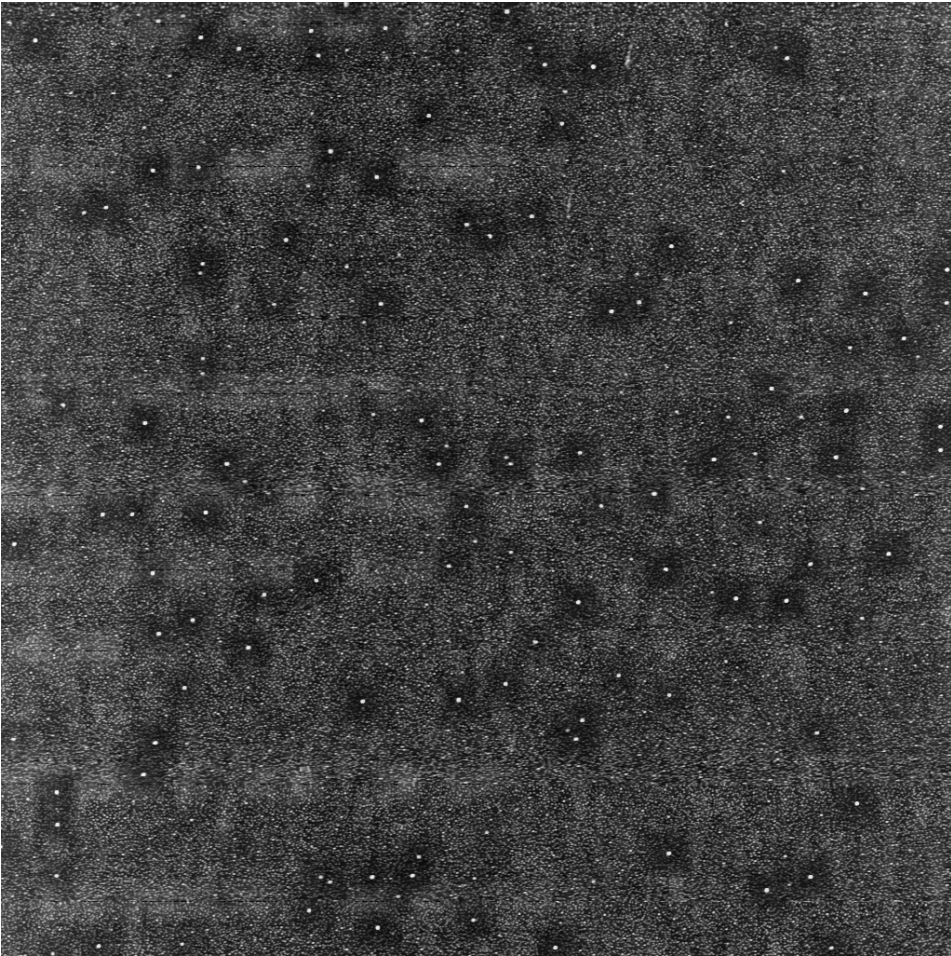


Fig. 5.33: A high contrast $10\ \mu\text{m} \times 10\ \mu\text{m}$ AFM image of sample *503-2*.

5.7.3 Sample *504-1*

A $10\ \mu\text{m} \times 10\ \mu\text{m}$ AFM image of sample *504-1* is shown in Fig. 5.34. Sample *504-1* had the highest growth temperature of all samples. The *square defect* are not so dark in Fig. 5.34, meaning that the plateaux amplitude within a *square defect* is very close to zero. There are two parallel, diagonal scars across the Fig. 5.34, and one horizontal scar in the upper-left region of the image. It is hard to guess the origin of these scars, but it might be a damage to the surface that occurred prior growth. Similar scars were found in four different locations on sample *504-1*.

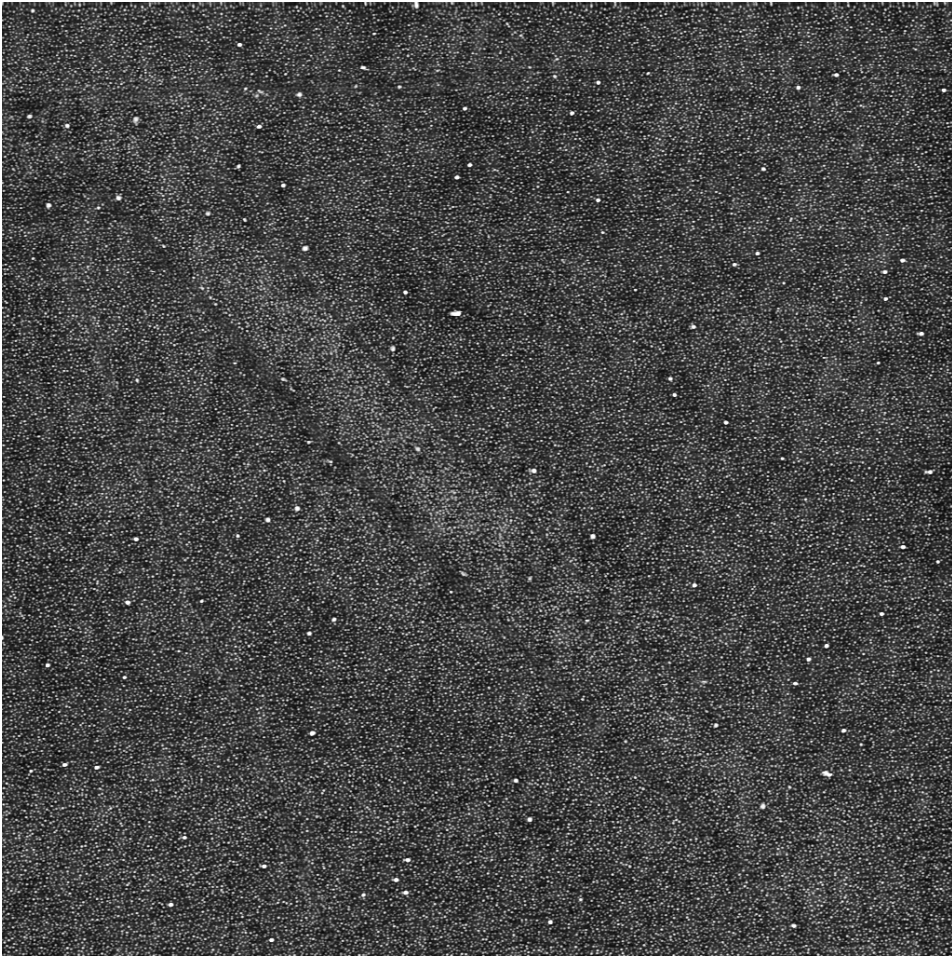


Fig. 5.34: A high contrast $10\ \mu\text{m} \times 10\ \mu\text{m}$ AFM image of sample *504-1*.

5.7.4 Sample *514-2*

Fig. 5.35 is a $10\ \mu\text{m} \times 10\ \mu\text{m}$ AFM image of *514-2*. The density of *square defects* is much lower in Fig. 5.35 than in Fig. 5.32, 5.33 and 5.34. The plateaux amplitude of the *square defects* in Fig. 5.35 is, in contrast to Fig. 5.34, very large. The QDs are very smooth compared to the other samples covered so far in this section. Some large QDs can occasionally be seen among the smaller QDs. The uppermost part of the image looks dragged in the vertical direction, and is a scanning artefact.

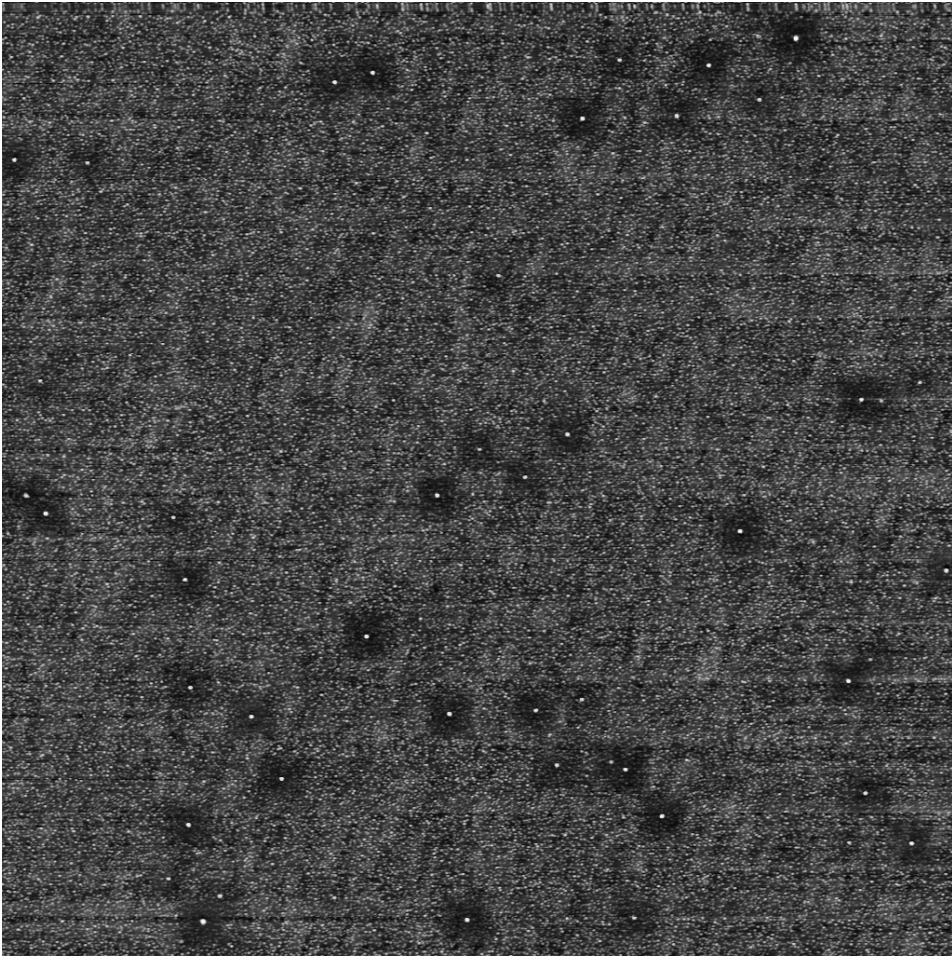


Fig. 5.35: A high contrast $10\ \mu\text{m} \times 10\ \mu\text{m}$ AFM image of sample *514-2*.

5.7.5 Sample *514-4*

Fig. 5.36 is a very high resolution AFM image of sample *514-4*. The QDs are homogeneously distributed with a nearly constant QD density in all regions of Fig. 5.36. The QDs are easier to resolve in this image compared to higher density AFM images like Fig. 5.32 or 5.33, because the diameter is larger and the density lower. There is a darker spot in the upper-left corner of the image, showing that there are topographically changes in the background. Sample *514-4* was the only sample with very few defects or large QDs. Few clear defects were observed in any of the AFM images for sample *514-4*. The only abnormal surface features are four large QDs, visible in Fig. 5.36. The large QDs are apparently not allocated to square defects. It is possible that the plateaux amplitude is very, very small; but density of *square defect* is certainly extremely low in sample *514-4*.

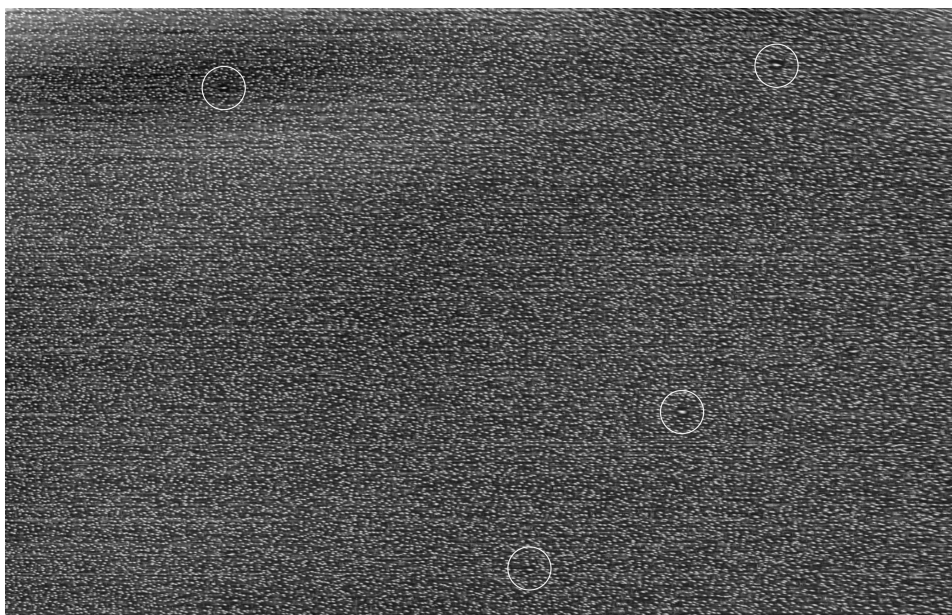


Fig. 5.36: A high contrast $10\ \mu\text{m} \times 10\ \mu\text{m}$ AFM image of sample *514-4* with a very high resolution ($4096\ \text{px} \times 2621\ \text{px}$). The medium-sized QD are marked with white circles.

5.7.6 Sample *544-1*

Fig. 5.37 shows a $10\ \mu\text{m} \times 10\ \mu\text{m}$ AFM image of sample *544-1*. The growth temperature of *544-1* was 455°C (see Table 3.1), lower than in all other samples. Sample *544-1* had the highest QD density of all sample. Evidence of *square defects* in sample *544-1* was first found in Sec. 5.1.6. Fig. 5.37, supports this finding. It is evident from Fig. 5.37, and many other AFM images, that sample *544-1* had the highest density of *square defect* among all samples. In fact, most of the surface is covered by these defects, and many of the defects have grown into each other. The *square defects* vary in size, shape and alignment. It is hard extract details from the regions between dark squares. The grey level seems to change very little, but it is still less homogeneous than samples like *514-2* and *514-4*. A very strange feature, found in several AFM images of sample *544-1* - but not in any other sample, can be seen in the lower part of Fig. 5.37. The feature looks like an mirrored "C".

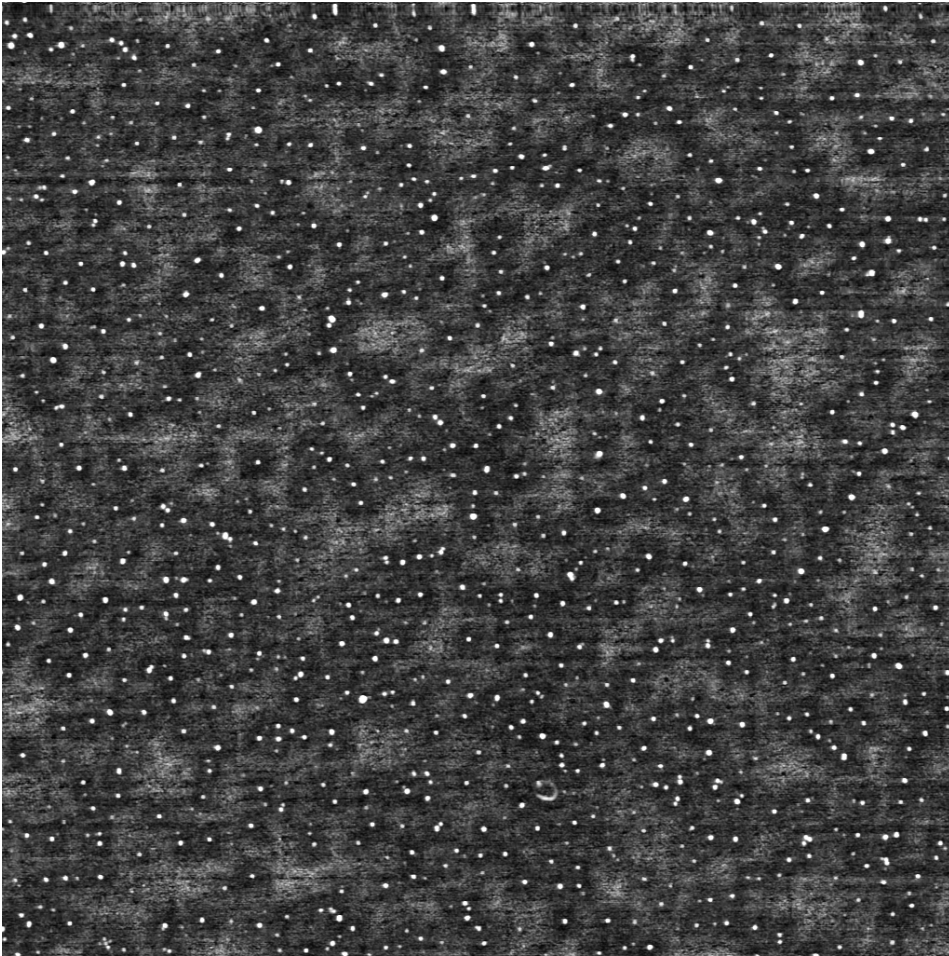


Fig. 5.37: A high contrast $10\ \mu\text{m} \times 10\ \mu\text{m}$ AFM image of sample *544-1*.

5.7.7 Large QDs and Square Defects

Table 5.7 shows characteristics of square defects and large QDs in all six samples. Side length of square defects are given by a . The *Square defects* are very regular and highly symmetric features found in all samples except *514-4*. They have well-defined edges with a size of about a few hundred nanometre, Table 5.7 shows the length of the sides estimated from $10\ \mu\text{m} \times 10\ \mu\text{m}$ AFM images only. *Square defects* are inverted plateaux that are a few nanometres deep, varying from sample to sample. No square defects without a large QD in the centre have been observed, based on an investigation of all $10\ \mu\text{m} \times 10\ \mu\text{m}$ AFM images, from all samples. There could be one or several large QDs in a square defect, in most cases located near the centre of the defect. Two and three large QDs were observed in the centre of a single *square defect* at several locations in Fig. 5.37, and were seen in

other samples as well. Some isolated medium-sized QDs can be found without the associated square defect, mostly seen in Fig. 5.32, 5.33 and 5.36.

Table 5.7: Side length of *square defects* (a), projected area (A_{proj}) and height (\bar{H}) of large QDs were all estimated from 4-5 AFM $10\ \mu\text{m} \times 10\ \mu\text{m}$ AFM images per sample. The side length (a) was determined from manual measurements of about 40 square defects per sample. s_a , $s_{A_{proj}}$ and $s_{\bar{H}}$ are sample standard deviations for a , A_{proj} and \bar{H} , respectively.

Sample	a (nm)	s_a (nm)	A_{proj} (nm^2)	$s_{A_{proj}}$ (nm^2)	\bar{H} (nm)	$s_{\bar{H}}$ (nm)
503-1	407	53	1542	43	8.6	1.1
503-2	367	51	663	16	11.8	0.9
504-1	358	58	775	23	13.6	1.3
514-2	377	101	938	47	12.3	1.3
514-4	n/a	n/a	1269	132	10.6	1.2
544-1	370	69	1104	14	10.0	1.5
Mean	376	69	1048	326	11.1	1.8

Some of the AFM images in Sec. 5.1 might suggest that the side length is varying for different scan sizes. A similar study of *square defects* in $2\ \mu\text{m} \times 2\ \mu\text{m}$ AFM images of sample *544-1* was performed to investigate possible deviations. The side length was never estimated from $1\ \mu\text{m} \times 1\ \mu\text{m}$ AFM images. The data set included only five $2\ \mu\text{m} \times 2\ \mu\text{m}$ AFM images. No significant deviations were proven. The observed difference could be explained by natural variation. The sample variance was high for all samples, including *544-1*, as seen in Table 5.7.

The varying height (\bar{H}) and projected area (A_{proj}) of large QDs are presented in Table 5.7. The only sample that had a significantly higher height (\bar{H}), was sample *504-1*. The height in all other samples were similar. 95% of all large QDs had a height between 7.6 to 14.6 nm, in all samples. In comparison, 95% of small QDs in all samples were between 0.75 nm and 2.26 nm high. Thus, the large QDs are significantly higher than small QDs in all samples.

The large QDs in *503-1*, *514-4* and *544-1* had the highest projected area (A_{proj}). Likewise, *503-2* and *504-1* had the smallest A_{proj} . The mean projected area of $(1048 \pm 659)\ \text{nm}^2$ corresponds to an effective diameter between 24.7 to 41.9 nm. This result was supported by manual measurement in *Gwyddion*, including over 100 large QDs. The projected area for large QDs was found to be significant higher than small QDs for all samples, except for possibly *514-4*. The area was found to be the same for small and large QDs in sample *514-4* for small QD estimates from $1\ \mu\text{m} \times 1\ \mu\text{m}$ AFM images.

The large QD density for all six samples is listed in Table 5.8. The large QD density was estimated from the mean value of at least four different locations, using $10\ \mu\text{m} \times 10\ \mu\text{m}$ AFM images. The motivation to estimate the large QD density was to have a quantitative parameter indicating the density of defects for a given sample, since *Gradkowski et al.* have seen a close relationship between large QDs

and square defects. [43]

Table 5.8: The large QD density ($\rho_{LargeQD}$), sample standard deviation (s_ρ) and relative variance $\Delta\rho_{LargeQD}/\rho_{LargeQD}$ and fraction of large QD per small QD Ψ . The data is estimated from $10\ \mu\text{m} \times 10\ \mu\text{m}$ AFM images from three different locations per sample. QD density from Table 5.1 was used to calculate Ψ .

Sample	$\rho_{LargeQD}$ ($10^8\ \text{cm}^{-2}$)	s_ρ ($10^8\ \text{cm}^{-2}$)	$\Delta\rho_{QD}/\rho_{QD}$ (%)	Ψ (%)
503-1	2.2	0.3	14%	$2.0 \pm 0.6\%$
503-2	1.3	0.1	8%	$1.7 \pm 0.3\%$
504-1	0.9	0.2	22%	$1.6 \pm 0.8\%$
514-2	0.5	0.0	0%	$0.7 \pm 0.1\%$
514-4	0.1	0.1	87%	$0.2 \pm 0.3\%$
544-1	6.0	1.0	17%	$3.4 \pm 1.3\%$
Mean	1.8	0.5	28%	$2.0 \pm 1.2\%$

Fig. 5.38 and Table 5.8 show a great variation in large QD density for the various samples, not surprisingly highest large QD density for *544-1*. The number of large QDs per 1000 small QDs, Ψ , reflects the *defect density*. Single large QDs, not associated with *square defects*, was observed in all samples. This was quite common in sample *514-4*. The *defect density*, Ψ , was smallest for *514-4*, and a bit larger in *514-2*. *503-2* was significantly larger than *514-2*. The fraction of large QDs per small QD was about the same for *503-1*, *503-2* and *504-1*. Sample *503-1* and *544-1* had largest Ψ , thus, highest *defect density* of all samples.

Large QD density, *defect density* and growth parameters

The large QD density ($\rho_{LargeQD}$) and *defect density* (Ψ) are plotted for two series in Fig. 5.38 and 5.39. *Series I* (a) has increasing amount of deposited InAs thickness and the same growth temperature (480°C), whereas *Series II* (b) has varying growth temperature and fixed amount of deposited InAs during growth (2.3 ML). A linear regression of the the data series are shown as red, dashed lines. Both plots of *Series I* (a) in Fig. 5.38 and 5.39, seem to suggest that the large QD density and Ψ increase as the amount of deposited InAs becomes larger. This increase is significant for both large QD densities and Ψ . Similarly, large QD densities and Ψ decrease for each increment in growth temperature for *Series II* (b). The decrease is not significant, but *544-1* has a larger $\rho_{LargeQD}$ than the other samples in Fig. 5.38 (b).

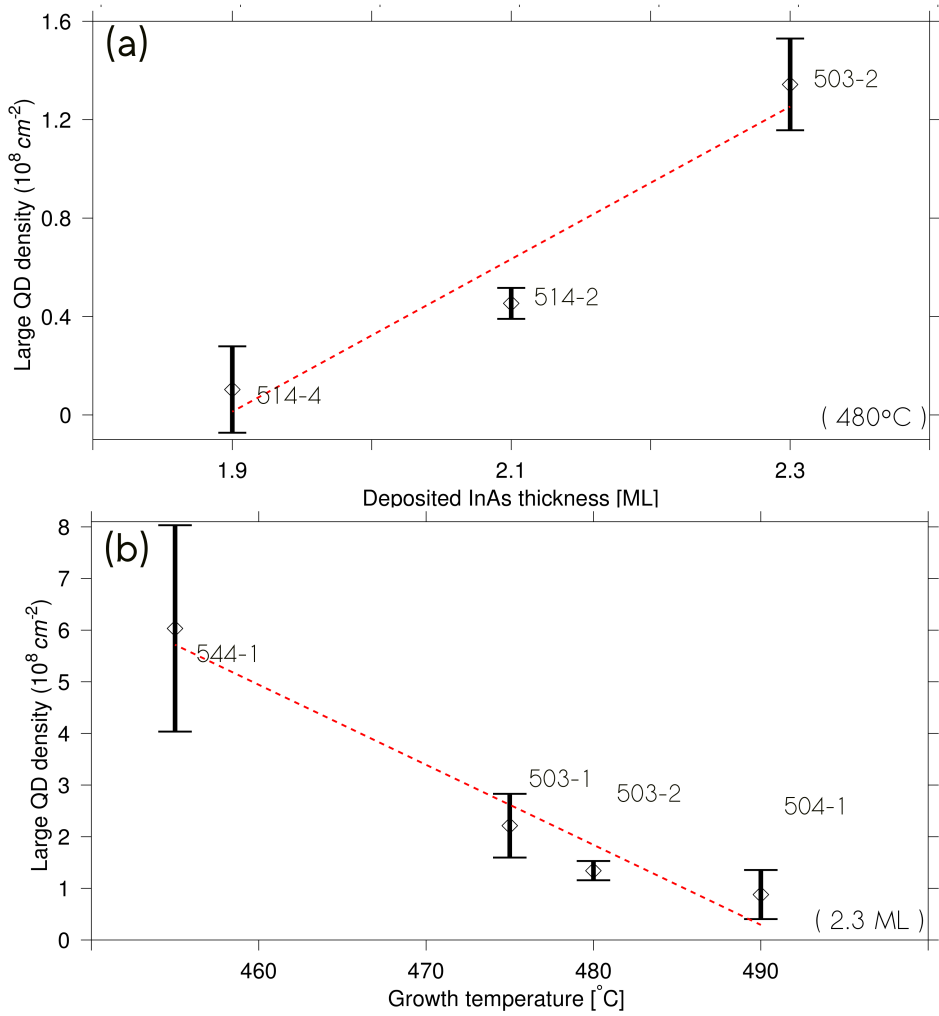


Fig. 5.38: The large QD density with error bars versus (a) deposited InAs thickness, Θ_{InAs} (*Series I*) and (b) growth temperature, T_{QD} (*Series II*). The red, dashed lines are linear regressions. The data was estimated from $10 \mu\text{m} \times 10 \mu\text{m}$ AFM images, mean value of four different locations per sample.

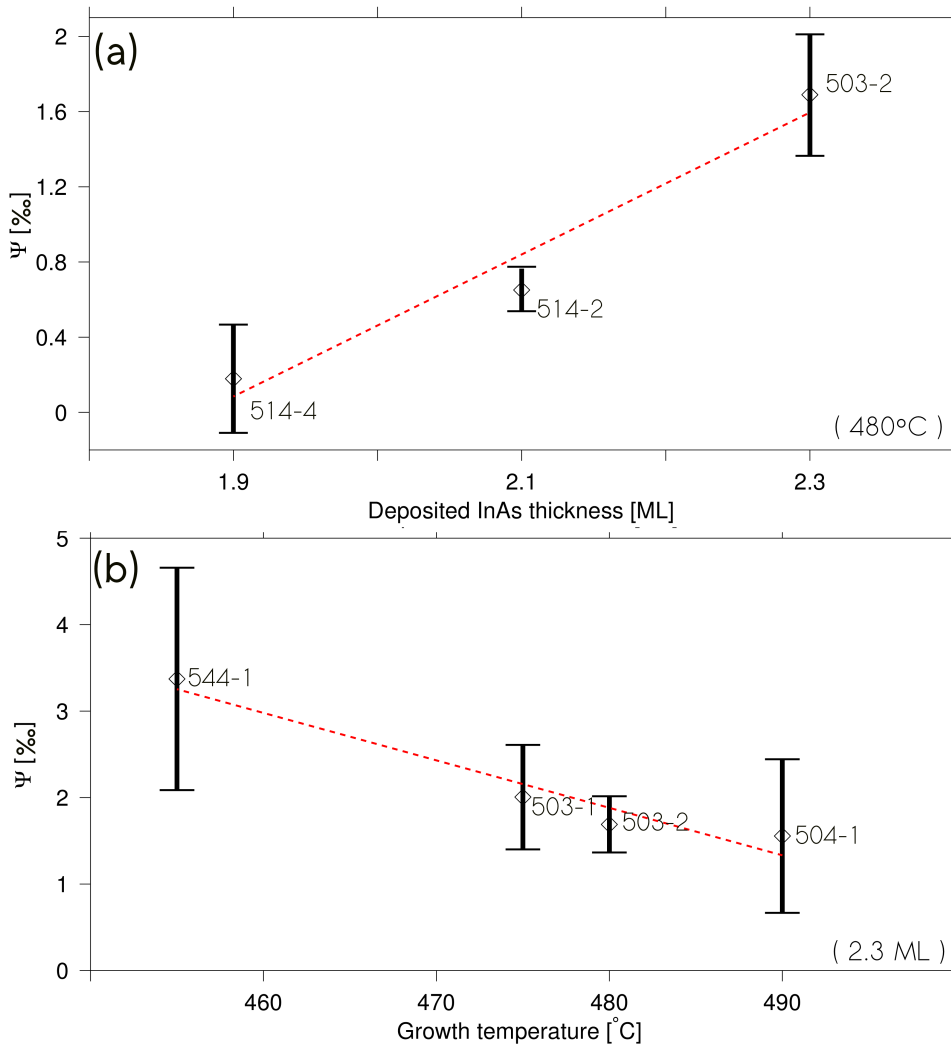


Fig. 5.39: Defect density with error bars versus (a) deposited InAs thickness, Θ_{InAs} (*Series I*) and (b) growth temperature, T_{QD} (*Series II*). The red, dashed lines are linear regressions. The data was estimated from $10 \mu\text{m} \times 10 \mu\text{m}$ AFM images, mean value of four different locations per sample.

5.7.8 Discussion: Large QDs and Square Defects

What are large QDs ? The observed circumstances could be understood in two ways. The most probable is that large QDs simply are gargantuan QDs - with greater volume and diameter than ordinary, small QDs. Several studies [44] support this explanation. An alternative explanation is that large QDs are clusters of several QDs merged together in one cluster. It has been observed in previous studies [37] that clusters of QDs occasionally can be recognized as one large QD. This happens if the AFM tip is too large to fit in between the QDs. The AFM tip recognizes the clusters as one big QD with height "off the chart", relative to the small QDs surrounding the cluster. One observation, that contradicts this explanation, is that the resolving abilities of the AFM in that case has to be strongly dependent on tip condition. No such dependence was seen in any sample. For instance, over hundred AFM images were captured of sample *544-1* alone - using both the *SINTEF* and *Biophysics* AFM with several different AFM tips. The large QDs was present in all AFM images of sample *544-1*, and the density of large QDs is nearly unchanged.

There seems to be a relationship between large QDs and *square defects*, but what are the *square defects*? Could the observed *square defects* simply be a scanning artefact? Firstly, if they were scanning artefacts one should expect that they were identical. This is not the case. The number of large QDs inside each square and the size of the squares are varying. Secondly, if the *square defect* were a scanning artefact they should all be parallel and perfectly aligned. Surely, some of the squares are parallel - but not all. From these two arguments, it could be concluded that the *square defect* is not a typical scanning artefact. The phenomena could still be a type of artefact not mentioned in the troubleshooting chapter of the *Veeco* AFM manual. The same *square defect* appeared on two different AFMs, not using the same tip, before and after calibration. The shape or size of the *square defect* seemed to be virtually the same. Based on these observations and arguments, it seems unlikely that the *square defect* is a scanning artefact of any sort.

Could *square defects* be a product of image processing? Well, it can not be excluded. It was hard to see the *square defects* properly without increased contrast (Sec. 4.1). The AFM images were exposed to a series of very sophisticated and advanced filters. Hopefully, most of them improved the image quality and made the raw data more reliable. Still, most of the filters were used as a *black box*. The exact low-level interpretation was unknown. The author did not have time or experience to read the source code of every filters applied in this work. This stands as a general uncertainty in the entire experiment.

One indication is the visible size and shape of *square defects* in Sec. 5.1, compared to 5.7. It is obvious that the *square defects* generally are much more well-defined in $10\ \mu\text{m} \times 10\ \mu\text{m}$ AFM images than in images with smaller scan sizes. The *square defects* are barely visible in $1\ \mu\text{m} \times 1\ \mu\text{m}$ AFM images. In addition, some AFM images in Sec. 5.1 seem to suggest that the side lengths are varying between the different scan sizes. This was investigated briefly for sample *544-1*, but no

significant difference were found. Mostly because the variance in side lengths was large for all samples, as seen in Table 5.7. A more thorough investigation, including all samples and scan sizes, has to be conducted. However, it has not been prioritized due to the limited time.

Is there reason to believe that the QD density inside the square defects is higher or lower than the surrounding areas, as clustering of QD is more likely in region with high QD density? From observations, the height of the QDs inside the square defect is effectively lower than the surrounding regions. It is possible that the large QDs drains Indium from the nearby square region. This leaves the small QDs in the square defect lower fraction of Indium - affecting the size, height and volume of the small QDs surrounding the large QD.

Another, more hypothetical question is whether or not there exist *square defects* with more than one large QD in the centre? Many *square defects* have been observed with several large QDs inside, near the centre. But could *square defects* containing N large QDs inside its boundaries simply be an overlap of N *square defects*, each with a single large QD at its centre? Overlap between several *square defects* has been observed in several AFM images (Fig. 5.32 and 5.37). Combined with the fact that *square defects* with more than a single cluster at its centre often deviate in the direction of a more rectangular or irregular shape, it seems plausible.

The last question, relevant for work further, is how *square defect* can be avoided, and how it is related to growth parameters? Only one sample had very few or none observed square defects: sample 514-4. Sample 514-4 was one of the samples with lowest QD density, and had the lowest deposited InAs thickness of all samples (see Table 3.1). In contrast, sample 544-1 had the highest QD density, lowest growth temperature, a relatively high InAs thickness and highest density of *square defect*. Previous studies [44] imply that large QDs nucleate after the formation of smaller QDs, and only when the ML is beyond a certain thickness. This might explain why 514-2 (2.1 ML) and 514-4 (1.9 ML) had fewer large QDs per 1000 small QDs than the rest of the samples (2.3 ML). Still, all MBE growth parameters influence each other and the variation in large QD density can not be explained by different InAs thickness alone. Growth temperature is clearly a factor determining the number of square defects. Sample 503-1, 503-2, 504-1 and 544-1 all have the same nominal InAs thickness. There is an increasing growth temperature from 544-1 (455°C), 503-1 (475°C), 503-2 (480°C) to 504-1 (490°C), but the number of square defects per area is correspondingly decreasing in each step (Fig. 5.38). The samples investigated in this study seem to suggest that large QDs and defects can be avoided by a optimal growth conditions, for example by not depositing too much InAs during growth.

5.8 Discussion: errors and uncertainties

There are three types of error:

- ◇ *human error*: under- or overestimation in the manual masking of QDs, incorrect masking of boundary grains, subconscious cognitive biases.
- ◇ *random error*: sample contamination, tip missed surface features, piezoelectric oscillation, noise, drifting (thermal or mechanical), different scanning parameters,
- ◇ *systematic error*: biases in the equipment (deformed AFM tip), calibration, working condition (temperature) or software (loss of information in procedures/algorithms).

A fine image quality was required to extract accurate estimates of QD volume. Thus, lack of image quality increases uncertainties and errors in the estimation methods. Fig. 5.40 illustrates that QDs could *grow* into each other in very high-density images. Merging of QDs makes it hard to separate all QDs properly by manual or computational methods. There is always a possibility that some vital surface features are missed out, not captured in the AFM imaging. It is always hard to know whether all features were captured or not. The QD density depends on tip condition [36], as discussed above in Sec. 4.1.2. Studies suggest that there is a distortion in the AFM images when the distance between two QDs are less than the tip width. [36] A comparison of SEM and AFM images with QD density in the range $(2 - 20) \cdot 10^{10} \text{ cm}^{-2}$ at NTNU [45], suggested that the estimated QD density in the SEM images on average were 6% higher than in the AFM images. It is likely that the loss due to distortion in AFM is even higher in this samples, because the QD density is relatively higher in this study $((0.5 - 1.8) \cdot 10^{11} \text{ cm}^{-2})$.

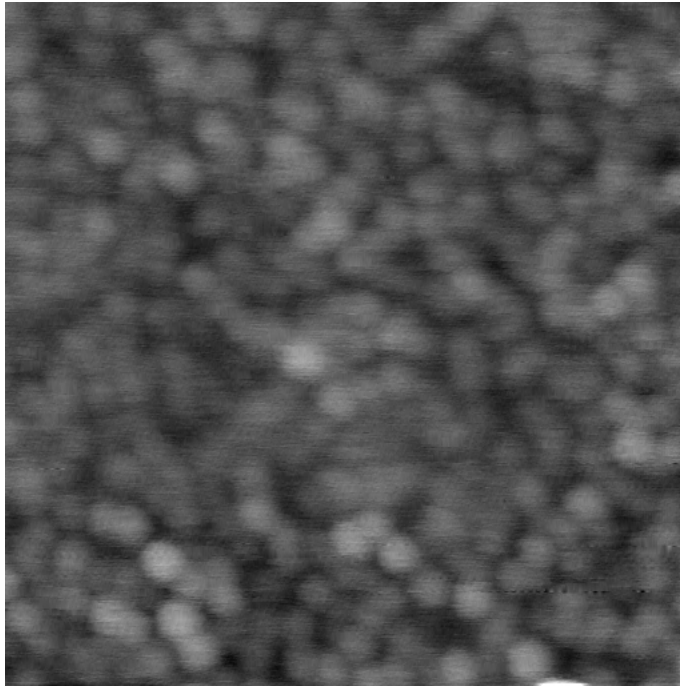


Fig. 5.40: A $500\text{ nm} \times 500\text{ nm}$ AFM image of sample *544-1*. Human error in the masking process could be a cause to uncertainty. The surface features had merged in some images and required extra attention, usually involving manual separation.

Suppose the AFM imaging reaches a *saturation* point and have problems catching up with QD densities higher than a definite level. That is, generally, the equipment is limiting the accuracy above a stipulated QD density. This was why it was so hard to extract reliable data from sample *544-1*, like illustrated by Fig. 5.40. It is quite possible that features are missed out” due to the height QD density.

Drifting was briefly discussed previously in Sec. 5.1, and was a prominent problem in images from sample *503-1* and *503-2*. Fig. 5.41 shows how drifting could be corrected in *Gwyddion*. Drifting could cause trouble, even though it was easy to detect and correct. It can be caused by rapid changes in temperature or mechanical stress. In the case of Fig. 5.41, the expansion is most likely thermally, caused by a change in temperature of $\Delta T = 3.6 \cdot 10^{-7} K$ during the sweep (assuming linear expansion). The AFM apparatus was placed upon a table. The table in the *SINTEF* lab. was shock-resistant, but there was always a risk by accident to touch the table and cause it to vibrate. In the *Biophysics* lab., the table was damped by pressurised air. The temperature in the *Biophysics* lab. was set to be lower and fluctuated less than in the *SINTEF* lab. Many parameters were altered during the scan to enhance the quality of the image. This could in turn change the outcome of the result. For example, varying the scan angle occasionally altered the number

of *visible* grain - simply because more grain features were captured under more optimal tip conditions. Still, it is a purely random error because the parameters had to be fine-tuning to different tips or parts of the samples. The parameters were changed each and every scan to find new optimal settings.

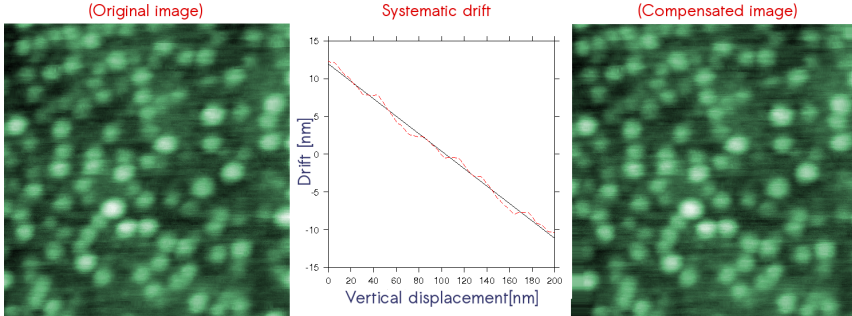


Fig. 5.41: Phenomenon such as *drifting* could cause projected grain area to stretch in one or several directions, as slightly seen by comparing the original image(left) and the drift compensated image(right). The black curve is a linear fit, and the red curve is the estimated slow-axis drift.

Some of the images were taken during a few days, using the same tip and working conditions. These AFM images are particularly prone to systematic error, like biases in the equipment such as deformed tips. The working temperature was not the same all the time. Working temperature could have a notable impact on the results, when imaging samples in the mesoscopic scale. Each image was processed following the procedure found in Sec. 4.1. The aim was to improve the image quality and increase data reliability. One cannot exclude the possibility that some information got lost during image processing. The author neither had time nor experience to point out every potential source of error in the algorithm procedures. Image processing errors remain unknown.

5.8.1 Error in *surface area method* (V_h)

The *surface area method* (V_h) was in Sec. 5.5.4 found to be the most reliable volume estimation method based on AFM data only. There are two major sources of error in the *surface area method* (V_h), namely, grain size (base area) and height. The volume of a QD is a function of grain size, shape and height. The error in QD shape can be eliminated, since the *surface area method* (V_h) integrates the height in all points over the entire surface. It is known that the condition of the AFM tip can affect the measured size and shape of QDs. The unreliability of AFM area estimates can clearly be seen in Fig. 5.9. SEM does not have the same problem, and give more accurate estimates of the QD size. The exact error estimate is unknown and probably large. Oxidation layers could result in an underestimation in QD height, and thus also affect the QD volume. This was discussed in section 5.4.

Oxidation layers could result in an underestimation in QD height, and therefore an underestimation QD volume. There is no guarantee that the oxidation layer has the same thickness in the valleys between the QDs, as on the top of the QDs. Another major problem with oxidation is that the oxidation rate, i.e. how rapidly the oxidation process goes, is likely to be biased by factors such as growth temperature and deposited In ML thickness. None of the samples was fabricated at the same time. The oxidation layer thickness strongly depends on how long time the sample has been exposed to air. Most oxidation processes are non-linear in time. It is probable that a saturation oxidation level is reached at some point, and that the oxidation rate declines after the sample has been exposed to air for a while. Still, various degrees of oxidation are expected.

In the *surface area method* (V_h), the 2D mask size of the QD is not determined by projected area or QD diameter. It is defined by the mask surrounding the boundary of the QD, including valleys and in some cases boundaries other QDs or step edges. The volume is estimated relative to the lowest z value within the mask. If the mask includes a step edge and the terrace below, the QD volume would be estimated relative to the lower terrace - consequently an overestimate. Likewise, if the QD is completely merged with surrounding QDs - the volume would become an overestimate. In a typical AFM image, these effects contribute to a random error. The error can be reduced by taking the mean values of several images.

5.8.2 Uncertainties

There are, as in most experiments, many sources of uncertainty.

In the QD density

The uncertainty was estimated by repeating the entire counting process (see Sec. 4.1) several times (> 5) in a high-density AFM image. This means that the uncertainty found is not only related to human error, but also a result of different blind tip estimations and the *thresholding/watershed*-algorithm. The counting uncertainty is generally larger in high QD density images than the lower-density images, and assumed to depend on the quality of the AFM image. The uncertainty in the counting process was approximately to be less than $0.07 \cdot 10^{11} \text{ cm}^{-2}$ error for *544-1*, the sample with highest QD density and poorest image quality. This corresponds to a relative error of less than 4%.

The uncertainty will show a discrepancy from image to image, depending on image quality, topology and QD density. The observed differences in QD density between AFM images at the same locations are often explained by other factors, such as tip conditions (see Sec. 4.1.2). A conservative estimation for all images in general, including the low-quality images, is to hypothesise that the relative counting uncertainty is less than 5% in general. For sample *503-1*, it corresponds to an over- or under-counting of 13 grains for $500 \text{ nm} \times 500 \text{ nm}$ AFM image, or ± 52 grains for $1 \mu\text{m} \times 1 \mu\text{m}$ AFM images. If there had been a greater counting uncertainty, an evidential larger sample variance would have been observed.

In the QD volume

The uncertainty in the QD volume depends on the uncertainty in grain height and projected area. The error in the estimation method is expected to be much larger than the uncertainty. This is thought to be a minor uncertainty, and less important than other uncertainties.

In the AFM

The two AFMs used in this study were calibrated once a year. The *SINTEF* AFM was calibrated with a 10 μm pitch reference in October 2010. The AFM images were taken both before and after the calibration. The uncertainty in X/Y scanning before calibration is unfortunately unknown. The calibration corrected for non-linearities in X/Y scanning directions. The relative uncertainty for X/Y scanning was after calibration approximately $\pm 2\%$. The deviation from linearity is probably smallest around zero offset for X/Y and Z scanning directions.

The *biophysics* AFM was calibrated at October 15th, 2011. Orthogonality, dimensions, linearity and sensitivity were checked using a calibration grid in all three scanning directions. The calibration was done using a 1 $\mu\text{m} \times 1 \mu\text{m}$ grid for X/Y calibration, and the 3 $\mu\text{m} \times 3 \mu\text{m}$ grid for Z calibration (180 nm deep wells). After calibration, Z sensitivity was measured to be 75.5 nm / V. The *biophysics* AFM was at the same time checked for errors, and the AFM head was sent to *Veeco* in Germany for inspection. No corrections were made.

Chapter 6

Conclusion

This master thesis was a study of self-organized InAs *quantum dots* (QDs) grown on GaAs substrates, for possible applications in *intermediate band solar cells* (IBSC). Six samples deposited by *molecular beam epitaxy* (MBE) were studied using *atomic force microscopy* (AFM). At least three locations per sample, each separated by several millimetres were examined. Density, height, projected area, homogeneity and total volume of the QDs were extracted from the AFM image data. Seven volume estimation methods were implemented and assessed for both $500\text{ nm} \times 500\text{ nm}$ and $1\text{ }\mu\text{m} \times 1\text{ }\mu\text{m}$ AFM images, and one method based upon both SEM and AFM data. Terraces, large QDs and defects were explored from contour maps and $10\text{ }\mu\text{m} \times 10\text{ }\mu\text{m}$ AFM images.

The most important findings are summarized as follows :

- ◇ The best, most trustworthy volume estimation methods were the *surface area method* (V_h) and the hybrid AFM / SEM method (V_{fusion}), based on $500\text{ nm} \times 500\text{ nm}$ AFM images. These methods are described in Sec. 4.3.
- ◇ Larger total estimated QD volumes are observed for increasing sample growth temperature and/or deposited InAs thickness. The total QD volume was not observed to be larger than the amount of InAs deposited.
- ◇ AFM images of the wetting layers support the existence of 2D islands, or terraces under the QDs. Higher terraces seem to be related to a higher degree of 3D island nucleation.
- ◇ Evidence of defects were found in nearly all samples. The defects were identified as inverted plateaus with well-defined, square-like shape.
- ◇ The *defect density* was correlated to growth temperatures and deposited InAs thickness. The defect levels in the samples were closely related to the density of large QDs. Excess amounts of deposited volume were related to higher/multiple *defect density*.

More studies must be conducted to conclude the findings in this study. The concept of 2D islands, or terraces, forming before QD nucleation has been established in several studies. [44] Square-shaped defects have been found in other, similar AFM studies. [43]

Further work

This was a study to explore the possibilities in the AFM. Much time and effort were spent to get the best out of the AFM, and only a small amount of the AFM images were actually used the analysis. I hope that the work is without any major flaws, and that the extracted data is accurate within the predicted uncertainties.

More studies on the effect of growth temperature and deposited InAs amount on QD volume and *defect density* are needed to reinforce the conclusions made above. The erosion mechanism was studied briefly, but it was not conclusive. A thoroughly investigation of *wetting layer* could reveal more. Finally, a study to investigate how rapidly the measurable post-growth QD height changes with shelf time, is highly suggested. It is crucial to obtain accurate numerical values for height of the QDs in volume estimations. More studies are needed to find the impact that oxidization processes have on various types of samples.

Bibliography

- [1] A. E. Becquerel. Mémoire sur les effets électriques produits sous l'influence des rayons solaires. *Comptes Rendus*, 9:561–567, 1839.
- [2] A. Stoletow. Sur une sorte de courants électriques provoqués par les rayons ultraviolets. *Comptes Rendus*, CVI:1149, 1888.
- [3] J. Czochralski. Ein neues verfahren zur messung der kristallisationsgeschwindigkeit der metalle. *Zeitschrift für Physikalische Chemie*, 92:219, 1917.
- [4] G. K. Teal, M. Sparks, and E. Buehler. Growth of germanium single crystals containing p-n junctions. *Phys. Rev.*, 81(4):637, Feb 1951.
- [5] D. M. Chapin, C. S. Fuller, and G. L. Pearson. A new silicon p-n junction photocell for converting solar radiation into electrical power. *Journal of Applied Physics*, 25(5):676–677, 1954.
- [6] New York Times. Vast power of the sun is tapped by battery using sand ingredient. Apr. 26, 1954.
- [7] Sunshakti Energy Solution Pvt. Ltd. Solar power plant. <http://www.sunshakti.co.in/images/sunshakti-directors-profile.pdf>, 2010.
- [8] S.W. Glunz O. Schultz, R. Preu and A. Mette. Silicon solar cells with screen-printed front side metallization exceeding 19% efficiency, 2007.
- [9] U.S. Department of Energy. What is the energy payback for pv? Technical report, The National Renewable Energy Laboratory, 2004.
- [10] Next Insight. Anwell produces its first solar panel: <http://www.nextinsight.net/index.php/story-archive-mainmenu-60/36-2009/1480-anwell-produces-its-first-solar-panel>, 2009.
- [11] William Shockley and Hans J. Queisser. Detailed balance limit of efficiency of p-n junction solar cells. *Journal of Applied Physics*, 32(3):510–519, 1961.
- [12] Brad Siskavich. Solar junction. <http://optics.org/news/2/4/22>, 2009.

- [13] Antonio Luque and Antonio Martí. The intermediate band solar cell: Progress toward the realization of an attractive concept. *Advanced Materials*, 22(2):160–174, 2010.
- [14] Steven Jenks and Robert Gilmore. Quantum dot solar cell: Materials that produce two intermediate bands. *Journal of Renewable and Sustainable Energy*, 2(1):013111, 2010.
- [15] A. I. Ekimov and Onushchenko. Quantum size effect in three-dimensional microscopic semiconductor crystals. *JETP Lett.*, pages 345–349, 1981.
- [16] Kamada H. Quantum computing with qd excitons. *NTT Tech Rev*, 1:31–40, 2003.
- [17] X. Michalet, F. F. Pinaud, L. A. Bentolila, J. M. Tsay, S. Doose, J. J. Li, G. Sundaresan, A. M. Wu, S. S. Gambhir, and S. Weiss. Quantum dots for live cells, in vivo imaging, and diagnostics. *Science*, 307(5709):538–544, 2005.
- [18] Antonio Luque and Antonio Martí. Increasing the efficiency of ideal solar cells by photon induced transitions at intermediate levels. *Phys. Rev. Lett.*, 78(26):5014–5017, Jun 1997.
- [19] Jenny Nelson. *The Physics of Solar Cells*. Imperial College Press, 1st edition edition, 2003.
- [20] Andrew S. Brown and Martin A. Green. Impurity photovoltaic effect: Fundamental energy conversion efficiency limits. *Journal of Applied Physics*, 92(3):1329–1336, 2002.
- [21] Gerardo L. Araújo and Antonio Martí. Absolute limiting efficiencies for photovoltaic energy conversion. *Solar Energy Materials and Solar Cells*, 33(2):213 – 240, 1994.
- [22] A. Luque, Martí, A. , C. Stanley, N. Lopez, L. Cuadra, D. Zhou, J. L. Pearson, and A. McKee. General equivalent circuit for intermediate band devices: Potentials, currents and electroluminescence. *Journal of Applied Physics*, 96(1):903 –909, jul 2004.
- [23] David J. Griffiths. *Introduction to Quantum Mechanics*. Benjamin Cummings, 2st edition edition, 2004.
- [24] Pawel Hawrylak and Marek Korkusiński. Electronic properties of self-assembled quantum dots. In *Single Quantum Dots*, volume 90 of *Topics in Applied Physics*, pages 25–92. Springer Berlin / Heidelberg, 2003.
- [25] Tetsuo Soga. *Nanostructured Materials for Solar Energy Conversion, chapter 17*. Elsevier Science, 1st edition edition, 2007.

- [26] A. Martí, N. López, E. Antolín, E. Cánovas, C. Stanley, C. Farmer, L. Cuadra, and A. Luque. Novel semiconductor solar cell structures: The quantum dot intermediate band solar cell. *Thin Solid Films*, 511-512:638 – 644, 2006. EMRS 2005 - Proceedings of Symposium F on Thin Film and Nanostructured Materials for Photovoltaics - EMRS 2005- Symposium F.
- [27] Ben Streetman and Sanjay Banerjee. *Solid State Electronic Devices*. Prentice Hall, 6th edition edition, 2005.
- [28] Andrew S. Brown and Martin A. Green. Detailed balance limit for the series constrained two terminal tandem solar cell. *Physica E: Low-dimensional Systems and Nanostructures*, 14(1-2):96 – 100, 2002.
- [29] D. Leonard, K. Pond, and P. M. Petroff. Critical layer thickness for self-assembled InAs islands on GaAs. *Phys. Rev. B*, 50(16):11687–11692, Oct 1994.
- [30] M. Grundmann, J. Christen, N. N. Ledentsov, J. Böhrer, D. Bimberg, S. S. Ruvimov, †, P. Werner, U. Richter, U. Gösele, J. Heydenreich, V. M. Ustinov, A. Yu. Egorov, A. E. Zhukov, P. S. Kop'ev, and Zh. I. Alferov. Ultranarrow luminescence lines from single quantum dots. *Phys. Rev. Lett.*, 74(20):4043–4046, May 1995.
- [31] E Placidi, F Arciprete, M Fanfoni, F Patella, E Orsini, and A Balzarotti. InAs/GaAs(001) epitaxy: kinetic effects in the two-dimensional to three-dimensional transition. *Journal of Physics: Condensed Matter*, 19(22):225006, 2007.
- [32] E. Placidi, F. Arciprete, V. Sessi, M. Fanfoni, F. Patella, and A. Balzarotti. Step erosion during nucleation of InAs/GaAs(001) quantum dots. *Applied Physics Letters*, 86(24):241913, 2005.
- [33] A.G. Cullis, D.J. Norris, T. Walther, M.A. Migliorato, and M. Hopkinson. Stranski-krastanow transition and epitaxial island growth. *Phys. Rev. B*, 66:081305, Aug 2002.
- [34] Espen Selvig. Molecular beam epitaxial growth and 2004. characterization of GaInAsSb/AlGaAsSb mid-infrared laser structures.
- [35] Bruker. *Contact Mode AFM probes, type OTR4-10 (data sheet)*.
- [36] Shen-de Chen, Chiou-yun Tsai, and Si-chen Lee. Growth of InGaAs-capped InAs quantum dots characterized by atomic force microscope and scanning electron microscope. *Journal of Nanoparticle Research*, 6:407–410, 2004. 10.1007/s11051-004-4704-6.
- [37] 2010. Simon Riis Iden. Distribution of InAs/Al_{0.35}Ga_{0.65}As quantum dots across 1/4-wafer.
- [38] Digital Instruments. *Scanning Probe Microscopy: Training Notebook*, 3.0 edition, 2000.

- [39] Sadao Adachi. *Physical Properties of III-V Semiconductor Compounds: InP, InAs, GaAs, GaP, InGaAs, and InGaAsP*. Wiley-Interscience, 1st edition edition, 1992.
- [40] Index. volume 89 of *Advances in Electronics and Electron Physics*, pages 481 – 491. Academic Press, 1994.
- [41] 2012. Sedsel Fretheim Thomassen. PhD Thesis (in preparation).
- [42] G. Hollinger, R. Skheyta-Kabbani, and M. Gendry. Oxides on gaas and inas surfaces: An x-ray-photoelectron-spectroscopy study of reference compounds and thin oxide layers. *Phys. Rev. B*, 49:11159–11167, Apr 1994.
- [43] K. Gradkowski, T. C. Sadler, L. O. Mereni, V. Dimastrodonato, P. J. Parbrook, G. Huyet, and E. Pelucchi. Crystal defect topography of stranski–krastanow quantum dots by atomic force microscopy. *Applied Physics Letters*, 97(19):191106, 2010.
- [44] O Bute, G H V Cimpoca, E Placidi, F Arciprete, F Patella, M Fanfoni, and A Balzarotti. The monitoring of 2d-3d transition for inas/gaas (001) self-assembled quantum dots by atomic force microscopy. *Journal of Optoelectronics and Advanced Materials*, 10(1):74 – 79, 2008.
- [45] S. Fretheim Thomassen, T. Worren Reenaas, and B.O. Fimland. InAs/GaAs quantum dot density variation across a quarter wafer when grown with substrate rotation. *Journal of Crystal Growth*, 201:-, 2011.